Formation process of Fe oxide bands and bleached spots by water–rock interaction

（水–岩石反応による酸化鉄バンド及び溶脱スポットの形成プロセス）

KAWAHARA, Hirokazu

（河原　弘和）

A dissertation for the degree of Doctor of Science

Department of Earth and Environmental Sciences,

Graduate School of Environmental Studies, Nagoya University

（名古屋大学大学院環境学研究科地球環境科学専攻学位論文　博士（理学））

2023

Abstract

Iron (Fe) is the fourth most-abundant element, accounting for ≈5 wt% of the elements found in the Earth's crust and is more ubiquitous compared to other metal elements. However, although various examples of Fe concentration phenomena are known, water-rock reactions in the shallower crust have rarely been treated as a major research topic. In addition, some recent studies focusing on the Fe-concentration mechanism have also been conducted to understand the water-rock reaction process on Mars. Although the pH of groundwater penetrated into rocks has been considered as an important factor controlling the element migration on Earth and Mars, the detailed reaction process has not yet been understood.

This study focuses on "Zebra Rock" in the eastern the Kimberley region of northern Australia. Zebra rock is Ediacaran siltstone with a unique texture with reddish-brown Fe-oxide bands ranging from a few millimeters to 2 cm in width. There are not many numbers of previous studies of zebra rock, especially based on the latest geochemical analyses and petrological descriptions. The detailed studies of Fe oxide bands in zebra rock are expected to provide us information about the element migration associated with water-rock reactions in the sedimentary rock, and better understanding of the mechanism of Fe precipitation over a wide area in the shallow crust.

As a result of this doctoral study, it was revealed that zebra rock can be divided into two types based on the clay mineral assemblages: kaolinite-rich type and alunite-rich type. These clay minerals indicate that zebra rock has undergone an acidic alteration, and the differences in mineral assemblages may reflect differences in the acidity of the fluid that infiltrated into the original rock. Elemental mapping of the Fe oxide bands in zebra rock also shows the asymmetric Fe concentration distribution in the bands, indicating the direction of migration of the reaction front of Fe precipitation. In addition, as the mechanism of Fe-precipitation in zebra rock, it can be

shown that the reaction was occurred by pH buffering of the Fe-bearing acidic fluid induced by the neutralization reaction between the fluid and the clastic minerals of the original rock.

For the first time, bleached spots in zebra rock have been discovered, which is about 100 μm in diameter and is accompanied with polygonal dickite pseudomorph in the center of the spot. The results of microscopic observation and mineral composition analysis indicate that the original mineral of the central pseudomorph is pyrite, and that the spots represent the extent of localized pH change in the pore water caused by the dissolution of original pyrite on a microscale.

These results in this study can be applied as the followings about the element migration and concentration mechanisms in water-rock reactions on both Earth and Mars:

- It should be possible to reveal the infiltration direction of the fluid by analyzing the Fe concentration distribution in the bands, and to infer the spatiotemporal extent of diffusion path of the fluid in the area by mapping this information. The source of the Fe-bearing acidic fluid could also be investigated as well.
- The time scale of Fe-oxide band formation in zebra rock can be estimated from the relationship between the spacing of bands and the diffusion coefficient of the rock.
- pH reactions may be the one of the major mechanisms that create large-scale and high-grade element concentrations in the shallow crust, and the proper geological and geochemical settings for pH changes can be targets for mineral resource exploration.
- Bleached spots may indicate the presence of sulfides, implying the amounts of spots show the potential of mineralization of the hinterland and the sedimentary rock itself.

Contents

1. Introduction

1.1. Importance of iron's behavior in water–rock interaction system

Iron (Fe) is the fourth most-abundant element, accounting for ≈5 wt% of the elements found in the Earth's crust (Rudnick and Gao, 2005) and is used in manufacturing ironware and is more ubiquitous compared to other metal elements. Thus, Fe is the most familiar metal to mankind historically and has been used for the longest time after bronze. Fe is used in many industries today, including automobiles, railroads, ships, buildings, and machinery and is referred to as the "backbone of modern industry."

Fe is extracted as a mineral resource from anomalously concentrated deposits with average grades ranging from ≈20% to 50% Fe in the deposits. Following are examples of large-scale Fe deposits based on various geological and geochemical settings: banded iron formation (BIF), which is chemically precipitated by Fe and silica in seawater (e.g., Mesabi iron range in Minnesota, USA; Mt. Whaleback iron mine, Western Australia); hydrothermal and skarn deposits caused by volcanic intrusion and associated hydrothermal activity (e.g., Kiruna iron mine, Sweden; Chichibu mine and Kamaishi mine, Japan); orthomagmatic deposit where heavy minerals with high melting points are cumulated during crystallization differentiation (e.g., Bushveld igneous complex, South Africa); and hydrogenetic ferromanganese crusts on seafloors (Fig. 1).

In addition to Fe ore deposits, porphyry copper deposits, the most common type of Cu deposit, often accompany pyrite shells around intrusive rocks related to Cu mineralization, which is easily extracted as a high chargeability area by geophysical surveys and is a major target for mineral resource exploration. IOCG (iron oxide–copper–gold)-type deposits, which are one of the major copper deposits and are distributed in craton margins, are associated with magnetite–hematite

alteration and are targeted by gravity, electromagnetic, and magnetic surveys. Thus, Fe-bearing minerals are important indicators for major base metal exploration because Fe is highly associated with mineralization, even if the metal is not a direct target.

Multiple conditions, including temperature, pressure, oxygen and sulfur fugacity of fluids containing metals, host rock types, specific gravity, redox state, and pH conditions, are involved in the formation of these metal mineral deposits. Among them, redox and pH conditions play an important role in the elemental migration, concentration, and dissolution in rocks at lower temperatures and shallower crusts. In particular, Fe is a redox-sensitive element, and its valences (soluble ferrous iron [Fe^{2+}] and insoluble ferric iron [Fe^{3+}]) are good indicators of redox conditions during diagenesis, weathering, and alteration. Furthermore, because ferric ion can be dissolved in acidic fluids with a pH < 3, the distribution of Fe minerals is influenced by pH changes in acidic fluids containing Fe.

To identify potential zones of concentration of Fe and Fe-related metal elements, it is necessary to understand the migration and precipitation mechanisms controlled by pH and Eh conditions during water–rock interaction. Although the redox reaction zone is generally determined by the distribution of Fe oxide minerals—the oxidized zone with reddish color where Fe oxide minerals are contained and the reduced zone with white color where Fe oxide minerals were removed—the pattern of Fe oxide minerals by the difference of pH conditions is possible. It is difficult to distinguish which reaction caused the element enrichment, redox or pH reactions by only observing the distribution of oxide minerals. Consequently, a thorough examination of reaction histories is necessary.

In terms of redox reactions, Hofmann (1999) examined the behavior of redox-sensitive elements in redox conditions and multiple geological and geochemical settings. When an element concentration occurs along a redox boundary, the enrichment zone possibly has a wide spatial

extent, good continuity, and elemental zonation based on the redox sensitivity of each element. Some metal deposits formed by element concentrations by redox reactions include sandstone-hosted roll-front uranium deposits, secondary enrichment in porphyry copper deposits, and sediment-hosted copper deposits (e.g., Kupferschiefer, Germany and Poland, and in the Copperbelt, the D.R. Congo).

However, there are few examples where pH change has been considered the primary mechanism for a deposit-scale metal element concentration. Fe mineral concretions in sedimentary rocks (e.g., Chan et al., 2004; Potter et al., 2011; Yoshida et al., 2018), *Takashi-kozo*, which is a cylindrical aggregate of Fe oxide minerals concentrated around plant roots (Yoshida and Matsuoka, 2004, Yoshida et al., 2008), and Fe oxide bands in sandstone known as Picture Stone in the Navajo Desert in the United States, Petra Stone in Jordan, and Zebra Rock (zebra stone) in Australia (e.g., Ortoleva, 1984, 1993; Fu et al., 1994; L'Heureux, 2013; Yoshida et al., 2020), which occur in nonvolcanic setting with a much smaller scale and lower economy are examples of Fe precipitation induced by pH change.

The majority of these small-scale Fe concentrations are considered to be the result of chemical reactions between Fe-containing groundwater and sedimentary rocks or precursor materials, and the reaction histories are important to assuming the paleo-geochemical conditions in a shallower crust. For example, Fe oxide concretion was formed when the pH of Fe-containing acidic groundwater was increased and neutralized by initial carbonate concretions (Yoshida et al., 2018; Sirono et al., 2021). Furthermore, Yoshida et al. (2020) reported that pH buffering was a primary mechanism for the formation of 1-mm wide Fe oxide bands in a dacite cobble, which was induced by a neutralization reaction related to plagioclase dissolution and that asymmetric Fe concentration within a band indicates the direction of fluid infiltration. It is possible that Fe precipitation phenomena in a shallower crust could record certain information about element

migration and precipitation, as well as the hydrological behavior of the fluid involved in the Fe precipitation.

Based on the preceding background, it is necessary to consider whether metals were precipitated on a regional scale by pH change. If this is the case, it is expected that target areas for metal mineral exploration will be expanded, and the examples of small-scale Fe concentrations mentioned previously can be considered as a miniature of metal mineral deposits and could be a good analog for considering the precipitation process. Because mining activities are quantitatively, technically, and economically finite, mineral resource exploration for future mines must be continued. Therefore, an improved understanding of the behavior of Fe in rocks and groundwater is expected to contribute to an efficient mineral resource exploration and a stable supply of metal resources.

Furthermore, the distribution of Fe is observed not only on the Earth but also on the surface of Mars. Because of the abundance of Fe oxide minerals such as hematite and goethite, the Martian surface appears reddish brown. Although no significant concentrations, such as Fe ore deposits, have been confirmed to date, a probe on Mars has discovered hematite spherules (expressed as blueberries; Glotch et al., 2004; Squyles et al. 2004). Fe oxide concretions on the Earth are analogs of the Martian hematite spherules and that the spherules could have been formed by a paleo-water–rock reaction and Fe oxide concretions on the Earth (Chan et al., 2004; Ormö et al., 2004). Other metal element concentrations, on a larger or smaller scale, may exist in Martian rocks because of paleo-water-rock reactions. The knowledge of Fe behavior on the Earth could be useful in tracing the paleo-aqueous environment on Mars.

Unlike the Fe concentrations described earlier, white reduction (bleached) zones formed by partial Fe oxide dissolution in Fe-rich sedimentary rocks such as red bed can be reported all over the world. In Utah, USA, reduction zones are distributed on a scale of several tens of kilometers,

and it is considered that fluids containing hydrocarbons and carbon dioxide migrated along fractures and bedding planes in the red sandstone, causing Fe oxide minerals to be dissolved (Beitler et al., 2003; Gilfillan et al., 2008; Wigley et al., 2012; Kampman et al., 2014). The reduction zone is an easy target for satellite image analysis because of the distinct color differences caused by the distribution of Fe oxide minerals, and the area of the zone is evaluated to estimate the range of water–rock reactions (Beitler et al., 2003). This type of research is expected to be implemented to the carbon dioxide capture and storage (CCS) technology because the breached zone represents a trace of carbon-containing fluid flow. A previous study suggested that the large amount of carbon dioxide produced by the reaction between Fe oxide minerals in red beds and carbon dioxide-containing reduced fluids may have affected the Earth's environment (Beitler et al., 2003). White reduction (bleached) spots on the scale of several millimeters to centimeters have been observed in Fe-rich sedimentary rocks on a considerably smaller scale than the bleached zones described earlier and have been reported worldwide (Table 1). The spots can be observed in red sandstone used in the walls of city buildings. The process of spot formation has been proposed as the reduction by reducing fluids (Curiale et al., 1983; Parnell and Eakin, 1987; Chan et al., 2000; Eichhubl et al., 2009; Wigley et al., 2012; Kampman et al., 2014), organic matter as a precursor (Van de Poll and Sutherland, 1976; Durrance et al., 1978; Mykura and Hampton, 1984), hydrogen sulfide by microbial activity, or Fe-reducing bacteria (Hofmann, 1990, 1991; Spinks et al., 2010; McMahon et al., 2018).

A white reduction spot has three dimensions and is spherical. Therefore, it has been used as a strain marker for the degree of strain and deformation direction, assuming that it was initially a perfect sphere (e.g., Kneen, 1976; Wood et al., 1976; Cogne and Gapais, 1986; Borradaile, 1988, 1991; Gray and Nickelsen, 1989; Kligfield et al., 1981, 1983).

Some of these white spots contain metals such as uranium, vanadium, and copper in the center

of the spot and are sometimes known as “fish-eye concretion” because of their appearance (Harrison, 1975; Parnell, 1988; Hofmann, 1990; Milodowski et al., 2000, 2002; Yoshida et al., 2014). They are distributed throughout the world (Table 2). Although the source of these elements is unknown, some research indicates that microbial reduction is the most likely mechanism of elemental concentrations (Spinks et al., 2010; McMahon et al., 2018). The spots can be considered as biomarkers, which will be used in the search for life on Mars where the surface is covered with Fe oxide (e.g., Parnell et al., 2016; McMahon et al., 2018). However, not all white spots are associated with heavy metal concentrations, and it is necessary to carefully examine whether all white spots are of biogenic origin.

Thus, these bleached textures where Fe oxide minerals disappeared are useful markers for kinetic and geochemical conditions, as well as for extraterrestrial life exploration. Previous research has mostly explained the formation of bleached textures by the reduction of Fe oxide. However, if other processes can be elucidated, it is expected that these textures could have the potential to provide a wider range of information and be used as another marker during element migration and concentration in the rocks.

As previously stated, there are numerous examples of Fe concentration and dissolution phenomena in the shallow crust. However, not all of their mechanisms have been explained. While Fe concentration has been extensively studied, primarily in Fe oxide concretions and Fe dissolution (bleaching) in red sandstones, other cases have received little attention.

This doctoral research focuses on “zebra rock,” which is also known as Fe oxide banding texture, to understand the factors that influence element migration and concentration. The rock is a very fine-grained sedimentary rock found in the eastern Kimberley region of northeastern Western Australia, with rhythmic Fe oxide bandings and elliptical spots ranging in width from several millimeters to centimeters (e.g., Loughnan and Roberts, 1990; Mattievich et al., 2002,

2003; Retallack, 2021; Kawahara et al. 2022a). Unlike Fe oxide concretions, which have Fe concentration at a single point, the Fe oxide bands show spatially wide distribution with high Fe concentration. There have only been a few previous studies of zebra rock based on modern petrological and geochemical observations, and the formation process has remained debatable for almost a century. Furthermore, several bleached textures were observed in zebra rock for the first time in this study. Zebra rock is an interesting example that allows us to simultaneously examine and observe the mechanisms of Fe concentration and dissolution.

1.2. Geological background of the zebra rock occurrence

Zebra rock can be reported in the eastern Kimberley region of northeastern Western Australia as discontinuous lenses or seams of ≈2 m in thickness within the Johnny Cake Shale Member, which is interbedded within the Ranford Formation of Ediacaran sedimentary rocks, and the occurrences are continuously distributed for several tens of kilometers around Lake Argyle across Western Australia–Northern Territory boundary (Fig. 2; Dow and Gemuts, 1969; Sweet, 1973; Tyler et al., 1998; Thorne et al., 1999; Dunster et al., 2000, 2013; Bevan, 2001). However, because the term “zebra rock” refers only to rocks with the characteristic banding pattern of Fe minerals, the actual distribution of rocks of the same composition as zebra rock without the pattern is currently unknown.

The Ranford Formation belongs to the Neoproterozoic Duerdin Group and is located on the eastern margin of the Halls Creek Orogen, extending over tens of square kilometers in northern Australia (Thorne et al., 1999). The Ranford Formation comprises two subcomponents: the Jarrad Sandstone Member and the Johnny Cake Shale Member. The lower Jarrad Sandstone Member is composed of fine-grained dolomitic sandstone, and the upper Johnny Cake Shale Member is composed of micaceous siltstone and shale (Dow and Gemuts, 1969; Sweet, 1973; Dunster et al.,

2000). Based on his paleopedological research, Retallack (2021) reported the depositional setting of the Johnny Cake Shale Member, including zebra rock as lacustrine basin similar to a playa or salt lake. Moreover, using a paleomagnetic study of hematite pigment in zebra rock, Abrajevitch et al. (2018) indicated that the Johnny Cake Shale Member has not been affected by metamorphism or diagenesis at temperatures >300 °C after the formation of Fe oxide bands.

In the Duerdin Group, the Ranford Formation conformably overlays the Moonlight Valley Formation (Tillite), which is composed of glacial deposits and uppermost dolomicrite (Dow and Gemuts, 1969; Sweet, 1973; Dunster et al., 2000). The Moonlight Valley Formation is a glacigenic succession in the late Cryogenian, which is correlated with the Elatina Formation in southern Australia, the representative cap carbonate sequence of the Marinoan glaciation (Corkeron, 2007, 2008). The Moonlight Valley Formation, which is composed of a fine dolomitic matrix, easily weathers and is mostly preserved as clastic materials (Corkeron, 2008).

The Duerdin Group is unconformably overlaid by the Kalkarindji flood basalt, which is thought to have been active during the early Cambrian period (Glass and Phillips, 2006; Jourdan et al., 2014) and to have covered an area of $>2.1 \times 10^6$ km^2 in northern Australia (Evins et al., 2009). The Kalkarindji flood basalt eruption is considered to have caused global environmental change and has been linked to the Early-Middle Cambrian boundary mass extinction event (Glass and Phillips, 2006; Jourdan et al., 2014).

1.3. Previous studies on zebra rock in the Kimberley region

Larcombe (1924) first described zebra rock in the Kimberley and proposed that the zebra pattern was formed by the introduction of hydrated Fe oxides at regular intervals during sedimentation in a marine environment. Then, the formation process of zebra rock has been discussed in terms of whether it was a syn- or post-depositional phenomenon: by the accumulation

of Fe minerals in ripple troughs (Geidans, 1981) or by the acidic alteration around primary pyrite particles (Hobson, 1930). However, these studies were based solely on the appearance of zebra pattern and not on modern petrological and geochemical analysis.

For the first time, Loughnan and Roberts (1990) used a detailed scientific approach to study zebra rock, demonstrating mineral assemblages, bulk compositions, and transmission and scanning electron microscopy observations. They described that zebra rock is composed of quartz, kaolinite, dickite, a polytype of the kaolin group, sericite, and alunite and that the abundances of kaolinite–dickite and sericite–alunite tend to be inversely related. In terms of the formation model of the zebra pattern, they suggest that pH fluctuations in pore fluid caused by pyrite oxidation in the original sediment formed colloidal hematite (Fe_2O_3) particles and that the banding pattern developed through periodic coagulation with the increase in the concentration of precipitated Fe oxide.

Retallack (2021) recently reported the outcrop occurrence and geochemical investigations of the Johnny Cake Shale Member, including zebra rock and neighboring sedimentary beddings. Based on his paleopedological perspectives, he illustrated the depositional setting of the Johnny Cake Shale Member as a surrounding of a lacustrine setting, such as a playa or salt lake, under an acidic condition, and concluded that the zebra rock formation was caused by the soil gleization of acid lacustrine sediments by acid sulfate weathering of primary pyrite, as proposed by Loughnan and Roberts (1990). He described the Fe oxide band as having homogeneous Fe-content distributions and considered that the zebra pattern was formed by a partial reduction of Fe oxide in reddish soils by Fe-reducing bacteria (Chen et al., 2019), rather than an addition of Fe oxide to reddish bands.

Kawahara et al. (2022a) and Katsuta et al. (2022) demonstrated in their thesis that the Fe oxide bands were formed by Fe precipitation caused by pH buffering of Fe-containing acidic fluid. The

distribution of zebra rock outcrops is discontinuous, but over a total length of ≈50 km, a zebra pattern can be traced for up to 90 m in a single quarry (Retallack, 2022), which suggests that the Fe precipitation reaction by pH buffering in zebra rock may be related to a regional geological event. Although zebra rock is not currently regarded as an Fe ore, extensive pH reactions metal concentrations on a deposit scale may be involved.

Furthermore, Kawahara et al. (2022b) discovered white bleached spots of up to 1 mm in diameter in zebra rock (Fig. 3). A pH change, rather than a reduction reaction, is possibly an important mechanism in the spot formation process, as is the formation of Fe oxide bands. Although certain previous studies proposed that bleached spots could be used as a biomarker for extraterrestrial life investigation, the results of this study provide important insight into determining whether the spot is biogenic.

A detailed description and comprehensive petrological and geochemical investigations of zebra rock were conducted in this study, and zebra rock is a fascinating object of study that demonstrates the importance of pH changes in both Fe precipitation and dissolution reactions and retains information in water–rock reactions on a regional scale. The formation processes of both Fe oxide bands and bleached spots in zebra rock will be clarified in this thesis, and the behavior of Fe in water–rock reactions in sedimentary rocks will be discussed. This thesis proposes the significance of pH reaction as a metal precipitation mechanism, the possibility of application to mineral resource exploration by observing Fe oxide bands and white bleached spots, and the insight on bleached spots as a biomarker for the extraterrestrial life investigation on Mars.

2. Materials and Methods

2.1. Descriptions of zebra rock samples

Profs. H. Yoshida, K. Yamamoto, and M. Adachi of Nagoya University Museum obtained several zebra rock samples for this study in 2008 at the Zebra Rock Gallery in Kununurra, Western Australia. The samples were directly taken from the zebra rock mine in Lake Argyle before the mine was abandoned, and they were not processed products for ornaments. The mine's precise location, including the coordination of sampling points, has not been disclosed.

This study used nine zebra rock samples in total, with section sizes ranging from ≈5 cm × 8 cm in minimum to ≈10 cm × 20 cm in maximum (Fig. 4). The Fe-concentrated part of the samples exhibit three patterns: banding, elliptical spot, and layered. The width of bands ranges from several millimeters to ≈1 cm, which is the almost same as the one in previous studies. The term "Fe oxide band" in this thesis represents the texture in a cross section, and the bands in a section are practically aligned plates perpendicular to the bedding plane in 3D. Similarly, the elliptical spots in a section are extended tubes parallel to the bedding plane. The cross sections of all the samples were cut perpendicular to the bedding plane in the z-axis and to the direction of the extension of Fe-concentrated plates and tubes in the x-y plane (Fig. 5).

2.2. Microscopic observations

A polarizing microscope and scanning electron microscope (SEM) were used to examine the texture of the zebra rock, and energy-dispersive X-ray spectrometry (EDX) was used for qualitative analysis. Five zebra rock samples were cut into several thin sections. Bleached spots and associated polygonal dickite pseudomorphs were studied using SEM.

2.3. Mineral identifications

The main mineral compositions of zebra rock were determined using an X-ray diffractometer

(XRD; Multiflex, Rigaku Co.) in Nagoya University Museum, and the mineral identification of the micro textures was performed using Raman spectroscopy by Thermo Fisher Scientific Nicolet Almega XR in Laboratory of petrology in Environmental Study of Nagoya University.

XRD analyses were performed using Cu–Kα radiation (the Cu was subjected to an electron beam of 40 kV/40 mA) at a scan rate of 4°/min. A microdrill was used to create powdered samples.

Prof. N. Katsuta at Gifu University analyzed oxidation state of Fe oxide in the band using Fe K-edge X-ray absorption near-edge structure (XANES) spectra in Tsukuba, Japan, to identify whether the Fe oxide contains only Fe^{2+} or both Fe^{2+} and Fe^{3+} (Murakami et al., 2012; Katsuta et al., 2019). The spectra of Fe K-edge XANES were obtained using a synchrotron radiation beam. The XANES measurement was performed at BL9A, Photon Factory, KEK. An incident X-ray beam was acquired using a Si 111 double-crystal monochromator, and intensity was monitored using an ion chamber. After being mixed with boron nitride (BN) powder, reference samples were prepared as powder-pressed pellets and measured in transmission mode. A second ion chamber was used to measure the intensity of the X-ray after it passed through the sample. The experimental samples of zebra rock were nondestructively measured in fluorescence mode. The sample was set on a stage that was orientated at 45° to the incident beam. A Lytle detector installed at 90° to the incident beam detected the sample's Fe-Ka intensity. The incident X-ray beam size was about ≈1 mm × 1 mm. The monochromator was scanned at 0.5 eV steps in the range of 7.080 to 7.150 keV to obtain Fe K-edge XANES spectra. Each energy step was counted for 2 s. Energy calibration was adjusted by assigning the pre-edge peak position of Fe foil as 7.112 keV.

Reference samples such as Fe_2O_3 (hematite), FeO, FeO(OH) (goethite), $FeCO_3$ (siderite), and montmorillonite were used as Fe standards and were prepared as a mixture of a powdered sample with BN powder to form a disk. Alumina suspensions were polished and used as an experimental sample. The Fe^{3+} mole fraction was calculated based on the Wilke et al. method using the Fe-K

pre-edge centroid positions. The spectra were analyzed using REX 2000 version 2.5 software (Rigaku, Japan).

2.4. Bulk compositions

X-ray fluorescence (XRF) and CHNS elemental analyses for major elemental compositions (SiO_2, TiO_2, Al_2O_3, Fe_2O_3, MnO, MgO, CaO, Na_2O, K_2O, P_2O_3, and S) of Fe oxide band and the white area (i.e., the extent between Fe oxide bands) were conducted by Rigaku ZSX Primus II equipped using an Rh X-ray tube (50 kV/60 mA) and Elementar Vario EL cube, both in Environmental Study of Nagoya University. To prepare glass beads, 0.5 g of the sample (crushed to 125 μm or less) was mixed with exactly ten times the amount of lithium tetraborate and heated to 1,050 °C with 1 drop of lithium iodide as a remover (1 g LiI/2 g ultrapure water). Using a microdrill for fossil cleaning, the powdered sample was prepared in three parts: Fe oxide band, white areas, and the area outside the banding pattern (Fig. 6). To obtain the loss on ignition (LOI), the powdered samples were heated at 1,000 °C for 2.5 hours and then at 150 °C for 2 days to remove volatile components such as H_2O and SO_2 in zebra rock.

Bulk rock analyses for Fe oxide concretions collected in Mongolia and Jordan, as well as dacite cobbles with Fe oxide bands studied by Yoshida et al. (2020) were conducted to compare with other Fe-precipitated rocks. Powdered samples of Fe oxide concretion were collected from the Fe-precipitated parts of the spherical shell, with the core being weathered carbonate concretion (Fig. 7a–c). The dacite cobble powder samples were drilled at the Fe oxide band (1~2 mm in width), white areas, and the core part (Fig. 7d).

Open system mass balance (τ) calculations were also performed by comparing the chemical compositions of Fe oxide bands and white areas. The following equation was used to calculate mass balance (Anderson et al., 2002):

$$\tau\ (j) = (C(j,\ w) \times C(i,\ p)) / (C(j,\ p) \times C(i,\ w)) \ -\ 1 \qquad (1)$$

where j is an arbitrary element and i is an immobile element, and C(j, w) and C(i, w) represent the mass concentrations (weight percent) of elements j and i in an Fe oxide band, and C(j, p) and C(i, p) are the mass concentrations (weight percent) of elements j and i in white areas. Titanium was regarded as an immobile element (i). The mass balance calculation results show the difference in elemental concentrations between the current white areas and Fe oxide band, not a degree of Fe addition during band formation.

2.5. Elemental mappings

The 2-D semiquantitative elemental mapping on the surface of zebra rock samples was obtained by using a scanning XRF analyzer (SXAM; XGT-5200S Horiba Japan) at Nagoya University Museum to determine the spatial variations of Fe and other chemical constituents of zebra rock. A 100-m-diameter high-intensity continuous X-ray beam (Rh anode 50 kV/1 mA) was focused with a guide tube and irradiated the sample's surface perpendicularly. The samples were placed on a PC-controllable X-Y stage. A total of eight elements were detected: Si, Ti, Al, Fe, K, S, Cr, and Sr.

2.6. Trace elemental analysis

A JEOL JXA8800 electron microprobe (EMP) was used to perform quantitative major element analysis of Fe^{3+} minerals and dickite. The analytical conditions were an accelerating voltage of 15 kV, a sample current of 12 nA, and a beam diameter of ≈2 μm. For Fe^{3+} minerals and dickite, the counting durations were 20 s on peak and 10 – 20 s on the white areas. The irradiation time

was shortened because these are hydrous minerals. Natural and synthetic silicates and oxides were used as standard materials. A total of seven compounds, such as SiO_2, Al_2O_3, TiO_2, FeO, MnO, K_2O, and SO_3, were measured.

3. Results

3.1. Geochemical and petrological characteristics of zebra rock

Comprehensive petrological and geochemical studies of zebra rock have been carried out to elucidate the zebra rock formation process by investigating the distributions of major elements, bulk compositions, mineral assemblages, and microscopic observations.

3.1.1. Asymmetric Fe concentration distribution in Fe oxide bands

Figure 8 depicts the results of 2-D SXAM mapping of cross-sections of representative zebra rock samples. Higher Fe concentration parts correspond to reddish-brown bands. The spectra of Fe K-edge XANES analysis were performed to confirm the valence of Fe in Fe oxide bands. The results indicate many similarities with hematite, and the Fe^{3+} mole fraction was greater than 99.5% (Fig. 9) (Wilke et al., 2001; Murakami et al., 2012; Katsuta et al., 2019).

No other major element is concentrated in the bands, which is common feature for elemental mappings to all of the zebra rock samples. The white zones between the bands do not show any specific element concentration.

Dr. Katsuta of Gifu University (Katsuta et al., 2003) analyzed 1-D SXAM profiles extracted along zebra patterns from 2-D SXAM mapping using a lamination trace technique and found that they can quantitatively demonstrate this characteristic (Fig. 10). Focusing on one band, there is a trend in which highest Fe concentration peaks are observed on one side of each band in zebra

rock, which follows in the same direction consistently within a sample. This study describes for the first time the asymmetric Fe concentration in the band and the unidirectional trends, which differs from Retallack's (2021) argument that denies these features.

3.1.2. Two types of zebra rock based on mineral assemblages

The mineral assemblage of zebra rock is quite simple, consisting mostly of quartz and various types of clay minerals (Fig. 11a), with minor titanium (Ti) minerals such as rutile (TiO_2) and ilmenite ($FeTiO_3$). In Fig. 11a, hematite peaks were detected only in Fe oxide bands, and there were no differences in other mineral assemblages between the Fe oxide band and white zones.

According to the clay mineral assemblages, zebra rock can be divided into two types: kaolinite (Kao) and alunite (Alu). The Kao-type zebra rock is dominant in kaolinite and contains minor contents of sericite and alunite. However, the clay mineral in the Alu-type zebra rock is only alunite. This study examined seven zebra rock samples, three of which were Kao type and four were Alu type (Fig. 11b). Each type of zebra rock has unique characteristics, which are described as follows:

Kaolinite-type zebra rock

The composition of the Kao-type zebra rock is quite homogeneous, and the lamination of the Kao-type zebra rock does not appear clearly. In the microscopic observation, most of the quartz grains are less than 20 μm in size, very well sorted, and subrounded to subangular in shape (Fig. 12a, b). No authigenic quartz crystal was observed in this type. Some clay minerals, such as kaolinite and sericite, have relatively coarse-grained axes that run parallel to the lamination. Minor rutile and ilmenite are also observed. Hematite fills the space around quartz and clay minerals in the Fe oxide band part. Within the bands, hematite is not uniformly distributed (Fig.

12c).

Alunite-type zebra rock

The Alu-type zebra rock has many characteristics different from the Kao-type zebra rock, and one of them that is readily recognizable is its hardness. The Alu-type zebra rock is considerably harder than the Kao-type zebra rock and cannot be easily cut using a rock cutter. The lamination is very clear, but this zebra rock never breaks easily along the lamination.

The sedimentary rock is described as very well sorted and uniform and is composed of very fine-grained quartz and alunite of about less than 10 μm in size, with minor rutile and ilmenite (Fig. 13a, b). Particles of both quartz and alunite are so fine-grained that it is difficult to discriminate each grain under the microscope, and relatively coarse-grained quartz-rich seams are interbedding (Fig. 13a, b). Because of the higher Fe concentration, the Alu-type zebra rock is darker in color. Hematite coats around quartz and alunite in the Alu-type zebra rock as well as in the Kao-type zebra rock.

In microscopic observations, micro-normal fault was found in the Alu-type zebra rock (Fig. 13c). The lack of offset in the band despite the microfault crossing the band indicates that Fe oxide bands were formed after the sediments had solidified.

The Alu-type zebra rock has several types of bleached textures: dickite vein, dumpling-like clump of sediments, dickite pseudomorph after gypsum, and polygonal dickite pseudomorph (Fig 14). A dickite vein occurs parallel to the sedimentary structure between two elliptical Fe concentration parts (Fig. 13d and 14b). The dickite vein has a bleached halo, indicating Fe oxide minerals were dissolved in a certain area (Fig. 13e). Dickite veins always have bleached texture.

Three types of dickite pseudomorphs were also recognized in this study, each with bleached textures. The first one is a dumpling-like clump of sediments of several hundred micrometers in

size (Fig. 14c), consisting of relatively courser quartz grains and minor rutile compared to the surrounding clastic materials, and the matrix is dickite (Fig. 13f, g). The flattened part of the clump of sediment represents the lower surface when the deposition. Lower seams are also deformed, indicating that the clump of sediment dropped when the sediment was unconsolidated.

Second, dickite pseudomorphs with a rectangular strip shape and a size of several hundred micrometers exhibit bleached texture (Fig. 14d, e). Kawahara et al. (2022a) described them as pseudomorphs after gypsum because of their shapes (Tucker, 1976; Lambert et al., 1978; White, 1981). There is a specific layer of dickite pseudomorphs in a mosaic that is several millimeters wide (Fig. 13h, i). In such layers and around a pseudomorph, the surrounding Fe oxide minerals are slightly dissolved, and the zone appears white.

The third pseudomorph is a polygonal dickite with bleached spots. They are widely distributed in the Alu-type zebra rock and come in a variety of shapes, such as hexagonal, pentagonal, and trapezoidal. This type of pseudomorph will be described in detail later.

Although some zebra rock samples that contains 10~20% of alunite (Sample No. ZR1w In Loughnan and Roberts, 1990) and those with >30% of Fe_2O_3 in bands (Sample No. R5670R in Retallack, 2021) have been reported in previous studies, the former coexists with aluminosilicate mineral, and the latter shows very low value of K_2O (0.33%) in the bulk composition, which do not correspond to the characteristics of the Alu-type zebra rock described in this study. Other characteristics of the Alu-type zebra rock, such as hardness, microtextures under microscopic observations and the presence of bleached spots, can be used as indicators when verifying whether it is the Alu-type zebra rock.

Our samples were classified into the Kao-type and the Alu-type zebra rock which have been reported by previous studies (Loughnan and Roberts, 1990; Mattievich, 2002, 2003; Retallack,

2021). However, our Alu-type sample does not show transitional mineral assemblages different from that of Loughnan and Roberts (1990). Furthermore, dickite, a polymorph of kaolinite was identified by previous studies as a major component mineral of zebra rock (Loughnan and Roberts, 1990; Mattievich et al., 2002, 2003). However, in our samples, no dickite was detected in the Kao-type zebra rock using both XRD analyses and Raman spectroscopy, and it was found in the Alu-type zebra rock as a vein mineral and pseudomorphs rather than as a major compositional mineral.

3.1.3. Bulk compositions of zebra rock

In the representative samples of each of the two types of zebra rock, the bulk rock compositions were determined in the following three parts: Fe oxide band, white zones, and the outer areas showing a light reddish-brown color in the white zones. The results are shown in Table 3. The values of Fe_2O_3, CaO and MgO, and S are so distinctive that their results are described in detail below.

First, the amounts of Fe_2O_3 in the bands differ significantly between the two types of zebra rock, with the Alu-type zebra rock having more than three times the Fe concentration of the Kao-type zebra rock (at 9.31% – 9.46% in the Kao-type zebra rock and 30.1% – 30.5% in the Alu-type zebra rock). The values of Fe_2O_3 of adjacent Fe oxide bands in one sample are almost the same. On the other hand, the concentration factor of Fe by comparing Fe oxide bands to the white zones is 25.6 – 25.9 for the Kao-type zebra rock and 101.7 – 120.4 for the Alu-type zebra rock (Table 4). Because previous research has shown that the amount of Fe_2O_3 in the bands is less than 10% (Loughnan and Roberts, 1990; Retallack, 2021), which corresponds to the value of the Kao-type zebra rock, significant Fe concentration is a distinguishing feature of the Alu-type zebra rock. On the other hand, the amounts of Fe_2O_3 in the white zones are nearly identical in the two types (at

around 0.3% of Fe_2O_3 in both types).

Second, the amounts of CaO and MgO in zebra rock are remarkably low, with ~0.05% – 0.06% of CaO in both types, 0.20% – 0.21% of MgO in the Kao-type zebra rock, and 0.01% – 0.02% of MgO in the Alu-type zebra rock. Sedimentary rocks usually contain carbonate minerals as a cement to fill the pores among the grains, but no carbonate mineral was found in zebra rock (Retallack, 2021). This corresponds to the XRD results without detecting any carbonate minerals.

Third, the amounts of S in the white zones, where the effect of Fe_2O_3 is minimal, differ significantly between both types. Compared to the values in the white zones in both types, the Alu-type zebra rock contains approximately 100 times more S than the Kao-type zebra rock, with 0.06% – 0.07% in the Kao-type zebra rock and 6.49% – 6.68% of S in the Alu-type zebra rock. Because no sulfide minerals were found in zebra rock, it is possible that this reflects the amount ratio of a sulfate mineral, alunite.

Table 5 displays the results of mass balance calculations performed by comparing the bulk compositions of adjacent white zones and Fe oxide bands. Both types show a high amount of Fe addition in the Fe oxide band compared with the white zones, whereas other elements indicate much less addition or depletion compared to the variation of Fe.

3.2. Mineralogical description of bleached spots and polygonal pseudomorphs

Bleached spots and polygonal pseudomorphs are observed only in the Alu-type zebra rock. Because no other past studies have reported similar texture, this study provides their comprehensive mineralogical descriptions as follows.

3.2.1. Micro textures of bleached spots and polygonal pseudomorphs

The bleached spots with the pseudomorph are always located at the margin of Fe oxide bands

with relatively lower Fe concentration (Fig. 15a–j). There is no Fe oxide mineral in a bleached spot of ≈100 μm in diameter around the polygonal pseudomorph. The bleached area is composed of quartz and alunite, which is the same mineral assemblage as in the surrounding Fe oxide band part except hematite. Bleached areas do not form around polygonal pseudomorphs that are located inside and outside the bands.

A single thin section could contain more than 10 polygonal pseudomorphs. Most of them are hexagonal in shape, with some pentagonal and minor trapezoidal shapes (Fig. 16). The pseudomorphs range in size from ≈50 μm in diameter inside Fe-bands to 20−30 μm in diameter outside Fe-bands.

Raman spectroscopy reveals that the polygonal pseudomorph is composed of dickite and Fe oxide minerals such as hematite (Fig. 17). Ilmenite, a minor titanium mineral, may also be present. In Fig. 18, the results of the elemental mapping by SEM-EDX are shown in four major elements: Fe, Si, Al, and S. The images of Fe, Si, Si-Al, and Al-S represent Fe^{3+}-minerals, quartz, dickite, and alunite, respectively. The elemental distribution within the pseudomorph differs greatly from that of the surroundings; sulfur, which represents alunite, is rarely found within the pseudomorph.

Polygonal pseudomorphs can be classified into three types based on microscopic observations, Raman spectroscopy, and elemental distributions (Table 6): (1) Fe^{3+} minerals (Fig. 16a–c and Fig. 18a), (2) dickite + Fe^{3+} minerals (Fig. 16d–h and Fig. 18b), and (3) dickite (Fig. 16i–l and Fig. 18c).

The type 1 pseudomorph is mostly composed of Fe^{3+} minerals, with minor dickite detected in the center (Fig. 18a). The pseudomorph has no compositional zonation. The type-1 pseudomorph is much more rare than the other types and is found only outside the band. They have no bleached spots.

The type 2 pseudomorph shows characteristic ring-shaped Fe^{3+} minerals in the mantle part,

and the other part comprises dickite. Type-2 pseudomorph exists both inside and outside the bands. This type accounts for the majority of pseudomorphs with bleached spots.

The type-3 pseudomorph is mostly composed of dickite, the most common of the three types. Type-3 pseudomorph can be found both inside and outside the bands.

3.2.2. Mineral compositions of polygonal pseudomorphs

Microprobe analysis was used to determine the mineral compositions of Fe^{3+} minerals of the type 1 pseudomorph and dickite of the type-3 pseudomorph (Table 7). The type 2 pseudomorph was not analyzed because separating Fe^{3+} minerals and dickite with a beam diameter of ≈2 μm is difficult.

The results of the analysis for mineral compositions correspond to the ones of Raman spectroscopy. Particularly, it was indicated that Fe^{3+} mineral in type 1 is an aggregation of hematite and Fe oxyhydroxides such as goethite because the composition is not 100% in total. Type 1 pseudomorph also contained very small amounts of SiO_2 and Al_2O_3 as impurities of clay minerals or quartz particles.

3.3. Bulk compositions of other rock samples with Fe concentration

This study analyzed the bulk compositions of a Fe oxide band in the dacite cobble in Yoshida et al. (2020) and the crusts of Fe oxide concretions in Mongolia and Jordan to compare zebra rock to other rocks with Fe concentration. The results are 3.65% of Fe_2O_3 for Fe oxide bands in the dacite cobble, and 28.3% – 31.9% and 7.03% of Fe_2O_3 for Fe oxide concretions in Mongolia and Jordan, respectively (Table 8). The concentration factor of Fe for Fe oxide bands in dacite cobbles is 3.38, while it is 35.8 – 50.6 and 28.1 for Fe oxide concretions from Mongolia and Jordan, respectively (Table 4).

4. Discussions

4.1. Zebra rock formation

Loughnan and Roberts (1990) proposed the oxidation of the original pyrite in the primary sediment and the periodic coagulation of colloidal hematite (Fe_2O_3) particles via pH fluctuations in pore fluid as the formation process of zebra rock. Recently, Retallack (2021) proposed another model of partial reduction of Fe oxide in homogeneously reddish gleyed soils by microbial activity.

However, previous studies cannot provide a comprehensive explanation for the following results demonstrated by this study: (1) the two types of zebra rock based on the difference of their clay mineral assemblages and Fe concentration in the bands and (2) the asymmetry of the Fe concentration distribution in the bands. Additionally, mass balance calculations indicate a significant Fe addition in zebra rock, which cannot be explained by the elemental migration in a closed system. Based on the findings of this study, a comprehensive formation model of zebra rock is provided here.

4.1.1. Acidic alteration of lacustrine sediments

Based on the results, Kawahara et al. (2022a) concluded that the clay mineral assemblages of the two types of zebra rock correspond well to the acidic hydrothermal alteration zonation and proposed a hydrothermal formation of zebra rock associated with undiscovered volcanic activity. Kawahara et al. (2022a) stated that the Alu-type zebra rock with higher Fe concentrations was formed near the center of the hydrothermal system, implying relatively higher temperature and lower pH of the fluid, whereas the Kao-type zebra rock was formed in the outer regions of the

system. However, Katsuta et al. (in preparation) performed sulfur isotope analysis of both types of zebra rock samples and obtained negative $\delta^{34}S$ values (<−20‰) from both types of zebra rock, indicating that sulfur in zebra rock is not the origin of volcanic activity (Rye, 2005), but rather the result of sulfide oxidation in lacustrine sedimentary rocks (Gorjan et al., 2000). Katsuta et al. (in preparation) proposed that the Fe-containing acidic fluid derived from the oxidation of the original pyrite was buffered by the lacustrine sediments, resulting in the formation of zebra rock formation. Later discussion in this thesis follows Katsuta et al.'s model that the external acidic fluid produced by oxidation of the original pyrite in the surrounding sedimentary rocks has diffusively infiltrated into the original rock of zebra rock.

The reactions between the sulfuric acidic fluid and primary potassium–aluminum silicate minerals, such as feldspars and mica minerals, in the original rock are shown in Eqs. (2) – (4):

$$3KAlSi_3O_8 + 18H_2O + 2SO_4^{2-} + 6H^+ \rightarrow KAl_3(SO_4)_2(OH)_6 + 9H_4SiO_4 + 2K^+ \quad (2)$$

Feldspar Acidic fluid Alunite

$$KAl_2(Si_3, Al)O_{10}(OH)_2 + 6H_2O + 2SO_4^{2-} + 4H^+ \rightarrow KAl_3(SO_4)_2(OH)_6 + 3H_4SiO_4 \quad (3)$$

Muscovite Acidic fluid Alunite

$$2KAlSi_3O_8 + 9H_2O + 2H^+ \rightarrow Al_2Si_2O_5(OH)_4 + 4H_4SiO_4 + 2K^+ \quad (4)$$

Feldspar Acidic fluid Kaolinite

It is assumed that the difference in the clay mineral assemblages was caused by the acidity of the fluid (i.e., possibly the distance from the source of the fluid). It is likely that the fluid near the source would have contained more sulfate and Fe ions and would have produced Alu-type zebra

rock, which is composed of alunite and has a higher Fe concentration. Far from the source, the acidic fluid contains less sulfate and Fe ions, resulting in the formation of Kao-type zebra rock with less sulfate.

On the other hand, the original sedimentary rock of the Kao-type zebra rock is considered to have been deposited closer to the sediment supply source because of its relatively coarse grains, while one of the Alu-type zebra rock should have been deposited farther from the source and at deeper areas because of its much finer grains and distinct laminae. Therefore, it is assumed that the supply direction of the sediments and the acidic fluid was different.

Alternatively, it is also possible that the two types of zebra rocks reflect different compositions of the original sedimentary rock prior to acidic alteration. The relationship between the mineral assemblages and the distinct differences in sedimentary textures and physical properties of these two types cannot be explained by infiltration of an acidic fluid, indicating that these were introduced by the two rock types originated owing to differences in alteration as well as types of original rocks. Furthermore, I consider that the Alu-type zebra rock is contained in a more different layer than the Kao-type zebra rock, possibly in a stratigraphically lower layer.

To verify these possibilities, a comprehensive field survey is required to confirm the distribution, provenance, and stratigraphic relationships of the two rock types. However, previous studies did not provide any additional field geological information regarding the two types of zebra rocks. Future field research is expected to identify the distribution of the two types of zebra rocks and the pyrite-containing layers, which may be the source of the sulfuric acid, and to provide more precise description of the zebra rock's alteration process.

Furthermore, this study considers the compositional minerals of the original rock before the alteration. In this study, carbonate minerals were not detected in both types of zebra rock. Microscopic examinations conducted by Retallack (2021) revealed that neither zebra rock nor the

adjacent layers contain carbonate minerals. However, as shown in Table 4, the concentration factor of Fe oxide bands in zebra rock is significantly greater than the one of Fe oxide bands in the dacite cobbles formed by the pH buffering by compositional silicate mineral of dacite and is closer to the concentration factor of Fe oxide concretions in Mongolia and Jordan formed around primary carbonate concretion.

Additionaly, because gypsum has a higher solubility than carbonate minerals, the carbonate minerals appear prior to crystallizing gypsum. Therefore, it is likely that at least the Alu type contained carbonate minerals.

Moreover, the deformational texture was observed in the Alu-type zebra rock, indicating that the laminae are deformed outside the band and that the spacing of laminae outside the band is smaller than that inside the band (Fig. 19). The ratio of spacing outside the band is ≈35% less than that inside the band. Because the sedimentary structure of the Alu-type zebra rock is undisturbed (Fig. 19) and micro-faults prior to the Fe oxide band formation have been identified (Fig. 13c), the primary sedimentary rock was consolidated before Fe oxide band formation. This indicates that the deformation described previously occurred after the sediments became unconsolidated. These observations suggest the former presence of carbonate minerals that buffered the pH sufficiently to precipitate Fe minerals. The carbonate minerals have a stronger pH buffering ability than siliciclastic materials and may precipitate more Fe than silicate minerals. Given the presence of carbonate minerals in the original rock, the following process could explain the deformation texture in Fig. 19:

(i) Acidic fluid diffused into the original lacustrine sediments, and the neutralization reaction has consumed the carbonate minerals in the rock.

(ii) Fe oxide minerals immediately filled with certain parts of pore created by the

disappearance of carbonate minerals (i.e., band formation), and the initial spaces of laminae remained.

(iii) The area outside the band retained high porosity due to the consumption of carbonate minerals. Because Fe minerals filled with pores, the laminae outside bands bent during compaction over time, whereas the ones inside bands were not easily deformed.

If the unaltered original rock of zebra rock can be found, the detailed compositions of the rock can be investigated, and quantitative element migration can be estimated by comparing the chemical compositions between the current zebra rock and the original rock.

4.1.2. Mechanism of rhythmic band formation by pH buffering

Two potential models for Fe precipitation mechanisms are as follows: (1) oxidation of soluble ferrous iron to insoluble ferric iron or (2) pH buffering that induced the precipitation of ferric iron in acidic fluid as Fe oxyhydroxide. In the oxidation model, an oxidation agent is required in the original rock. No such oxidizing agent or remnant of it has ever been found in zebra rock. Therefore, oxygenated pore water in the original rock is the most likely candidate for oxidizing agent. The Fe precipitation may have resulted from a reaction between an Fe-containing acidic fluid and oxygenated pore water in that case. However, because minor traces of pyrite are found in zebra rock (described in the later section), the pore water in the original rock could be in a reduced condition.

Fe oxide concretion is a representative example of Fe-precipitation by pH change in the pH buffering model. As the Fe oxide concretion formation, it is thought that the primary carbonate concretions have caused the pH buffering (Yoshida et al., 2018). However, in the zebra rock formation, Retallack (2021) described that no carbonate minerals are contained in both zebra rock

and the surrounding sedimentary layers. Therefore, the primary pH buffer materials are most likely siliciclastic sediments, such as primary feldspar and mica minerals, which comprised the original rock of zebra rock (Katsuta et al. in preparation). Also, as discussed previously, possible carbonate minerals may have contributed to the pH buffering.

The Fe-containing acidic fluid was produced by the oxidation of the original pyrite in a lacustrine sediment and infiltrated into the original rock of zebra rock. Through the transportation process, the Fe^{2+} in the acidic fluid was oxidized to Fe^{3+} at a pH ≈3 (Jurjovec et al., 2002; Lottermoser, 2007). The oxidation reaction of Fe^{2+} occurs as shown in Eq. (5):

$$4Fe^{2+} + O_2 + 4H^+ \rightarrow 4Fe^{3+} + 2H_2O \quad (5)$$

The acidic fluid reacted with the unaltered siliciclastic materials. The neutralization of the acidic fluid by the alteration of plagioclase and muscovite occurs as shown in Eqs. (2) – (4). During the neutralization reaction, precipitation of Fe oxyhydroxide (here represented for simplicity by ferric hydroxide) occurs as shown in Eq. (6)”

$$Fe^{3+} + 3H_2O \rightarrow Fe(OH)_3 + 3H^+ \quad (6)$$

Combining Eqs. (2) and (6), and (4) and (6), the Fe precipitation reaction by the neutralization can be described as Eqs. (7) and (8), respectively;

$$3KAlSi_3O_8 + Fe^{3+} + 18H_2O + 2SO_4^{2-} + 3H^+$$

Feldspar Acidic fluid

$$\rightarrow KAl_3(SO_4)_2(OH)_6 + Fe(OH)_3 + 9H_4SiO_4 + 2K^+ \quad (7)$$

Alunite Fe^{3+}-mineral

$$2KAlSi_3O_8 + Fe^{3+} + 12H_2O \rightarrow Al_2Si_2O_5(OH)_4 + Fe(OH)_3 + 4H_4SiO_4 + H^+ + 2K^+ \quad (8)$$

Feldspar Acidic fluid Kaolinite Fe^{3+} mineral

The zebra-like rhythmic banding pattern could be caused by the difference in the rates of fluid diffusion and reaction front (Yoshida et al., 2020; Kawahara et al., 2022a; Katsuta et al. 2022). While the Fe precipitation was taking place, the diffusion-dominated infiltrating fluid front where the neutralization reaction occurred preceded the Fe precipitation reaction front, lowering the pH around the reaction front, inhibiting the Fe precipitation reaction, and abruptly stopping the formation of the Fe oxide band. When the reaction front caught up with the fluid front, and the pH around the reaction front returned to near neutral, and the Fe precipitation reaction resumed to form the next Fe oxide band. The characteristic rhythmic bandings in zebra rock were formed by repeating this process, and the highest Fe concentration peak in each band indicates the infiltration direction (Yoshida et al., 2011, 2020).

4.1.3. History of the water–rock reaction to form zebra rock

Based on the previous discussion, the zebra rock formation process in the Kimberley region can be illustrated as follows (Fig. 20) (Kawahara et al., 2022a; Katsuta et al., 2022):

(i) The oxidation of original pyrite in a lacustrine sediment by oxidation produced Fe-bearing sulfuric acidic fluid. The acidic diffusive fluid infiltrated the early Ediacaran Johnny Cake Shale Member of the upper Ranford Formation.

(ii) As the acidic fluid diffused into the original rock, neutralization reactions with siliciclastic

sediments, such as feldspars and mica minerals (and possibly carbonate minerals), occurred, and the pH of the fluid immediately increased, causing Fe precipitation as Fe oxyhydroxide at the reaction front.

(iii) During the Fe precipitation reaction, the fluid front advanced ahead of the reaction front, lowering the pH of the Fe precipitation part and inhibiting the reaction (i.e., end of band 1). When the reaction front caught up to the fluid front, the Fe precipitation reaction resumed as the pH at the reaction front approached neutral (i.e., the band 2 formation). This stepwise progression of Fe precipitation formed the rhythmic banding pattern.

(iv) Due to the constant supply of acidic fluid, primary feldspar and mica minerals changed to acidic alteration minerals such as alunite, kaolinite, dickite, and sericite. The mineral assemblage of zebra rock varies with the pH of the fluid, reflecting the distance from the source of the fluid.

(v) As time passed and oxidation progressed, Fe oxyhydroxide ($Fe(OH)_3$) in bands changed to hematite (Fe_2O_3).

Wang et al. (2015) elucidated the Fe precipitation pattern transition in sandstone by Ostwald ripening mechanism induced by a change in flow velocity in advection and illustrated the distribution of Fe oxides in the form of nodules, bands, and relatively uniform spread in order of increasing flow velocity. Although zebra rock exhibits a similar pattern of transition, fluid migration is more likely to occur by diffusion because of its much lower permeability than sandstones. Because the patterns are bounded by sedimentary planes, it is inferred that differences in diffusion coefficients of each layer reflect on the patterns. However, because zebra rock underwent acidic alteration and the original texture is not preserved, it is difficult to infer the original properties.

Katsuta et al. (in preparation) determined the growth rate of Fe-precipitated band to estimate the timescale of Fe oxide band formation. The diffusion–formation rate relationship for Fe oxide bands was applied, as shown in Eq. (9):

$$D = V \times L \quad (9)$$

where D is the diffusion coefficient (cm^2/s), V is the formation rate of each band (cm/s), and L is the width of two peaks of Fe concentration in bands (cm). The estimated time scale of the formation of each band was 18.6 years (10^{-4} to 10^{-3} m/a) for the Kao-type zebra rock and 8.7 years (10^{-3} to 10^{-2} m/a) for the Alu-type zebra rock (Katsuta et al. in preparation). This estimation of formation time is interesting in terms of the spatiotemporal extent of paleo-water–rock reactions and it enable us to approximate the reaction rate of alteration zones, despite the fact that the diffusion–formation rate relationship is usually discussed only in terms of the duration of a band formation time (Yoshida et al., 2020).

4.2. Bleached spot formation in zebra rock

Some bleached textures in the Alu-type zebra rock range from tens of micrometers to millimeters. Zebra rock is characterized by unusual Fe concentrations, and it is interesting that the opposite reaction (i.e., partial Fe depletion) occurred in the same rock. However, because the Alu-type zebra rock was identified for the first time by Kawahara et al. (2022a), such bleached textures in zebra rock have never been described in any previous studies, and the formation mechanism is unknown.

Polygonal pseudomorphs are most likely directly responsible for the formation of bleached spots in bleached textures. This study focuses on the white bleached spots associated with the

polygonal dickite pseudomorph that provide a clue when investigating these bleaching phenomena. The following three points will be discussed to consider the formation process of the breached spots: What was the original mineral of the polygonal pseudomorph? When was the bleached spot formed? At last, how the bleached spot was formed?

4.2.1. Original mineral of the polygonal dickite pseudomorph

It is unlikely that the polygonal pseudomorphs, which comprise dickite and Fe^{3+} minerals, at the center of the spot were clastic materials in the sediments. Although both dickite and hematite have hexagonal platy crystal forms, one of the reasons is that the crystal plane is not parallel but perpendicular to the lamination (Fig. 16). If these minerals were deposited as clastic materials, they should be parallel to the sedimentary structure. Pseudomorphs are also much larger in size than the surrounding quartz and alunite, and their sides and vertices of pseudomorphs are extremely sharp and rarely broken (Fig. 16). These findings suggest that after deposition, the precursor minerals of the pseudomorphs had grown in the sediment.

Based on their mineral proportions, pseudomorphs can be divided into three types (Fig. 18). The transitional texture from the type 1 to the type 2, showing that Fe^{3+} minerals dissolved and the voids were filled with dickite, was observed (Fig. 16h), suggesting that the pseudomorphs changed from type 1 to type 3, and type 1 pseudomorph best preserves the characteristics of the precursor mineral. Therefore, it is likely that a single, homogeneous Fe mineral was used as the precursor mineral.

Furthermore, pseudomorphs are mostly hexagonal and pentagonal in thin sections, with a few quadrangles. The cross sections of the pseudomorphs in all of the zebra rock samples show the same pattern of shapes, indicating that the precursor mineral is in an isometric system. These pseudomorph cross sections provide information about the precursor mineral.

Given these morphological and geochemical characteristics, the most likely precursor of the pseudomorphs is euhedral pyrite. It generally has a cubic or octahedral shape, with cross sections corresponding to the shapes of the pseudomorphs when viewed under a microscope. Pyrite is commonly formed during diagenesis in sedimentary rocks and is easily dissolved under oxidation conditions. t is currently unknown why the original pyrite began to dissolve at the center and rim, as seen in the type 1 and type 2 pseudomorphs.

Given the origin of the original pyrite, it is expected that the sulfur isotope fractionation should be able to determine whether it is biogenic or abiogenic. However, no original pyrite remains in zebra rock. Because the Alu-type zebra rock containing the pseudomorphs has undergone the relatively stronger acidic alteration, it is considered that all of original pyrite had been completely oxidized. The relic of framboidal pyrite, which is characteristic of biogenic origin, has never been observed in zebra rock.

4.2.2. Timing of the bleached spot formation

The timing of the white bleached spot formation will be discussed in the perspective of pre-, syn-, or post-band formation by comparing the occurrence of pseudomorphs with and without bleached spots. As shown in Fig. 15k, the bleached spots were formed only at the margin of Fe oxide bands with relatively lower Fe concentration, and no spots were found inside the bands. This indicates that the position of the precursor mineral in the Fe oxide bands determines whether bleached spots could be formed and that there could be a relationship between the band formation and the spot formation.

All spots in the band should be overprinted by Fe precipitation if bleached spots developed prior to Fe oxide band formation. In contrast, if the bleached spots developed after the band formation, there should be bleached areas around a pseudomorph even inside the bands. However,

there are no pseudomorphs with such bleached regions inside the Fe band. It is possible that there was a substance (i.e., oxidant) to prevent the spot formation in the band, but no such substance has been observed.

Therefore, it is the most likely that the bands formed as a result of the bleached spots being produced during the Fe precipitation. When comparing the rates of band formation (i.e., Fe precipitation) reaction and spot formation (i.e., dissolution of Fe oxide mineral) reaction, it is assumed that the spots could not develop inside the bands due to relatively higher band formation reaction rate, whereas the spot formation reaction was more dominant at the margin of the bands due to relatively lower band formation reaction rate. As shown in Fig. 15j, the bleached area closer to the inner side of the band is smaller than the one closer to the outer side of the band at the bleached spot. This texture clearly shows that the sizes of bleached spots are decided by the difference in the reaction rates of Fe precipitation and dissolution.

4.2.3. Formation process of bleached spots by local pH decrease

According to earlier studies, the formation of white bleached spots has been explained by fluids containing hydrocarbons or carbon dioxide, organic materials as precursor, and microbial activities (e.g., Curiale et al., 1983; Mykura and Hampton, 1984; Hofmann 1990; Chan et al., 2000; Parnell et al., 2016). All of these are carbon-related chemical reactions. However, the original pyrite in the sediments is likely to be a trigger of the formation of bleached spots in zebra rock discovered in this study. This suggests that the bleached spot formed through an inorganic process as follows (Fig. 21):

(i) Euhedral pyrite (i.e., original pyrite) was formed in the lacustrine sediments, and acidic fluid infiltrated into the sediments (t1). The pore water became acidic overall.

(ii) A neutralization reaction occurred between the acidic fluid and siliciclastic materials in the sediments. Then, the pH of the pore water increased, and ferric iron in the fluid was precipitated as Fe oxyhydroxide (i.e., Fe oxide band formation) (t2–1) (Kawahara et al., 2022a).

(iii) Simultaneously, the original pyrite was oxidized and dissolved through fluid infiltration, as shown in Eq. (10):

$$2FeS_2 + 2H_2O + 7O_2 \rightarrow 2Fe^{2+} + 4SO_4^{2-} + 4H^+ \quad (10)$$

Pyrite

To the extent that hydrogen ions generated in Eq. (10) diffused, Fe oxyhydroxide was dissolved in the areas where the pH of the pore fluid decreased as shown in Eq. (11) (t2–2).

$$4Fe(OH)_3 + 8H^+ \rightarrow 4Fe^{2+} + 6H_2O + 3O_2 \quad (11)$$

The ferrous iron dissolved into the pore water was transferred by the fluid migration. These reactions could occur in a relatively short time when the pore water was being neutralized.

(iv) The pore water became acidic once more as the supply of the Fe-containing acidic fluid was maintained. No Fe oxyhydroxide could be precipitated again in the bleached area because of the exhaustion of siliciclastic materials (and possible carbonate minerals) in the original rock. Acidic alteration resulted in a complete transformation of the siliciclastic materials into alunite (t3).

(v) Over time, oxidation transformed the precipitated Fe oxyhydroxide into reddish-brown Fe

oxide bands. Alternatively, the areas where Fe oxyhydroxide was dissolved were preserved as white bleached spots (t4).

The voids due to the dissolution of pyrite were filled by dickite. Based on the ratio of the original pyrite oxidation level, the pseudomorphs were divided into three types. The type 1 pseudomorphs, in which the original pyrite was little decomposed, do not have with bleached spots, which corresponds to the spot formation model described previously.

4.3. Other bleached textures in zebra rock

In addition to polygonal dickite pseudomorphs, other bleached textures in the Alu-type zebra rock include dickite pseudomorphs after gypsum, dickite vein, and a dumpling-like clump of sediments (Fig. 14b–e). These bleached textures should be susceptible to the pH changes mentioned earlier.

When the original gypsum dissolved by the infiltrated acidic fluid, the released sulfuric acid could decompose the surrounding Fe oxyhydroxide as shown in Eq. (10). The dissolution of the original gypsum occurs as shown in Eq. (12):

$$Ca(SO_4)\cdot 2H_2O + 2H^+ \rightarrow Ca^{2+} + H_2SO_4 + 2H_2O \quad (12)$$

Gypsum Acidic water Acid sulfate

The bleached areas around the pseudomorphs after gypsum are observed in a white zone with a little Fe oxide precipitation (Fig. 14e). A gypsum-rich layer of ≈5 mm in width is strongly bleached entirely (Fig. 14d). No Fe oxide bands are decomposed around the pseudomorphs after gypsum, indicating that the acidity caused by the dissolution of gypsum may be weaker than that

caused by pyrite oxidation.

The dissolution of Fe oxide minerals also bleaches the area around a dumpling-like clump of sediments. The surrounding laminae are bent in accordance with the shape of clumps (Fig. 13f and 14c), suggesting that the clumps were relatively hard at the time of deposition. Although it is unknown what the clumps were initially composed of, it is presumed that they were a blend of fine-grained quartz and gypsum, similar to a desert rose. As described in Eq. (12), dissolution of gypsum by the acidic fluid formed the bleached texture.

Around the dickite veins, both the Fe oxide bands and the white zone with a little Fe precipitation were also decomposed (Fig. 13d, e and 14b). Two possibilities for the development of bleached areas near the dickite veins include the following:

(a) Fe oxide mineral was decomposed by the reduced fluids at a later stage than the band formation.

(b) During the neutralization reaction (i.e., the band formation) between the acidic fluid and the original rock, the acidic fluid passed through a fracture parallel to the beddings, in which the acidic fluid was less buffered because it went through free spaces and rarely reacted with the rock. To the extent of the diffusion of the unbuffered acidic fluid, the pH of the pore water decreased in the halo of the vein, and Fe oxyhydroxide in the area was dissolved.

The bleached textures described in this study are all connected to the dickite precipitation, indicating that these textures were formed at the same event, although there is currently no evidence to support the process (b) of bleaching around the dickite veins.

5. Conclusions

The following conclusions and recommendations can be summed up through this doctoral study on zebra rock in the Kimberley region, northern Australia, in terms of element migration and precipitation by water–rock interactions:

(1) One of the main findings of detailed modern petrological and geochemical studies conducted on zebra rock shows that zebra rock can be classified into two types, Kao and Alu types, based on mineral assemblages, bulk rock compositions, sedimentary textures, and physical properties, which may indicate the distance from the source of the acidic fluid. From the distribution of the two types of zebra rocks, the spacing of the bands, and the direction of fluid diffusion inferred from the asymmetric Fe concentrations in the bands, it is expected that the pathways of fluid diffusion, pH changes in the fluid, and timescale of the Fe precipitation reaction can be estimated, which can illustrate a picture of the spatio–temporal groundwater system and development of the acidic alteration zone in a regional scale after Proterozoic (Fig. 22a).

(2) The formation model of Fe oxide bands in zebra rock can be described as pH buffering of Fe-bearing acidic fluid by neutralization reactions with siliciclastic materials in the lacustrine sediments. Zebra rock exhibits up to 30 wt% of Fe_2O_3, which is comparable to the Fe concentration found in the crusts of Fe oxide concretion. However, it should be noted that in zebra rock with high grade Fe concentration, Fe oxide bands with high grade Fe concentration rhythmically repeat every few centimeters and the precipitation reaction is continuously progressing on a regional scale. The formation process of Fe oxide bands in

zebra rock highlights the crucial role that pH buffering plays in metal element concentration over a wide area and at high grades. Zebra rock in northern Australia can therefore be considered a miniature metal mineral deposit. Conventionally, pH reactions have been considered as a major mechanism for metal precipitation on a relatively small scale, rather than for mineralization on a large scale. However, future mineral resource exploration efforts should pay more attention to the ideal geochemical conditions for pH buffering.

(3) In addition, the Fe oxide band itself could be used for direct mineral resource exploration. The asymmetrical Fe concentration in each band indicates unidirectional fluid migration, implying that the metal source is upstream and could be located by tracing back the direction (Fig. 22a).

In previous studies of metal deposits and alteration zones, Fe oxide bands have never been described in detail. This could be because the bands are rarely observed, but rather simply because the bands have not been focused as an important feature of element migration. Fe oxide bands may become a powerful indicator for mineral resource exploration if more Fe oxide bands are reported and the relationship between the direction of fluid diffusion and metal source is clarified in the future. One of the important points to be confirmed in the upcoming field observations is the source of Fe iron in zebra rock, which should be verified as a first step toward this application.

Fe oxide bands may also be used to explore mineral resources on Mars. On Mars, the setting for the zebra rock formation is well established because both acid hydrothermal activity related to a volcanism and lacustrine sediments are observed (Solomon et al., 2005; Squyres et al., 2008; Ehlmann et al., 2011a, 2011b). The first mineral resource exploration activity on Mars would occur if a rover discovers rocks with zebra-like banding pattern and

traces back paleocurrents (Fig. 22b).

(4) For the first time, bleached spots in zebra rock have been discovered, and it has been elucidated that the spots represent the extent of localized pH change in the pore water caused by the dissolution of original pyrite on a microscale. Other bleached textures were also observed in zebra rock, and they are thought to be formed due to inorganic processes related to pH changes as well. Although some previous studies have proposed that bleached spots should be explored on Mars because they can be regarded as indirect evidence of life (Parnell et al., 2016; McMahon et al., 2018), this study can propose that bleached spots are not always related to microbial activity, and inorganic process of the spot formation should be considered. The results of this study do not deny that a bleached spot can be a biomarker, but they do emphasize the importance of the central material of the spot, which may be a trigger of spot formation. It is preferable to identify the origin of the central material, such as heavy metal concretions in red sandstones, for the extraterrestrial life exploration by following white spots. This spot search is more likely to provide highly reliable evidence of traces of life (Fig. 22b).

(5) The white bleached spots produced by pyrite oxidation that were observed in this study are also thought to be useful for evaluating the mineralization potential of sediment-hosted copper deposits. Sediment-hosted copper deposit is formed in a basinal setting where copper and other useful metal elements contained in red sandstones are dissolved by high-salinity basinal fluid circulation and precipitate in redox front, such as a stratum of sedimentary rock containing organic materials (e.g., Hitzman et al., 2005). It is known that this type of deposit is difficult to explore because large-scale alteration zones are not

developed around the deposit.

Parnell et al. (2021) emphasized the importance of hinterland of red beds for the mineralization. When red beds are composed of erosion products of a paleo-metal deposit, the sandstones could contain relatively larger amounts of metals, and the secondary deposit in redbeds formed by the basinal high-saline fluid circulation will be more economic. They discussed the correlation between the amount of metal elements contained in hematite gain coating in red sandstone and the volumes of the deposit. However, it is challenging to obtain such trace element analysis field results.

It is likely that the eroded sediments would contain clastic pyrite and that white bleached spots could be created by pyrite oxidation when copper deposits that contain sulfides, such as chalcopyrite and pyrite, were present in the redbeds' hinterland. In other words, it can be said that redbeds with high mineralization potential have a tendency to have more white spots than those without. Because it is simple to locate in the field, this will be a useful indicator in an early-stage exploration for sediment-hosted copper deposits (Fig. 22c). However, it should be noted that the spots could also have resulted from organic matter in the sediment or microbial activities.

It is challenging to determine whether the pyrite was of biogenic or abiogenic origin because the spot formation assumes the dissolution of original pyrite it is unlikely that any original pyrite remains in the spot. Pyrite itself or its traces in the center of bleached spot have not been found in any previous studies. Future research should look for it more carefully because, if it were to be found, the information extracted from the bleached spot would be expanded.

As shown in this study on zebra rock, rocks with band and spot patterns, that have not received

much attention so far, are not only unique ornaments, but important keys recording the mechanisms of element migration and precipitation. Future research should focus on these textures because the information they provide is crucial for the exploration of metal minerals and extraterrestrial life.

Furthermore, the few field investigations that have been done in previous studies of zebra rock, including this one, have only focused on chemical analysis and petrographic description of hand specimens of zebra rock. Field investigations using the new findings from this study may help us understand the history of water–rock reactions in paleo-geochemical events in northern Australia in more detail. The distribution areas of the Ediacaran formation, which contain zebra rock, in northern Australia can be used as a model field for the study of band and spot patterns.

Acknowledgements

I would like to thank H. Yoshida of Nagoya University Museum, N. Katsuta of Gifu University, S. Nishimoto of Aichi University for their constructive discussions and comments on my doctoral study. I sincerely would like to thank K. Yamamoto and A. Umemura of Nagoya University Museum, K. Mimura and Y. Asahara of the geochemical and cosmochemistry laboratory of Nagoya University, and R. Kuma of the Institute for Space-Earth Environmental Research of Nagoya University for their advice on the geochemical analyses (XRF, CHNS, XGT, XRD and SEM-EDX). I am grateful to Y. Kouketsu of the petrology group of Nagoya University for providing the equipment for microscopic observations and petrological analyses (Raman spectroscopy and EPMA). Moreover, M. Takeuchi, K. Tsukada of Nagoya University, Y. Muramiya of Fukada Geological Institute and other members of the tectonics group of Nagoya University provided effective comments on this study. The XANES analysis was performed in the Horonobe Research Institute for the Subsurface Environment. I would also like to acknowledge the support of the subsidization scheme to acquire my doctoral degree provided by the Japan Organization for Metals and Energy Security (JOGMEC).

References

Abrajevitch, A., Pillans, B.J., Roberts, A.P., Kodama, K., 2018. Magnetic properties and paleomagnetism of Zebra Rock, Western Australia: chemical remanence acquisition in hematite pigment and Ediacaran geomagnetic field behavior. Geochem. Geophys. Geosyst. 19, 732–748. https://doi.org/10.1002/2017GC007091.

Anderson, S.P., Dietrich, W.E., Brimhall, G.H., 2002. Weathering profiles, mass-balance analysis, and rates of solute loss: linkages between weathering and erosion in a small, steep catchment. Geol. Soc. Am. Bull. 114, 1143–1158. https://doi.org/ 10.1130/0016-7606(2002)114<1143:WPMBAA>2.0.CO;2.

Andeskie, A.S., 2016. Depositional and Diagenetic History of the Triassic Redbeds and Evaporites from the Mercia Mudstone Group in the Carnduff 02 Core of County Antrim, Northern Ireland. West Virginia University.

Andeskie, A.S., Benison, K.C., Eichenlaub, L.A., Raine, R., 2018. Acid-saline-lake systems of the Triassic Mercia Mudstone Group, County Antrim, Northern Ireland. Journal of Sedimentary Research. 88, 385–398. https://doi.org/10.2110/jsr.2018.14.

Beitler, B., Chan, M. A., & Parry, W. T., 2003. Bleaching of Jurassic Navajo Sandstone on Colorado Plateau Laramide highs: evidence of exhumed hydrocarbon supergiants?. Geology. 31, 1041–1044. https://doi.org/10.1130/G19794.1.

Benison, K.C., Goldstein, R.H., 2001. Evaporites and siliciclastics of the Permian Nippewalla Group of Kansas, USA: a case for non-marine deposition in saline lakes and saline pans. Sedimentology. 48, 165–188. https://doi.org/10.1046/j.1365-3091.2001.00362.x.

Benison, K.C., Knapp, J.P., Dannenhoffer, J.M., 2011. The Pennsylvanian Pewamo Formation and associated Haybridge strata: toward the resolution of the Jurassic Ionia red bed problem in the Michigan Basin, USA. Journal of Sedimentary Research. 81, 459–478. https://doi.org/10.2110/jsr.2011.039.

Bevan, A.W.R., 2001. Zebra rock: an ornamental stone from the east Kimberley, western Australia. Aust. Gemmol. 21, 165–168.

Borradaile, G. J., 1988. Magnetic susceptibility, petrofabrics and strain. Tectonophysics, 156, 1–20. https://doi.org/10.1016/0040-1951(88)90279-X

Borradaile, G. J., 1991. Correlation of strain with anisotropy of magnetic susceptibility (AMS). Pure and applied geophysics, 135, 15–29.

Bossart, P., Dietrich, D., Greco, A., Ottiger, R., Ramsay, J.G., 1988. The tectonic structure of the Hazara-Kashmir syntaxis, southern Himalayas, Pakistan. Tectonics. 7, 273–297. https://doi.org/10.1029/TC007i002p00273.

Bossart, P., Ottiger, R., Heller, F., 1990. Rock magnetic properties and structural development in the core of the Hazara-Kashmir Syntaxis, NE Pakistan. Tectonics. 9, 103–121. https://doi.org/10.1029/TC009i001p00103.

Budurov, K., Zagorcev, I., Trifonova, E., 1993. The Triassic tn Southwest Bulgaria. Upper Triassic red beds (Moesian Group) m the Golo-bardo unit. Geologica Balcanjca. 23, 35–45.

Chan, M.A., Parry, W.T., Bowman, J.R., 2000. Diagenetic hematite and manganese oxides and fault-related fluid flow in Jurassic sandstones, southeastern Utah. AAPG Bull. 84, 1281–1310. https://doi.org/10.1306/A9673E82-1738-11D7- 8645000102C1865D.

Chan, M.A., Beitler, B., Parry, W.T., Ormö, J., Komatsu, G., 2004. A possible terrestrial analogue for haematite concretions on Mars. Nature. 429, 731–734. https://doi.org/10.1038/nature02600

Chen, C., Barcellos, D., Richter, D.D., Schroeder, P. A., Thompson, A., 2019. Redoximorphic Bt horizons of the Calhoun CZO soils exhibit depth-dependent iron-oxide crystallinity. Journal of Soils and Sediments, 19, 785–797. https://doi.org/10.1007/s11368-018-2068-2.

Cleveland, D.M., Nordt, L.C., Atchley, S.C., 2008. Paleosols, trace fossils, and precipitation estimates of the uppermost Triassic strata in northern New Mexico. Palaeogeography, Palaeoclimatology, Palaeoecology. 257, 421–444. https://doi.org/10.1016/j.palaeo.2007.09.023.

Cogné, J.P., Gapais, D., 1986. Passive rotation of hematite during deformation: a comparison of simulated and natural redbeds fabrics. Tectonophysics, 121, 365–372. https://doi.org/10.1016/0040-1951(86)90057-0

Cogné, J.P., 1988. Strain, magnetic fabric, and paleomagnetism of the deformed red beds of the Pont-Rean formation, Brittany, France. Journal of Geophysical Research: Solid Earth. 93, 13673–13687. https://doi.org/10.1029/JB093iB11p13673.

Corkeron, M., 2007. “Cap carbonates” and Neoproterozoic glacigenic successions from the Kimberley region, north-west Australia. Sedimentology 54, 871–903. https:// doi.org/10.1111/j.1365-3091.2007.00864.x.

Corkeron, M., 2008. Deposition and palaeogeography of a glacigenic Neoproterozoic succession in the east Kimberley, Australia. Sediment. Geol. 204, 61–82. https://doi.

org/10.1016/j.sedgeo.2007.12.010.

Cowley, W.M., 1993. Cariewerloo Basin. In JF Drexel, WV Preiss and AJ Parker eds, The geology of South Australia, Volume 1, The Precambrian, Bulletin 54. Geological Survey of South Australia, Adelaide, 139–142.

Curiale, J.A., Bloch, S., Rafalska-Bloch, J., Harrison, W.E., 1983. Petroleum-related origin for uraniferous organic-rich nodules of southwestern Oklahoma. AAPG Bull. 67, vii. https://doi.org/10.1306/03B5B664-16D1-11D7-8645000102C1865D.

Dow, D.B., Gemuts, I., 1969. Geology of the Kimberley Region, Western Australia: the East Kimberley. Geol. Surv. Western Aust. Bull. 120.

Dunster, J.N., Beier, P.R., Burgess, J.M., Cutovinos, A. Auvergne, 2000. Nothern Territory 1:250,000 Geological Series Explanatory Notes SD 52–15. In: Northern Territory Geological Survey, Darwin.

Dunster, J.N., Beier, P., Cutovinos, A., 2013. Waterloo, Northern Territory (Revised Second Edition). 1:250,000 geological map series, SE 52–03. In: Northern Territory Geological Survey, Darwin.

Durrance, E.M., Meads, R.E., Ballard, R.R.B., Walsh, J.N., 1978. Oxidation state of iron in the Littleham Mudstone Formation of the New Red Sandstone Series (Permian- Triassic) of Southeast Devon, England. Geol. Soc. Am. Bull. 89, 1231–1240. https:// doi.org/10.1130/0016-7606(1978)89<*1231:OSOIIT*>*2.0.CO;2.*

Durrance, E.M., Meads, R.E., Brindley, R.K., Stark, A.G.W., 1980. Radioactive disequilibrium in uranium-bearing nodules from the New Red Sandstone (Permian-Triassic) of Budleigh

Salterton, Devon. Proceedings of the Ussher Society. 5, 81–88.

Ehlmann, B.L., Mustard, J.F., Clark, R.N., Swayze, G.A., Murchie, S.L., 2011a. Evidence for low-grade metamorphism, hydrothermal alteration, and diagenesis on Mars from phyllosilicate mineral assemblages. Clay Clay Miner. 59, 359–377. https://doi.org/10.1346/CCMN.2011.0590402.

Ehlmann, B.L., Mustard, J.F., Murchie, S.L., Bibring, J.P., Meunier, A., Fraeman, A.A., Langevin, Y., 2011b. Subsurface water and clay mineral formation during the early history of Mars. Nature. 479, 53–60. https://doi.org/10.1038/nature10582.

Eichhubl, P., Davatz, N.C., Becker, S.P., 2009. Structural and diagenetic control of fluid migration and cementation along the Moab fault, Utah. AAPG Bull. 93, 653–681. https://doi.org/10.1306/02180908080.

Evins, L.Z., Jourdan, F., Philips, D., 2009. The Cambrian Kalkarindji Large Igneous Province: extent and characteristics based on new 40Ar/39Ar and geochemical data. Lithos 110, 294–304. https://doi.org/10.1016/j.lithos.2009.01.014.

Fox, D.C., Spinks, S.C., Thorne, R.L., Barham, M., Aspandiar, M., Armstrong, J.G., Uysal, T., Timms, N.E., Pearse, M.A., Verrall, M., Godel, B., Whisson, B., 2020. Mineralogy and geochemistry of atypical reduction spheroids from the Tumblagooda Sandstone, Western Australia. Sedimentology. 67, 677–698. https://doi.org/10.1111/sed.12659

Fu, L., Milliken, K.L., Sharp, J.M., 1994. Porosity and permeability variations in fractured and liesegang-banded Breathitt sandstones (Middle Pennsylvanian), eastern Kentucky; diagenetic controls and implications for modelling dual-porosity systems. J. Hydrol. 154, 351–381.

https://doi.org/10.1016/0022-1694(94)90225-9.

Geidans, L., 1981. Zebra rock of Western Australia. Admin. Geol. Soc. Aust. 3, 22.

Glass, L.M., Phillips, D., 2006. The Kalkarindji continental flood basalt province: a new Cambrian large igneous province in Australia with possible links to faunal extinctions. Geology 34, 461–464. https://doi.org/10.1130/G22122.1.

Glotch, T.D., Morris, R.V., Christensen, P.R., and Sharp, T.G., 2004. Effect of precursor mineralogy on the thermal infrared emission spectra of hematite: Application to Martian hematite mineralization. Journal of Geophysical Research: Planets, 109(E7). https://doi.org/10.1029/2003JE002224

Gilfillan, S.M., Ballentine, C.J., Holland, G., Blagburn, D., Lollar, B.S., Stevens, S., Schoell, M., Cassidy, M., 2008. The noble gas geochemistry of natural CO_2 gas reservoirs from the Colorado Plateau and Rocky Mountain provinces, USA. Geochimica et Cosmochimica Acta. 72, 1174–1198. https://doi.org/10.1016/j.gca.2007.10.009.

Gorjan, P., Veevers, J.J., & Walter, M.R., 2000. Neoproterozoic sulfur-isotope variation in Australia and global implications. Precambrian Research. 100, 151–179. https://doi.org/10.1016/S0301-9268(99)00073-X.

Gray, M.B., Nickelsen, R.P., 1989. Pedogenic slickensides, indicators of strain and deformation processes in redbed sequences of the Appalachian foreland. Geology. 17, 72–75. https://doi.org/10.1130/0091-7613(1989)017<0072:PSIOSA>2.3.CO;2.

Hamimi, Z., Hagag, W., Osman, R., El-Bialy, M., Abu El-Nadr, I., Fadel, M., 2018. The active Kalabsha Fault Zone in Southern Egypt: detecting faulting activity using field-structural data

and EMR-technique, and implications for seismic hazard assessment. Arabian Journal of Geosciences. 11, 1–20. https://doi.org/10.1007/s12517-018-3774-1.

Harrison, R.K., Treshman, A.E., Young, B.R. and Lawson, R.I., 1975. Concretionary concentrations of the rarer elements in Permo-Triassic red beds of south-west England. Bull. Geol. Surv., G.B.; G.B.; 1975, NUM. 0052, P. 1 A 26.

Harrison, R.K., 2010. The Permo-Triassic of South Devon, England. Geoscience in South-West England. 12, 198–200.

He, W., Yang, Z., Du, H., Hu, J., Zhang, K., Hou, W., Li, H., 2022. Micro-Mechanisms and Implications of Continental Red Beds. Minerals. 12, 934. https://doi.org/10.3390/min12080934

Hirt, A.M., Lowrie, W., Pfiffner, O.A., 1986. A paleomagnetic study of tectonically deformed red beds of the Lower Glarus Nappe Complex, Eastern Switzerland. Tectonics, 5, 723–731. https://doi.org/10.1029/TC005i005p00723.

Hitzman, M., Kirkham, R., Broughton, D., Thorson, J., and Selley, D., 2005. The sediment-hosted stratiform copper ore system. ECONOMIC GEOLOGY 100TH ANNIVERSARY VOLUME, 609–642. https://doi.org/10.5382/AV100.19

Hobson, R.A., 1930. Zebra rock from Kimberley. J. R. Soc. West. Aust. 16, 57–70.

Hofmann, B.A., 1990. Reduction spheroids from northern Switzerland: mineralogy, geochemistry and genetic models. Chem. Geol. 81, 55–81. https://doi.org/10.1016/ 0009-2541(90)90039-A.

Hofmann, B.A., 1991a. Mineralogy and geochemistry of reduction spheroids in red beds. Mineral. Petrol. 44, 107–124. https://doi.org/10.1007/BF01167103.

Hofmann, B.A., 1991b. An uranium series disequilibrium investigation of reduction spheroids in red beds. Schweiz. mineralog. petrogr. Mitt. 71, 333–340.

Hofmann, B.A., 1993. Organic matter associated with mineralized reduction spots in red beds. In Bitumens in Ore Deposits (pp. 362–378). Springer, Berlin, Heidelberg. https://doi.org/10.1007/978-3-642-85806-2_19.

Hofmann, B.A., 1999. Geochemistry of natural redox fronts – a review. Technical Report 99-05, Nagra, pp. 1–156.

Jourdan, F., Hodge, K., Sell, B., Schaltegger, U., Wingate, M.T.D., Evins, L.Z., S¨oderlund, U., Haines, P.W., Phillips, D., Blenkinsop, T., 2014. High-precision dating of the Kalkarindji large igneous province, Australia, and synchrony with the Early–Middle Cambrian (Stage 4–5) extinction. Geology 42, 543–546. https://doi. org/10.1130/G35434.1.

Jurjovec, J., Ptacek, C. J., Blowes, D.W., 2002. Acid neutralization mechanisms and metal release in mine tailings: a laboratory column experiment. Geochimica et Cosmochimica Acta. 66, 1511–1523. https://doi.org/10.1016/S0016-7037(01)00874-2

Kampman, N., Bickle, M., Wigley, M., et al., 2014. Fluid flow and CO2–fluid–mineral interactions during CO2-storage in sedimentary basins. Chem. Geol. 369, 22–50. https://doi.org/10.1016/j.chemgeo.2013.11.012.

Katsuta, N., Takano, M., Okaniwa, T., Kumazawa, M., 2003. Image processing to extract sequential profiles with high spatial resolution from the 2D map of deformed laminated

patterns. Comput. Geosci. 29, 725–740. https://doi.org/10.1016/S0098- 3004(03)00021-9.

Katsuta, N., Miyata, Y., Murakami, T., Mino, Y., Naito, S., Yasuda, K., Ochiai, S., Abe, O., Yasuda, A., Morimoto, M., Kawakami, S., Nagao, S., 2019. Interannual changes in radiocesium concentrations in annually laminated tufa following the Fukushima Daiichi Nuclear Power Plant accident. Appl. Geochem. 102, 34–43. https://doi.org/ 10.1016/j.apgeochem.2019.01.002.

Katsuta, N., Sirono, S., Umemura, A., Kawahara, H., Yoshida, H., 2022. Applications of micro-X-ray fluorescence mapping to iron bands in iron-oxide concretion to evaluate its formation and reaction rate. J. Geol. Soc. Japan. 128, 81–86 (in Japanese). https://doi.org/10.5575/geosoc.2022.0008

Kawahara, H., Yoshida, H., Yamamoto, K., Katsuta, N., Nishimoto, S., Umemura, A., Kuma, R., 2022a. Hydrothermal formation of Fe-oxide bands in zebra rocks from northern Western Australia. Chem. Geol. 590, 120699 https://doi.org/10.1016/j. chemgeo.2021.120699.

Kawahara, H., Yoshida, H., Nishimoto, S., Kouketsu, Y., Katsuta, N., Umemura, A., 2022b. Bleached-spot formation in Fe-oxide-rich rock by inorganic process. Chemical Geology, 609, 121049. https://doi.org/10.1016/j.chemgeo.2022.121049.

Kemp, A.J., Palmer, M.R., Ragnarsdottir, K.V., 1994. The uranium-thorium and rare earth element geochemistry of reduction nodules from Budleigh Salterton, Devon. PROCEEDINGS-USSHER SOCIETY. 8, 214–214.

Kemp, A.J., Powell, S.J., Palmer, M.R., Ragnarsdottir, K.V., 1996. Computer aided analysis of x-ray images in mudstone concretions from Budleigh Salterton, Devon. PROCEEDINGS-

USSHER SOCIETY. 9, 041–044.

Kligfield, R., Owens, W.H., Lowrie, W., 1981. Magnetic susceptibility anisotropy, strain, and progressive deformation in Permian sediments from the Maritime Alps (France). Earth and Planetary Science Letters. 55, 181–189. https://doi.org/10.1016/0012-821X(81)90097-2

Kligfield, R., Lowrie, W., Hirt, A., Siddans, A.W.B., 1983. Effect of progressive deformation on remanent magnetization of Permian redbeds from the Alpes Maritimes (France). Tectonophysics. 98, 59–85. https://doi.org/10.1016/0040-1951(83)90211-1.

Kneen, S.J., 1976. The relationship between the magnetic and strain fabrics of some haematite-bearing Welsh slates. Earth and Planetary Science Letters. 31, 413–416. https://doi.org/10.1016/0012-821X(76)90123-0.

Lambert, I.B., Donnelly, T.H., Dunlop, J.S.R., Groves, D.I., 1978. Stable isotopic compositions of early Archaean sulphate deposits of probable evaporitic and volcanogenic origins. Nature 276, 808–810. https://doi.org/10.1038/276808a0.

Larcombe, C.O.G., 1924. Rock specimens from Ord River and Oakover River respectively. In: Geological Survey of Western Australia, Annual Report. 19.

Lines, A., Parnell, J., Mossman, D., 1996. Reduction spheroids from the Upper Carboniferous Hopewell Group, Dorchester Cape, New Brunswick: notes on geochemistry, mineralogy and genesis. Atlantic Geology. 32, 159–172. https://id.erudit.org/iderudit/ageo32_2art06

Lottermoser, B., 2007. Mine Wastes: Characterization, Treatment and Environmental Impacts, 2nd edn. Springer, New York.

Loughnan, F.C., Roberts, F.I., 1990. Composition and origin of the ‘zebra rock’ _from the East Kimberley region of Western Australia. Aust. J. Earth Sci. 37, 201–205. https://doi.org/10.1080/08120099008727920.

Mattievich, E., Chadwick, J., Cashion, J.D., Boas, J.F., Clark, M.J., Mackie, R.D., 2002. A ferronematic liquid crystal phase in Precambrian zebra rock from the Kimberley region. Ann. Cond. Matt. Phys. Meet. Conference Handb., Australia, 26, 66 p.

Mattievich, E., Chadwick, J., Cashion, J.D., Boas, J.F., Clark, M.J., Mackie, R.D., 2003. Macroscopic ferronematic liquid crystals determine the structure of Kimberley Zebra Rock (Paper presentation). In: Ann. Cond. Matt. Phys. Meet. Conf. Handb., Australia, 27, 3 pp. Available from. http://www.aip.org.au/wp-content/uploads/cmm/ 2003/WW03_33.pdf, 2003.

McMahon, S., Hood, A.V.S., Parnell, J., Bowden, S., 2018. Reduction spheroids preserve a uranium isotope record of the ancient deep continental biosphere. Nature Comm. 9, 4505. https://doi.org/10.1038/s41467-018-06974-9.

Michalzik, D., 1991. Facies sequence of Triassic-Jurassic red beds in the Sierra Madre Oriental (NE Mexico) and its relation to the early opening of the Gulf of Mexico. Sedimentary geology. 71, 243–259. https://doi.org/10.1016/0037-0738(91)90105-M.

Miller Jr, D.N., 1966. Petrology of Pierce Canyon Redbeds, Delaware Basin, Texas and New Mexico. AAPG Bulletin. 50, 283–307. https://doi.org/10.1306/5D25B487-16C1-11D7-8645000102C1865D.

Milodowski, A.E., Styles, M.T., Hards, V.L., 2000. A natural analogue for copper waste canisters: The copper-uranium mineralised concretions in the Permian mudrocks of south

Devon, United Kingdom (No. SKB-TR--00-11). Swedish Nuclear Fuel and Waste Management Co..

Milodowski, A.E., Styles, M.T., Horstwood, M.S.A., Kemp, S.J., 2002. Alteration of uraniferous and native copper concretions in the Permian mudrocks of south Devon, United Kingdom (No. SKB-TR--02-09). Swedish Nuclear Fuel and Waste Management Co..

Murakami, T., Takamatsu, T., Katsuta, N., Takano, M., Yamamoto, K., Takahashi, Y., Nakamura, T., Kawai, T., 2012. Centennial- to millennial-scale climate shifts in continental interior Asia repeated between warm-dry and cool-wet conditions during the last three interglacial states: evidence from uranium and biogenic silica in the sediment of Lake Baikal, Southeast Siberia. Quat. Sci. Rev. 52, 49–59. https://doi. org/10.1016/j.quascirev.2012.08.001.

Mykura, H., Hampton, B.P., 1984. On the mechanism of formation of reduction spots in the Carboniferous/Permian red beds of Warwickshire. Geol. Mag. 121, 71–74. https://doi.org/10.1017/S0016756800027965.

Olivarius, M., Weibel, R., Hjuler, M. L., Kristensen, L., Mathiesen, A., Nielsen, L.H., Kjøller, C., 2015. Diagenetic effects on porosity–permeability relationships in red beds of the Lower Triassic Bunter Sandstone Formation in the North German Basin. Sedimentary Geology. 321, 139–153. https://doi.org/10.1016/j.sedgeo.2015.03.003.

Olsen, P.E., Geissman, J. W., Kent, D.V., Gehrels, G.E., Mundil, R., Irmis, R.B., Lepre, C., Rasmussen, C., Giesler, D., Parker, W.G., Zakharova, N., Kürschner, W.N., Miller, C., Baranyi, V., Schaller, M.F., Whiteside, J.H., Schnurrenberger, D., Noren, A., Shannon, K.B., O'Grady, R., Colbert, M.W., Maisano, J., Edey, D., Kinney, S.T., Molina-Garza, M., Bachman, G.H., Sha, J., the CPCD team, 2018. Colorado plateau coring project, phase I

(CPCP-I): A continuously cored, globally exportable chronology of Triassic continental environmental change from Western North America. Scientific Drilling, 24, 15–40. https://doi.org/10.5194/sd-24-15-2018.

Ormö, J., Komatsu, G., Chan, M.A., Beitler, B. and Parry, W. T., 2004. Geological features indicative of processes related to the hematite formation in Meridiani Planum and Aram Chaos, Mars: A comparison with diagenetic hematite deposits in southern Utah, USA. Icarus. 171, 295–316. https://doi.org/10.1016/j.icarus.2004.06.001

Ortoleva, P.J., 1984. The self-organization of liesegang bands and other precipitate patterns. In: Chemical Instabilities: Applications in Chemistry, Engineering, Geology, and Materials Science: (ed. G.Nicols & F.Baras), pp. 289–297.

Ortoleva, P.J., 1993. Self-organization and nonlinear dynamics in sedimentary basins. Philos. Trans. R. Soc. Lond. A 344, 171–179. https://doi.org/10.1098/ rsta.1993.0085.

Parnell, J., 1985. Uranium/rare earth-enriched hydrocarbons in Devonian sandstones, northern Scotland. Neues Jahrbuch für Mineralogie Monatshefte. 3, 132–144.

Parnell, J., Eakin, P., 1987. The replacement of sandstones by uraniferous hydrocarbons: significance for petroleum migration. Min. Mag. 51, 505–515. https://doi.org/ 10.1180/minmag.1987.051.362.05.

Parnell, J., 1988. The mineralogy of red bed uranium-vanadium mineralization in the Permo-Triassic of Belfast. Irish Journal of Earth Sciences, 119–124. https://www.jstor.org/stable/30002478.

Parnell, J., Brolly, C., Spinks, S., Bowden, S., 2016. Metalliferous biosignatures for deep

subsurface microbial activity. Orig. Life Evol. Biosph. 46, 107–118. https://doi.org/10.1007/s11084-015-9466-x.

Parnell, J., Spinks, S., Brolly, C., 2018. Tellurium and selenium in Mesoproterozoic red beds. Precambrian Research, 305, 145–150. https://doi.org/10.1016/j.precamres.2017.12.022

Perutz, M., 1939. Radioactive nodules from Devonshire, England. Zeitschrift für Kristallographie, Mineralogie und Petrographie, 51(1), 141–161. https://doi.org/10.1007/BF02945541.

Pešek, J., Skoček, V., 1999. Alluvial-lacustrine red beds in Upper Paleozoic continental basins, Bohemian Massif, Czech Republic (Vol. 11). Czech Geological Survey.

Potter, S.L., Chan, M.A., Petersen, E.U., Dyar, M.D., Sklute, E., 2011. Characterization of Navajo Sandstone concretions: Mars comparison and criteria for distinguishing diagenetic origins. Earth and Planetary Science Letters. 301, 444–456. https://doi.org/10.1016/j.epsl.2010.11.027

Rainoldi, A.L., Franchini, M., Beaufort, D., Patrier, P., Giusiano, A., Impiccini, A., Pons, J., 2014. Large-scale bleaching of red beds related to upward migration of hydrocarbons: Los Chihuidos High, Neuquen Basin, Argentina. Journal of Sedimentary Research. 84, 373–393. https://doi.org/10.2110/jsr.2014.31.

Retallack, G.J., 2021. Zebra rock and other Ediacaran paleosols from Western Australia. Aust. J. Earth Sci. 68, 532–556. https://doi.org/10.1080/08120099.2020.1820574.

Retallack, G.J., 2022. Comment on “Kawahara, H., Yoshida, H., Yamamoto, K., Katsuta, N., Nishimoto, S., Umemura, A., Kuma, R., 2022. Hydrothermal formation of Fe-oxide bands in

zebra rocks from northern Western Australia. Chemical Geology 590 (2022), 120699". Chemical Geology, 121105. https://doi.org/10.1016/j.chemgeo.2022.121105.

Richards, J.P. and Mumin, A.H., 2013. Magmatic-hydrothermal processes within an evolving Earth: Iron oxide-copper-gold and porphyry Cu ± Mo ± Au deposits. Geology. 41. 767–770. https://doi.org/10.1130/G34275.1

Rudnick, R.L., Gao, S., Holland, H.D., Turekian, K.K., 2003. Composition of the continental crust. *The crust*. 3, 1–64.

Rye, R.O., 2005. A review of the stable-isotope geochemistry of sulfate minerals in selected igneous environments and related hydrothermal systems. Chemical Geology. 215, 5–36.

Sirono, S., Shibata, T., Katsuta, N., Yoshida, H., 2021. Numerical simulation of iron oxide concretions on Earth and Mars through calcite dissolution. Geochim. Cosmochim. Acta 295, 194–206. https://doi.org/10.1016/j.gca.2020.12.017.

Solomon, S.C., Aharonson, O., Aurnou, J.M., Banerdt, W.B., Carr, M.H., Dombard, A.J., Zuber, M.T., 2005. New perspectives on ancient Mars. Science 307, 5713. https://doi.org/10.1126/science.1101812.

Spinks, S.C., Parnell, J., Bowden, S.A., 2010. Reduction spots in the Mesoproterozoic age: implications for life in the early terrestrial record. Int. J. Astrobiol. 9, 209–216. https://doi.org/10.1017/S1473550410000273.

Spinks, S.C., Parnell, J., Still, J.W., 2014. Redox-controlled selenide mineralization in the Upper Old Red Sandstone. Scottish Journal of Geology. 50, 173–182. https://doi.org/10.1144/sjg2013-014.

Squyres, S.W., Grotzinger, J.P., Arvidson, R.E., Bell III, J.F., Calvin, W., Christensen, P.R., Clark, B.C., Crisp, J.A., Farrand, W.H., Herkenhoff, K.E., Johnson, J.R., Klingelhöfer, G., Knoll, A.H., McLennan, S.M., McSween, Jr. H.Y., Morris, R.V., Rice, Jr. J.W., Rieder, R., and Soderblom, L.A., 2004. In situ evidence for an ancient aqueous environment at Meridiani Planum, Mars. Science. 306, 1709-1714.

Squyres, S.W., Arvidson, R.E., Ruff, S., Gellert, R., Morris, R.V., Ming, D.W., de Souza Jr, P.A., 2008. Detection of silica-rich deposits on Mars. Science 320, 5879. https://doi.org/10.1126/science.1155429.

Sweet, I.P., 1973. Waterloo, Northern Territory. 1:250,000 Geological Map Series Explanatory Notes, SE 52–03. Bureau of Mineral Resources, Australia, Canberra.

Thorne, A.M., Sheppard, S., Tyler, I.M. Lissadell, Western Australia, 1999. 1:250,000 Geological Map Series and Explanatory Notes, SE 52–2, 2nd ed. Geological Survey of Western Australia.

Tirsgaard, H., Øxnevad, I.E., 1998. Preservation of pre-vegetational mixed fluvio–aeolian deposits in a humid climatic setting: an example from the Middle Proterozoic Eriksfjord Formation, Southwest Greenland. Sedimentary Geology. 120, 295–317. https://doi.org/10.1016/S0037-0738(98)00037-2.

Tucker, M.E., 1976. Replaced evaporites from the lake Precambrian of Finnmark, Arctic Norway. Sediment. Geol. 16, 193–204. https://doi.org/10.1016/0037-0738(76) 90031-2.

Tyler, I.M., Thorne, A.M., Sheppard, S., Hoatson, D.M., Griffin, T.J., Blake, D.H., Dixon, Warren R.G., Range, W.A., 1998. Sheet SE 52–6: Western Australia Geological Survey,

1:250,000 Geological Series. Geological Survey of Western Australia.

Van de Poll, H.W., Sutherland, J.K., 1976. Cupriferous reduction spheres in Upper Mississippian redbeds of the Hopewell Group at Dorchester Cape, New Brunswick. Can. J. Earth Sci. 13, 781–789. https://doi.org/10.1139/e76-081.

Wang, Y., Chan, M., Merino, E., 2015. Self-organized Fe-oxide cementation geometry as an indicator of paleo-flows. Sci. Rep. 5, 10792. https://doi.org/10.1038/srep10792, 26123788.

Wells, N.A., Gingerich, P.D., 1987. Paleoenvironmental interpretation of Paleogene strata near Kotli, Azad Kashmir, Northeastern Pakistan. Kashmir Journal of Geology. 5, 23–41.

Weibel, R., 1998. Diagenesis in oxidising and locally reducing conditions—an example from the Triassic Skagerrak Formation, Denmark. Sedimentary Geology. 121, 259–276. https://doi.org/10.1016/S0037-0738(98)00085-2.

Weibel, R., Friis, H., 2004. Opaque minerals as keys for distinguishing oxidising and reducing diagenetic conditions in the Lower Triassic Bunter Sandstone, North German Basin. Sedimentary Geology, 169, 129–149. https://doi.org/10.1016/j.sedgeo.2004.05.004.

Weil, A.B., Yonkee, W.A., Sussman, A.J., 2010. Reconstructing the kinematics of thrust sheet rotation: a paleomagnetic study of Triassic redbeds from the Wyoming Salient, USA. Geol. Soc. Am. Bull. 122, 2–23.

White, B., 1981. Shallowing-upward cycles in the Middle Proterozoic Altyn Formation. Nature 294, 157–158. https://doi.org/10.1038/294157a0, 29451241.

Wigley, M., Kampman, N., Dubacq, B., Bickle, M., 2012. Fluid-mineral reactions and trace

metal mobilization in an exhumed natural CO2 reservoir, Green River, Utah. Geology 40, 555–558. https://doi.org/10.1130/G32946.1.

Wilke, M., Farges, F., Petit, P.-E., Brown Jr., G.E., Martin, F., 2001. Oxidation state and coordination of Fe in minerals: an Fe K-XANES spectroscopic study. Am. Mineral. 86, 714–730. https://doi.org/10.2138/am-2001-5-612.

Wood, D.S., Oertel, G., Singh, J., Bennett, H.F., Tarling, D.H., 1976. Strain and Anisotropy in Rocks. Phil. Trans. R. Soc. of Lond. A. 283, 27–42. https://www.jstor.org/stable/74627.

Yang, Y., Fu, W., Yu, J., Ning, Z., Cui, J., Li, Q., Wang, X., Zhuo, X., 2019. Formation Mechanism of Reduction Spheroids with Dark Cores in Cretaceous Red Beds in Jiaolai Basin, China. Open Journal of Geology. 9, 707–710. 10.4236/ojg.2019.910081.

Yoshida, H., Matsuoka, K., 2004. Occurrence of 'Takashikozo' from Takashihara area, Aichi-Prefecture. Bull. Nagoya Univ. Museum. 20, 25–34 (in Japanese with English abstract).

Yoshida, H., Yamamoto, K., Murakami, Y., Katsuta, N., Hayashi, T. and Naganuma, T. (2008). The development of Fe-nodules surrounding biological material mediated by microorganisms. Environmental Geology, 55(6), 1363-1374.

Yoshida, H., Katsuta, N., Metcalfe, R., 2014. 'Fish-eye'type concretions: A possible analogue of radionuclide migration and retardation in rock matrices around buried HLW container. The Journal of the Geological Society of Japan. 120, IX-X. https://doi.org/10.5575/geosoc.2014.0029.

Yoshida, H., Hasegawa, H., Katsuta, N., Maruyama, I., Shirono, S., Minami, M., Asahara, Y., Nishimoto, S., Yamaguchi, Y., Ichinnorov, N., Metcalfe, R., 2018. Fe-oxide concretions

formed by interacting carbonate and acidic waters on Earth and Mars. Sci. Adv. 4 (eaau0872). https://doi.org/10.1126/sciadv.aau0872, 30525103.

Yoshida, H., Katsuta, N., Shirono, S., Nishimoto, S., Kawahara, H., Metcalfe, R., 2020. Concentric Fe-oxyhydroxide bands in dacite cobbles: rates of buffering chemical reactions. Chem. Geol. 552, 119786 https://doi.org/10.1016/j. chemgeo.2020.119786.

Figures and Tables

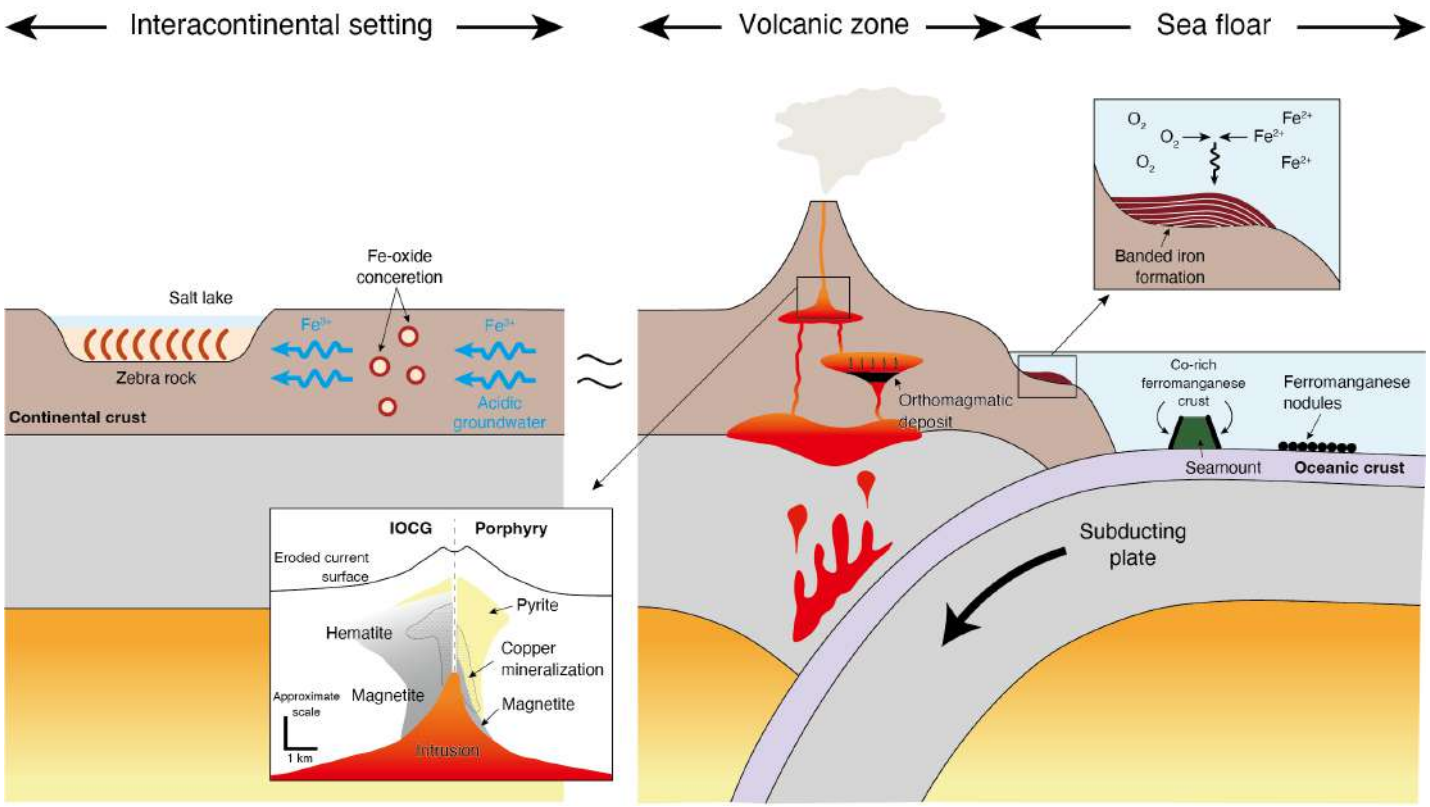

Fig. 1 Major iron concentration settings in the crust on the Earth (not to scale). The image of porphyry/IOCG deposits is simplified from Richards and Mumin (2013).

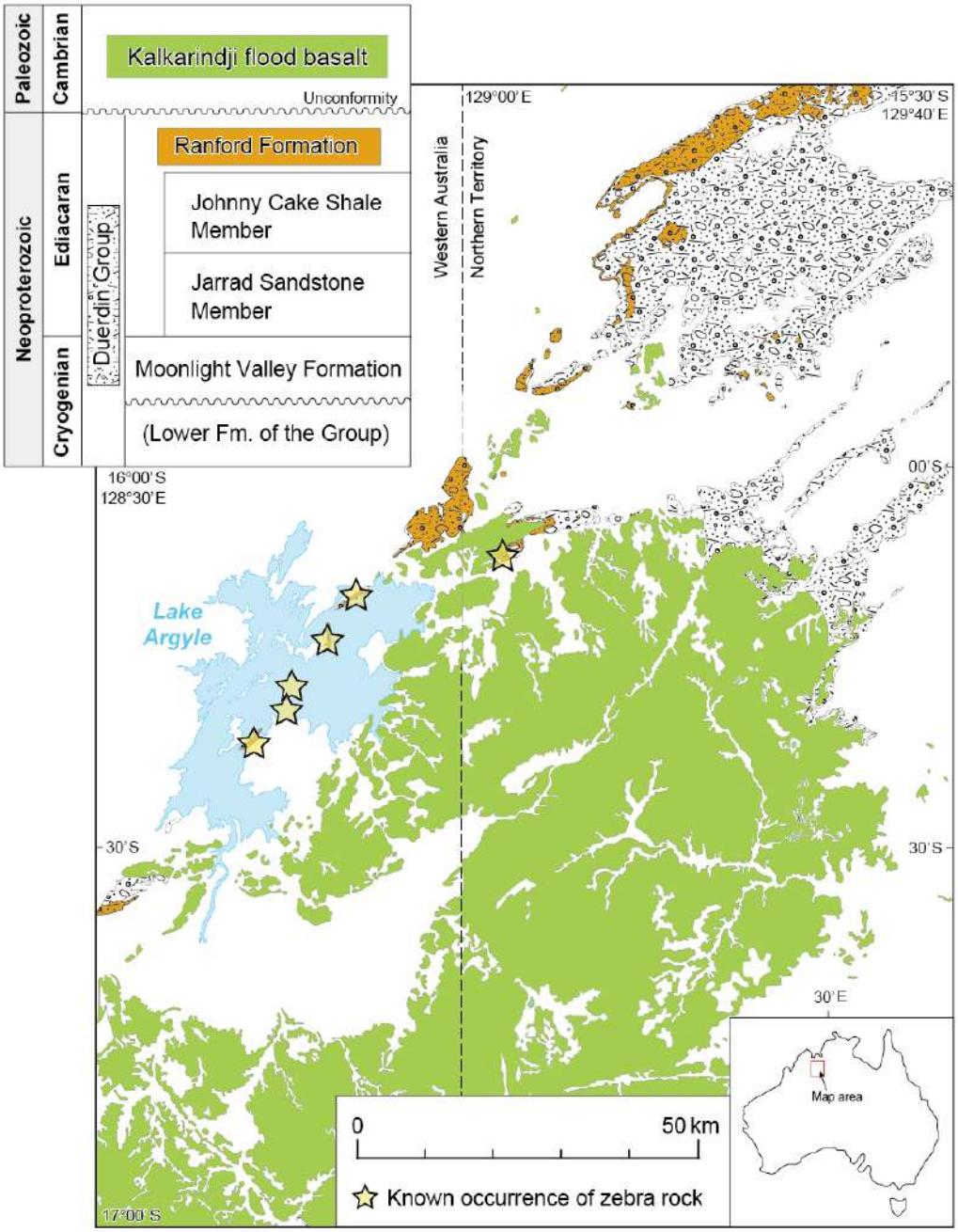

Fig. 2 Zebra rock occurrences with related lithologies and simple lithostratigraphy in northern Australia. The Ediacaran Ranford Formation (brown) of the Neoproterozoic Duerdin Group (pattern) and the Cambrian Kalkarindji flood basalt (green) have been depicted on the map (combined and modified from Thorne et al., 1999; Dunster et al., 2000, 2013). Stars in the map represent zebra rock occurrences (Loughnan and Roberts, 1990; Retallack, 2021).

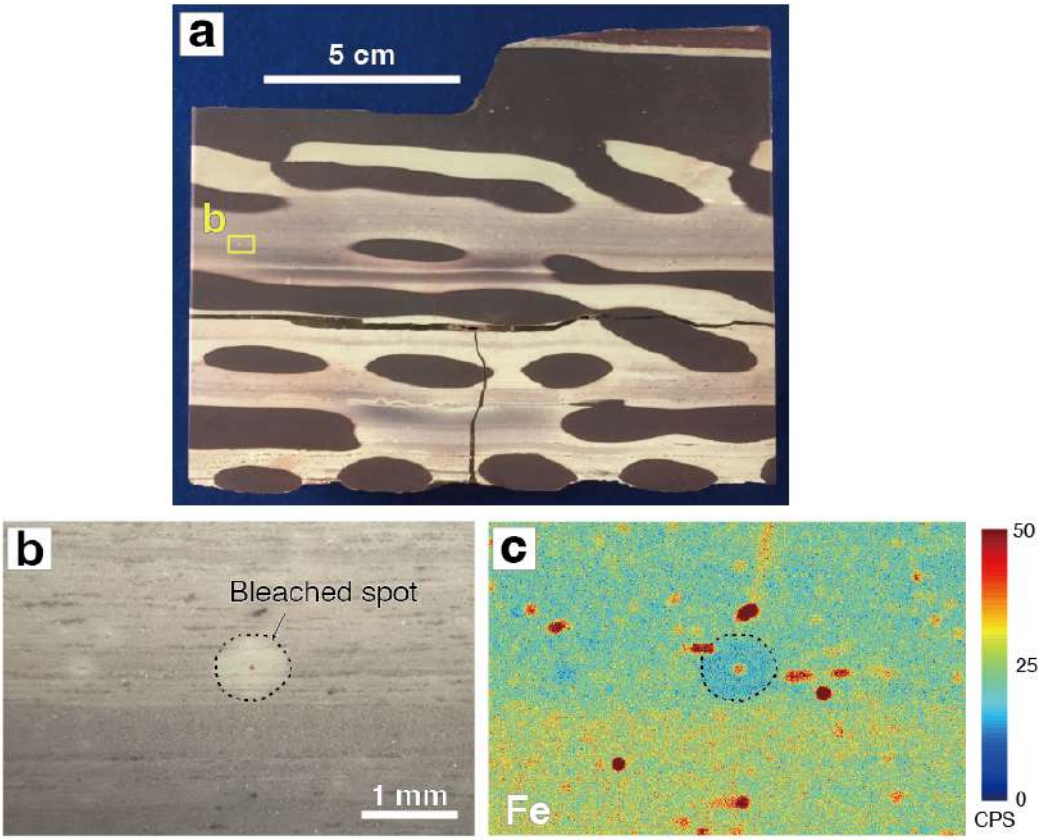

Fig. 3 The largest bleached spot in a zebra rock sample. **(a)** Cross-cut view of hand specimen of sample ZRY-05 and **(b)** Close-up of a bleached spot of ≈1 mm in diameter in (a), and **(c)** 2-D SXAM image of Fe distribution. The value of Fe is relatively higher at the center of the spot. Black dashed lines emphasize the outline of the bleached spot.

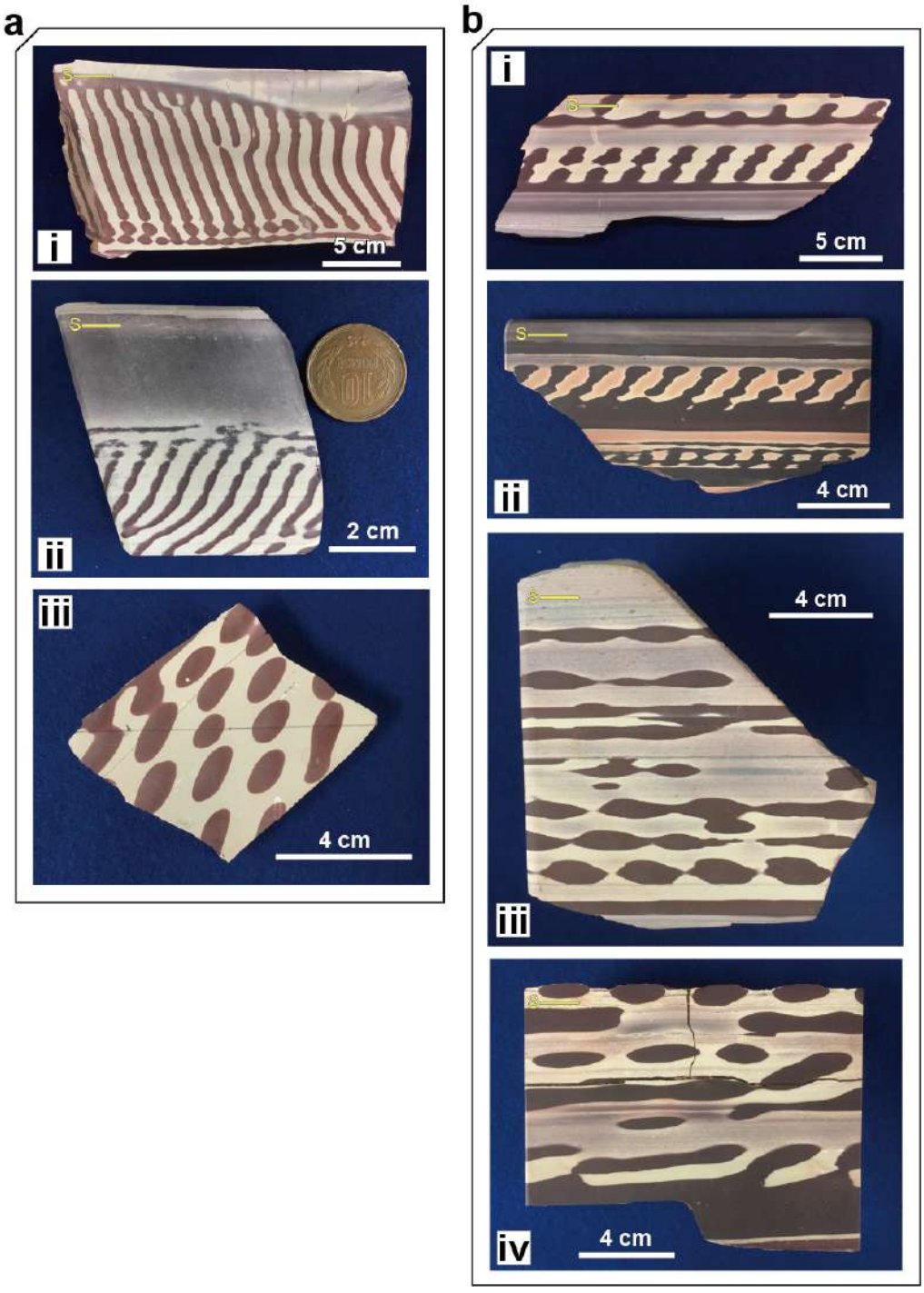

Fig. 4 Cross-cut views of two types of zebra rock samples in this study. **(a)** The kaolinite-dominant type zebra rock: (i) Sample No. ZRY-06, (ii) ZRY-10, (iii) ZRY-02. **(b)** The alunite-dominant type zebra rock: (iv) ZRY-07, (v) ZRY-03, (vi) ZRY-04, and (vii) ZRY-05.

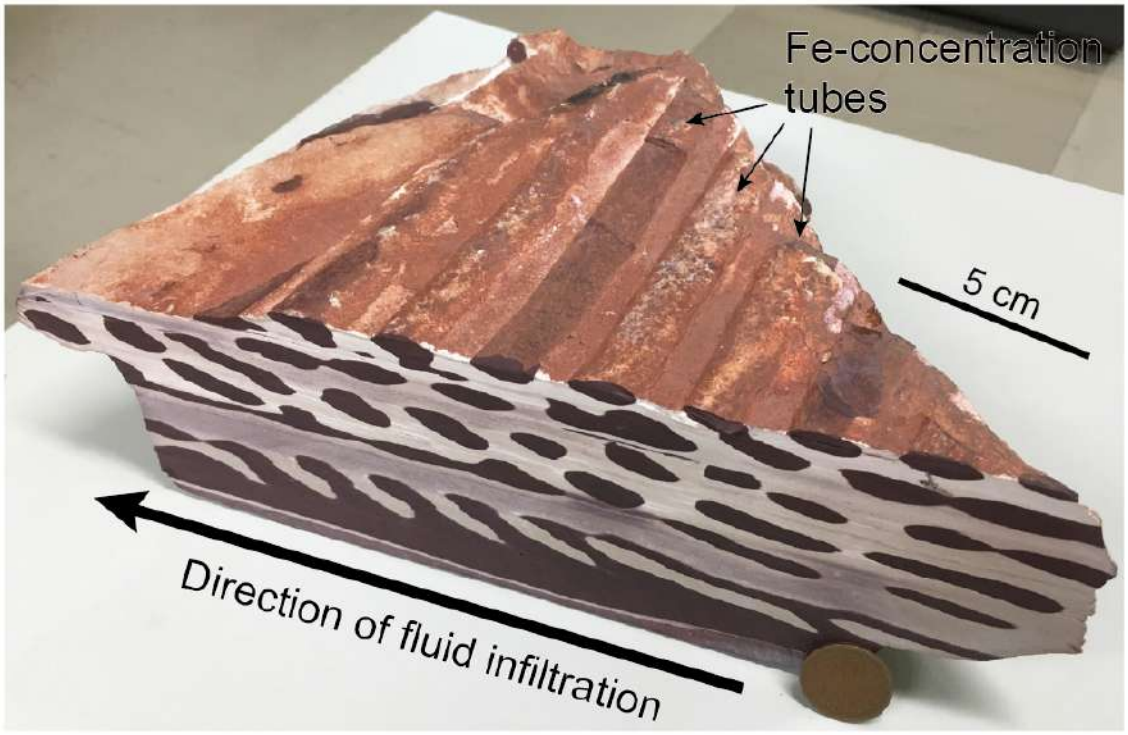

Fig. 5 3-D view of a zebra rock sample. The sample is located in Nagoya University Museum.

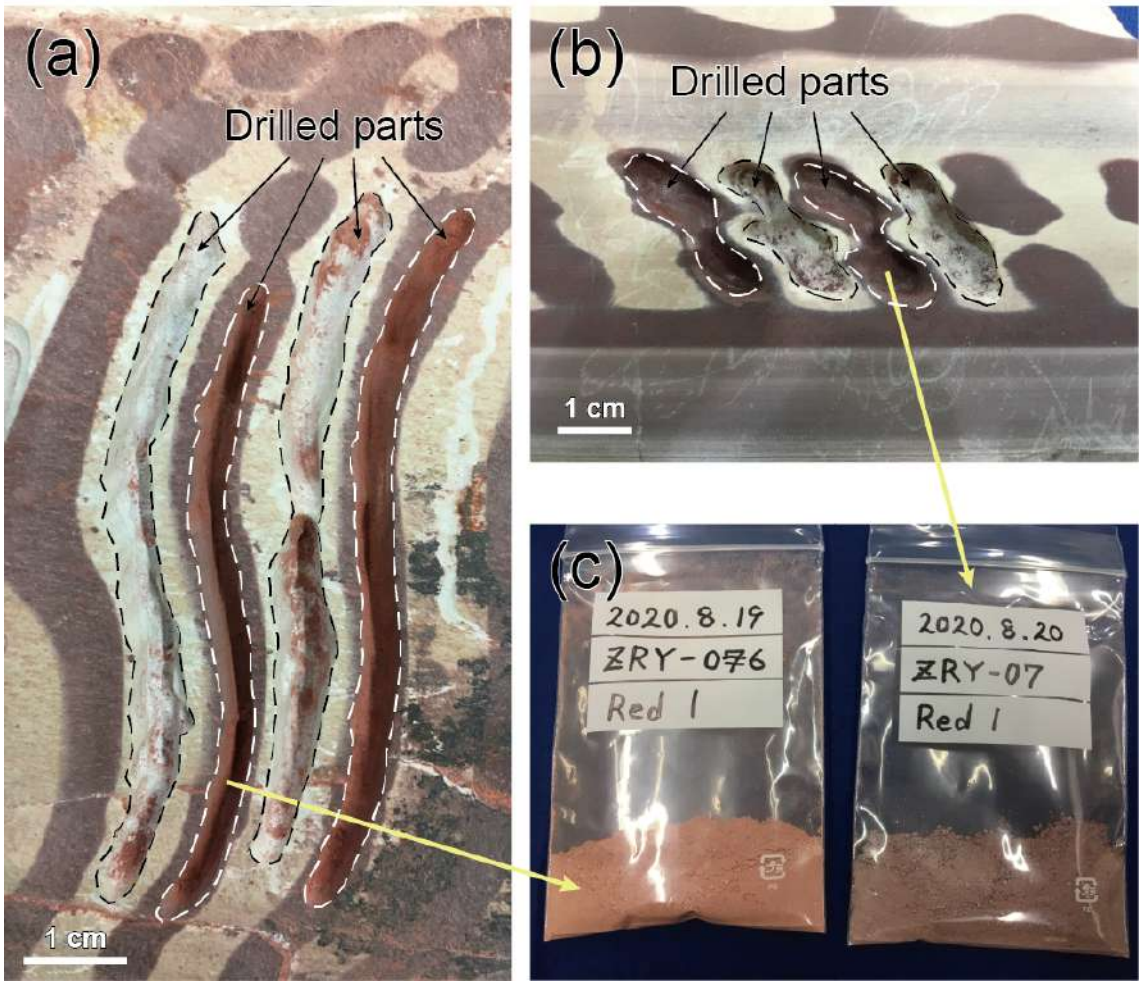

Fig. 6 Drilled parts of zebra rock samples. **(a)** Drilled parts of the Kao-type zebra rock and **(b)** the Alu-type zebra rock. The powdered samples for the chemical analysis were taken from two Fe oxide band parts and two white background parts of the two types of zebra rock, respectively. **(c)** Powdered samples of Fe oxide bands of the two types of zebra rock. The powder's color of the Alu-type zebra rock is much darker than the one of the Kao-type zebra rock.

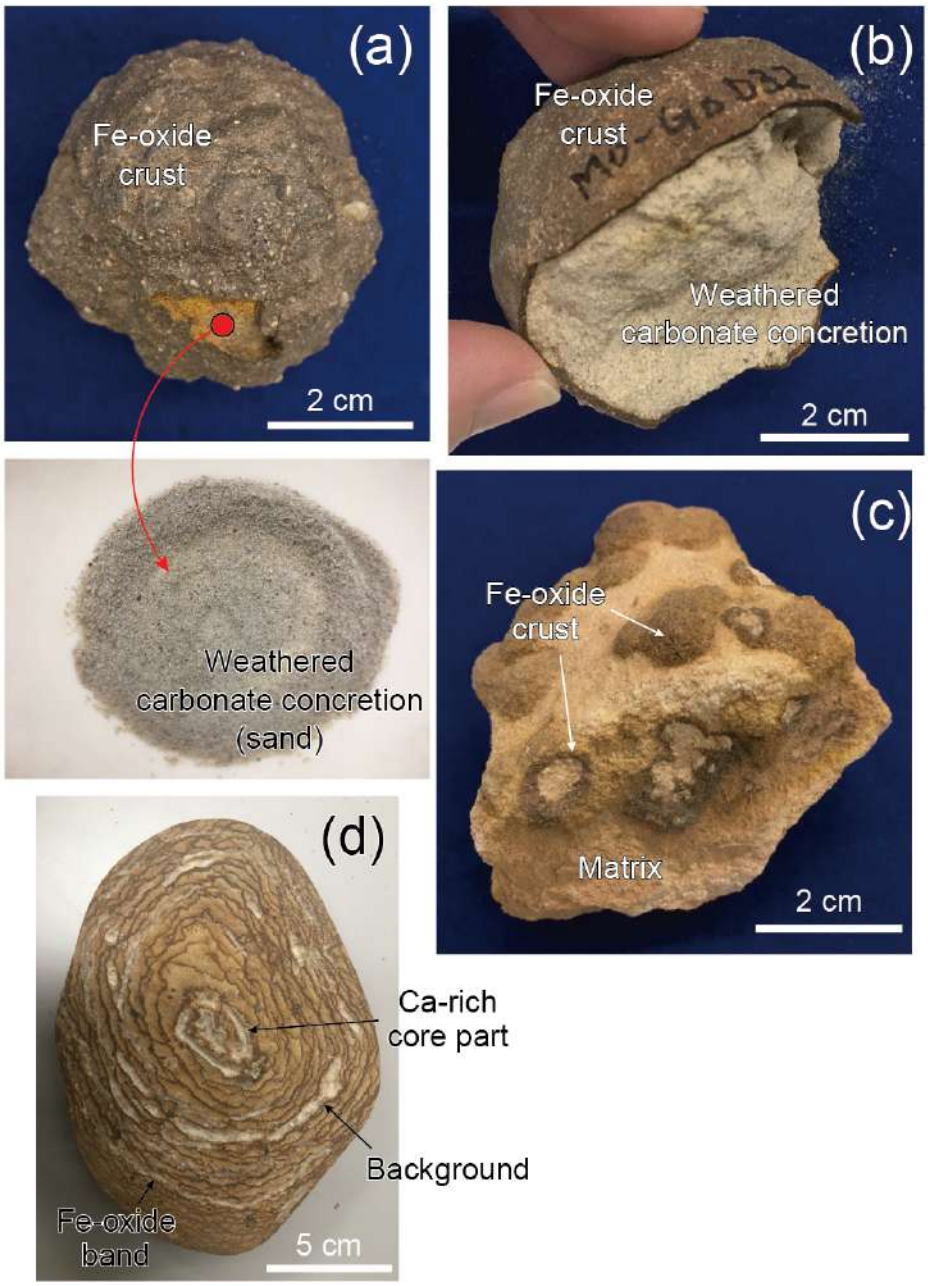

Fig. 7 Sample images of Fe oxide concretions and dacite cobble with Fe oxide bands for the chemical analysis. **(a)** and **(b)** Fe oxide concretions from Mongolia. Sample No. Mo-Go-030 and Mo-Go-032, respectively. A core part was strongly weathered carbonate concretion and was collected from a drilled hole. **(c)** Fe concretion from Jordan. Sample No. Jo-005. Fe oxide concretions are included in the host rock. **(d)** Dacite cobble with Fe oxide bands. Sample No. NGY-01. Powdered samples were collected from the Fe oxide band, Ca-rich core part, and background (the area between the bands at the outer part) by using microdrill.

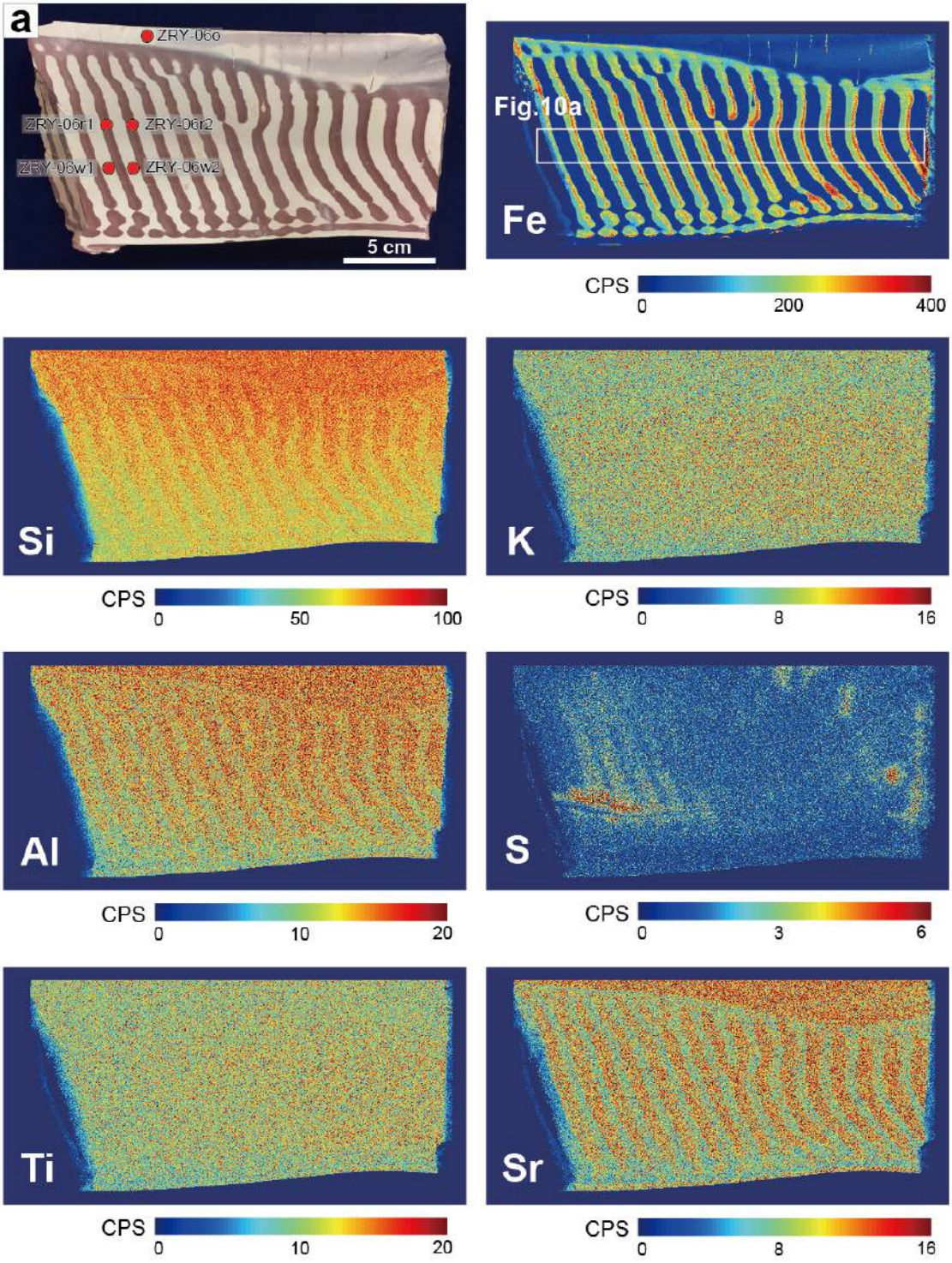
a
ZRY-06o
ZRY-06r1
ZRY-06r2
ZRY-06w1
ZRY-06w2
5 cm
Fig.10a
Fe
CPS
0
200
400
Si
CPS
0
50
100
K
CPS
0
8
16
Al
CPS
0
10
20
S
CPS
0
3
6
Ti
CPS
0
10
20
Sr
CPS
0
8
16

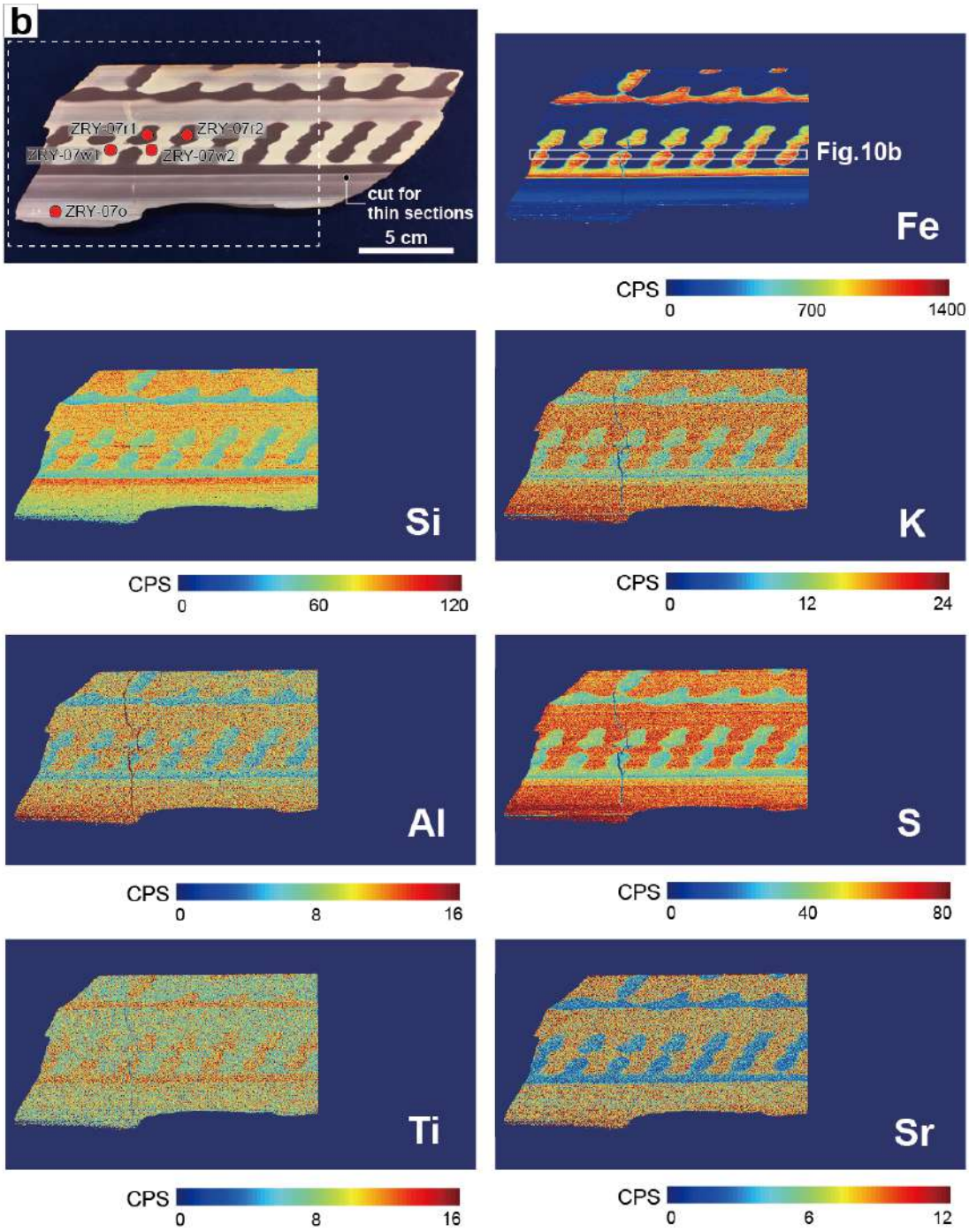

Fig. 8 Elemental mapping of two types of zebra rock. SXAM images of the distribution of Fe, Si, K, Al, S, Ti, Sr in ZRY-06 **(a)** and ZRY-07 **(b)**, respectively. (CPS, count per second).

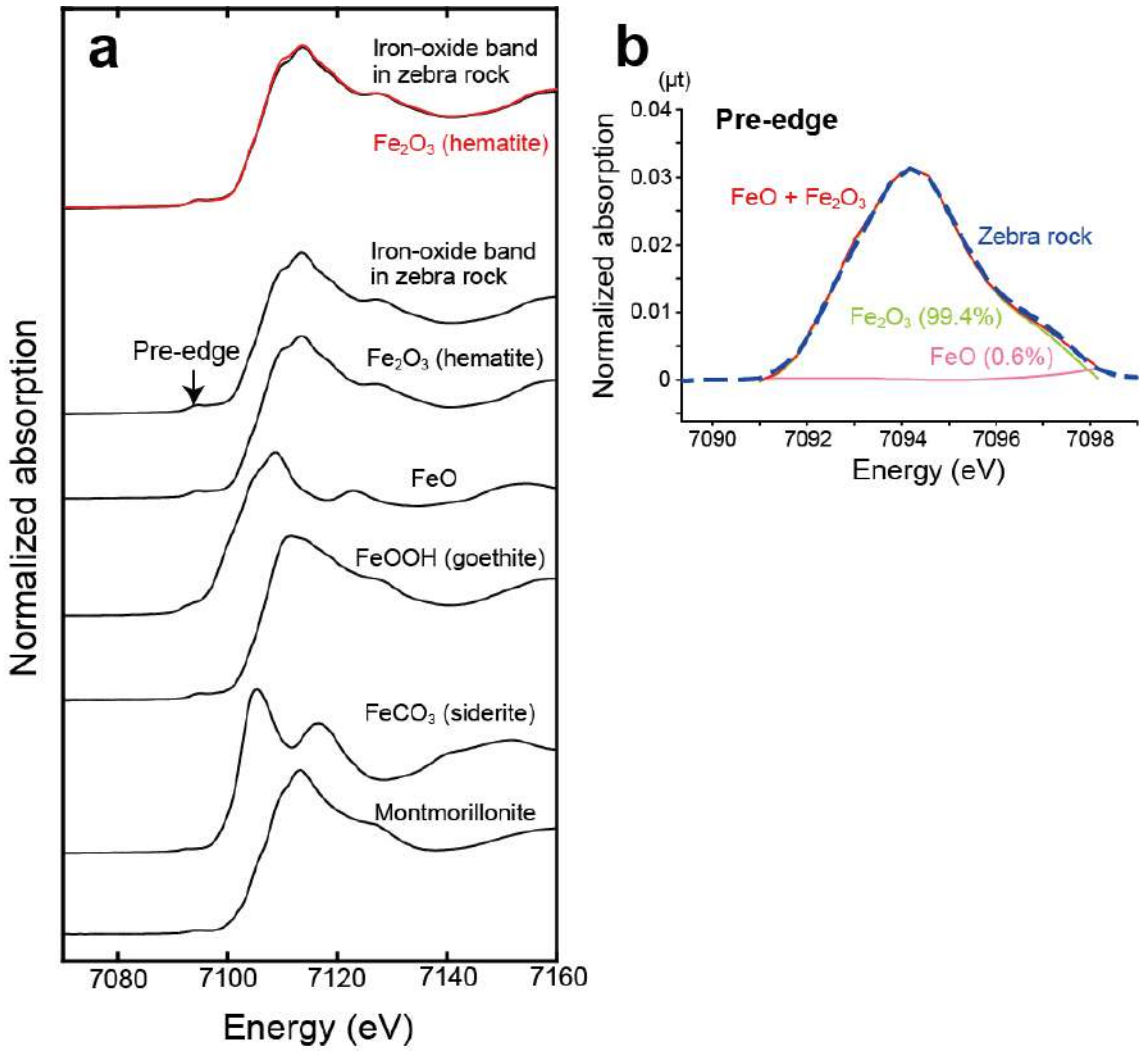

Fig. 9 Results of XANES for Fe oxide mineral in reddish bands in zebra rock. **(a)** Spectra of Fe K-edge XANES for a reddish band in zebra rock and reference samples of Fe oxide mineral. **(b)** The iron oxidation state of zebra rock investigated from the detail of Fe K-edge XANES spectra in the pre-edge part. Blue dotted line represents the spectrum of zebra rock.

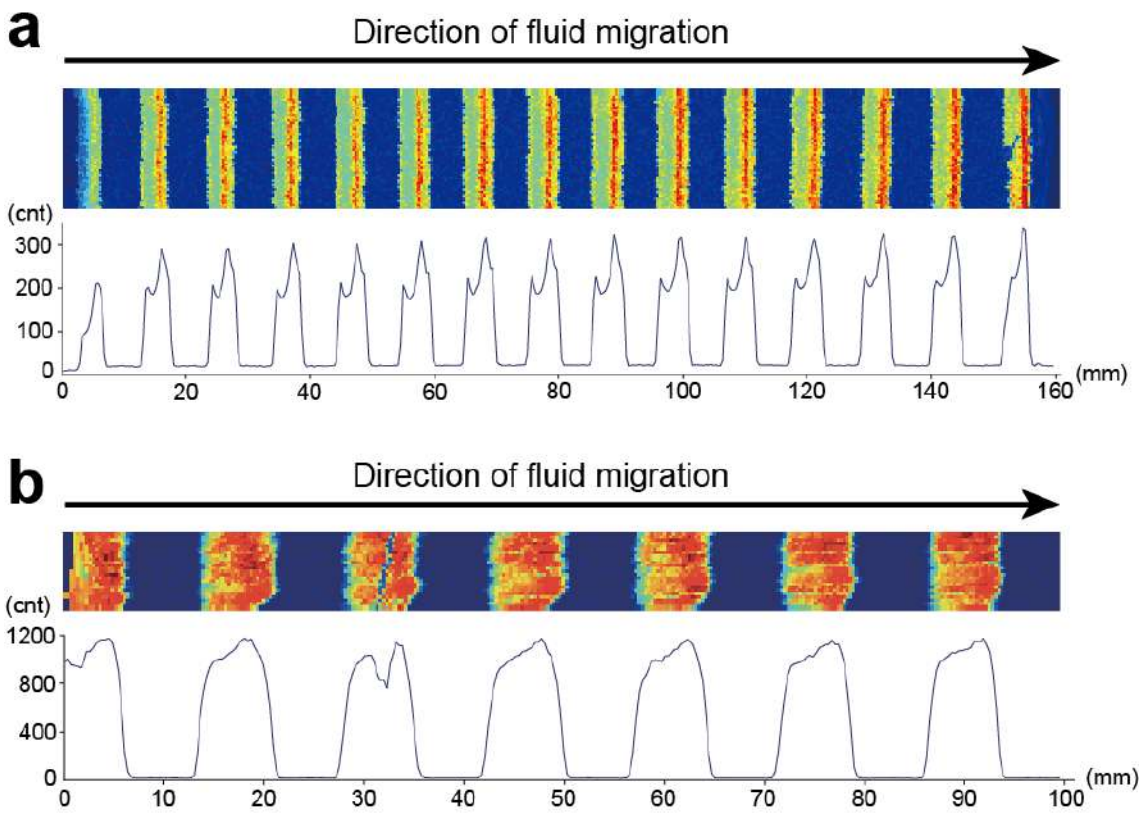

Fig. 10 SXAM profile of Fe oxide bands in zebra rock. Processed 2-D SXAM image (upper) and 1-D SXAM profiles (lower) from Fe oxide bands in ZRY-06 **(a)** and ZRY-07 **(b)**, respectively. Fe peaks correspond to Fe oxide band parts, and the asymmetrical Fe distribution represents the direction of fluid migration.

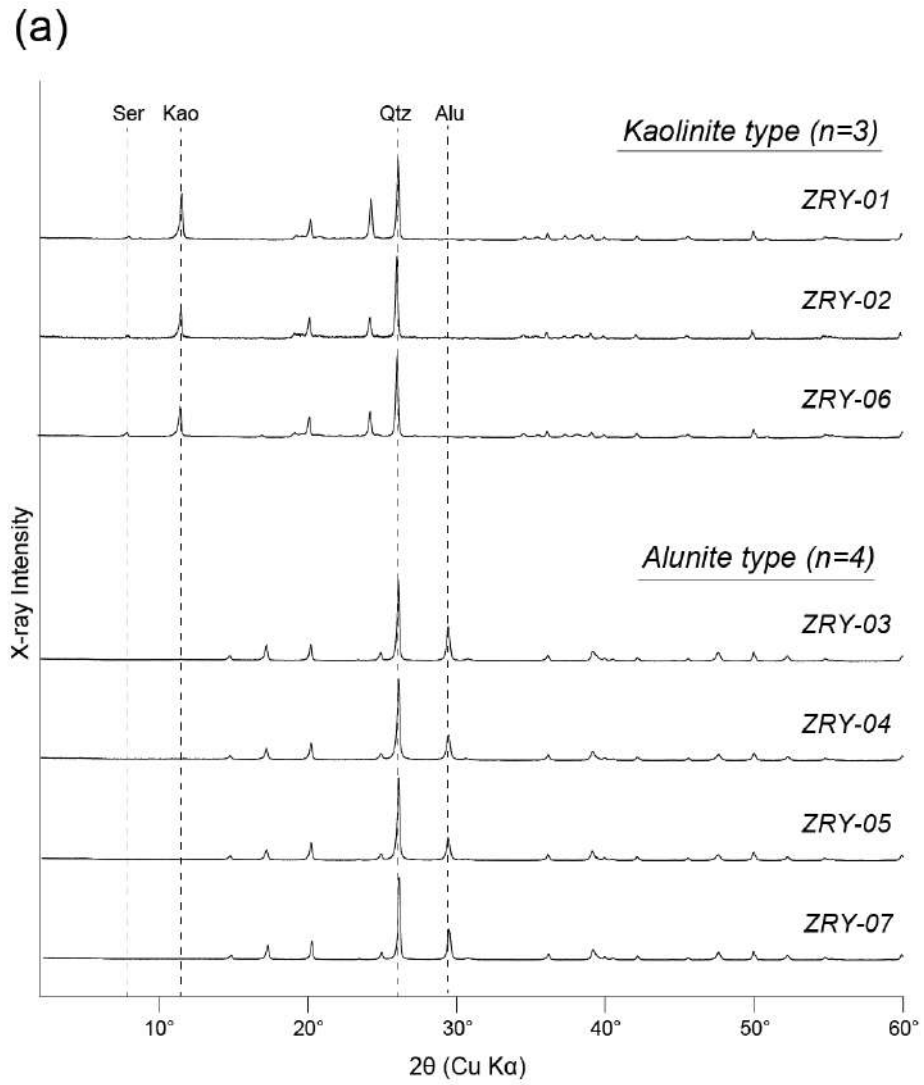

Fig. 11 Results of XRD analyses for zebra rock samples. **(a)** All of the zebra rock samples used in this study. They can be clearly divided into two types by the clay mineral assemblages. (continued)

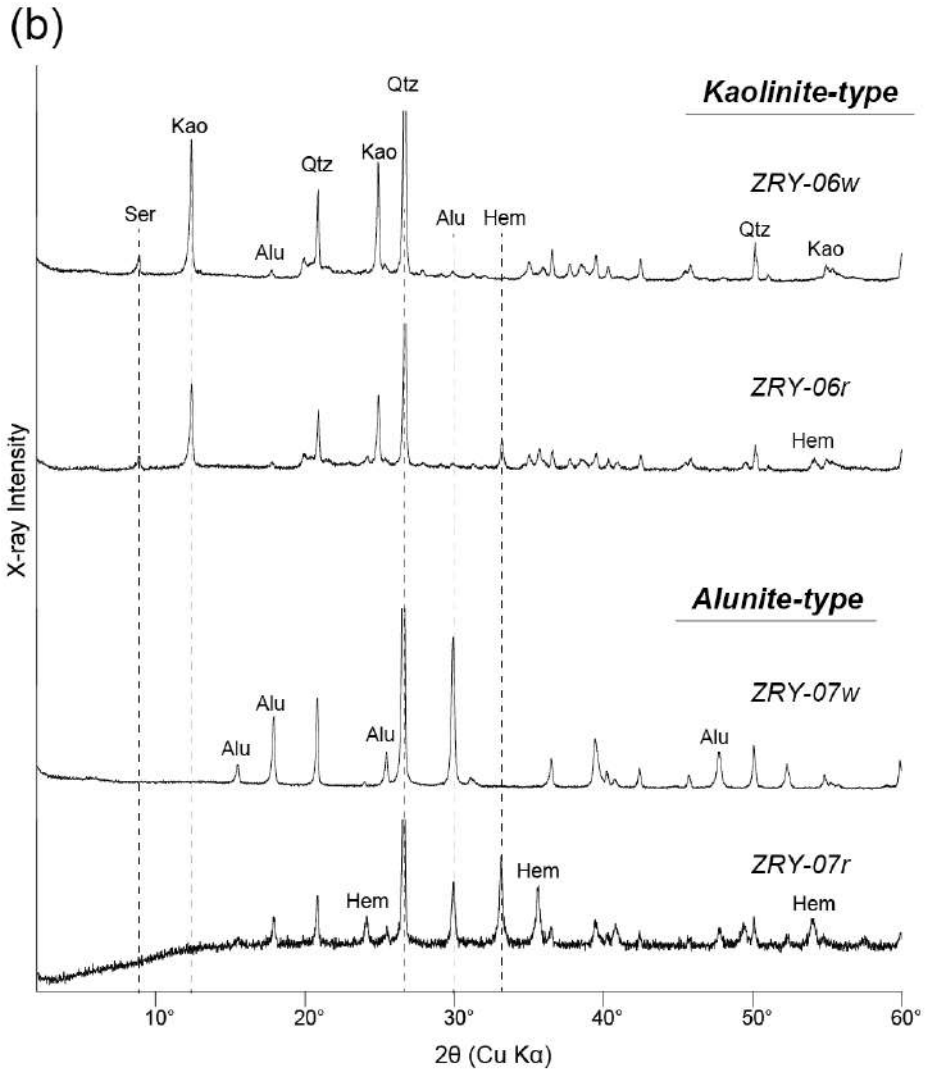

(b) Detail results of representative samples of two types of zebra rock: the Kao-type zebra rock (ZRY-06; upper) and the Alu-type zebra rock (ZRY-07; lower). “r” and “w” after sample numbers represent the reddish Fe oxide band and white background, respectively. Alu, alunite; Hem, hematite; Kao, kaolinite; Qtz, quartz; Ser, sericite.

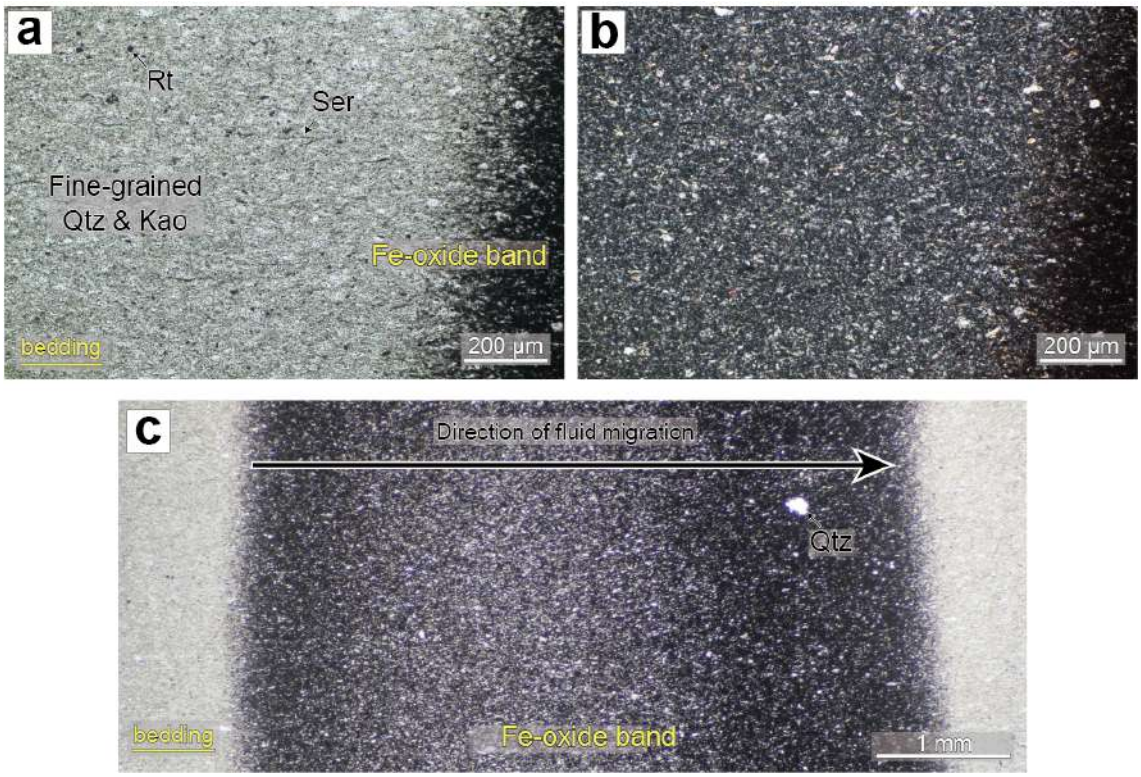

Fig. 12 Microscopic observations of the Kao-type zebra rock. **(a)** Photomicrograph of common texture of the Kao-type zebra rock (ZRY-06). Clay minerals are arranged along the bedding plane. Hematite fills the pores around quartz and clay minerals in the Fe oxide band. Plane polarized light. **(b)** Photograph of (a) in cross polarized light. **(c)** Photomicrograph of the overall width of Fe oxide band oblique to the bedding plane at a high angle, showing that hematite is not uniformly distributed (ZRY-06). The side with a higher concentration of Fe oxide minerals in the band is downstream of the fluid migration. Plane polarized light. Qtz, quartz; Rt, rutile; Ser, sericite.

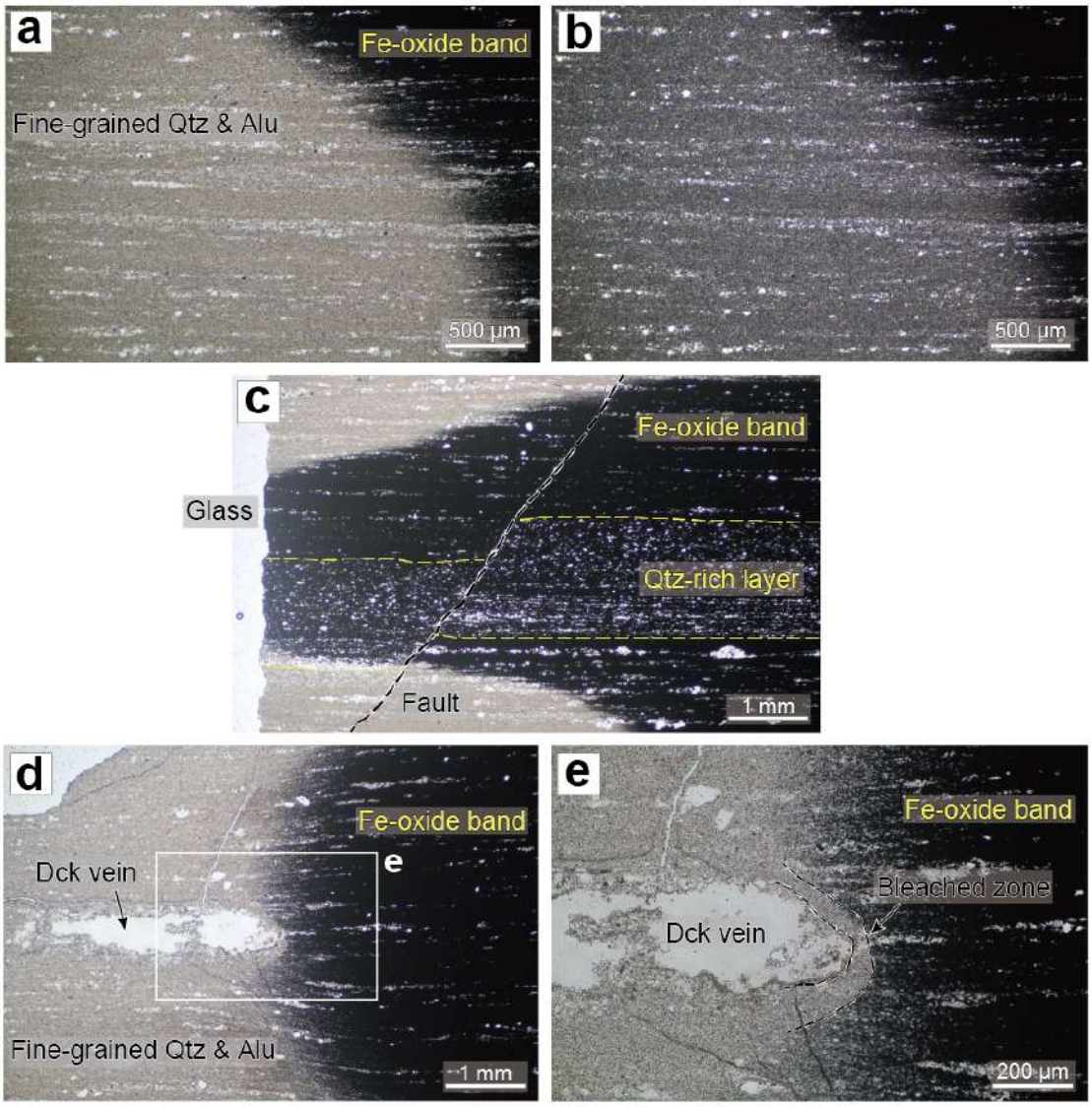

Fig. 13 Microscopic observations of the Alu-type zebra rock. **(a)** Photomicrograph of common texture of the Alu-type zebra rock (ZRY-05). The texture is dense and shows clear lamination, and the Fe oxide band is a darker color as compared to the Kao-type zebra rock. Opaque minerals on the outside of the band are fine-grained ilmenite and rutile. Plane polarized light. **(b)** Photomicrograph of (a) in cross polarized light. **(c)** Photomicrograph of microfault cutting the ellipsoidal Fe oxide concentration part. Qtz-rich layer is cut by normal microfault, but there is no offset in the Fe oxide concentration part, indicating that the Fe precipitation occurred after the microfault was formed. Plane polarized light. **(d)** Photomicrograph of dickite vein (ZRY-05). The vein is parallel to the bedding plane and breaks at the margin of the Fe concentration part. Plane polarized light. **(e)** Close-up of (d). At the margin of the dickite vein, the Fe oxide band is partially

decomposed, forming a bleached area. Plane polarized light. (continued)

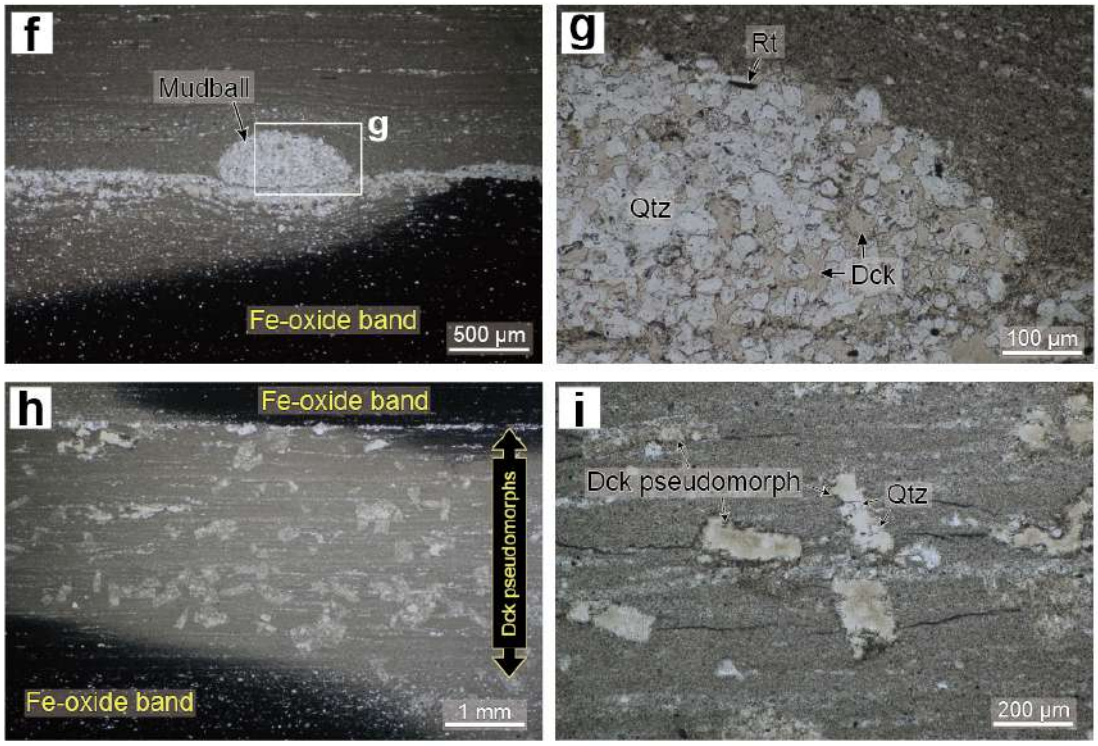

(f) Photomicrograph of mudball composed of relatively coarse-grained quartz, dickite, and rutile (ZRY-05). The flattened part is assumed to be the bottom (stratigraphically lower) part. The surrounding laminae are bent to fit the shape of a mudball. Plane polarized light. **(g)** Close-up of (d). Plane polarized light. **(h)** Photomicrograph showing dickite pseudomorphs after gypsum (ZRY-05). The pseudomorphs are distributed in a specific layer with a width of ≈3.5 mm wide. They are rectangular in shape, and their orientation of elongated axis is random. Plane polarized light. **(i)** Close-up of the dickite pseudomorphs (ZRY-05). The areas with lower refractive index in the pseudomorph comprise dickite. Plane polarized light. Alu, alunite; Dck, dickite; Qtz, quartz; Rt, rutile.

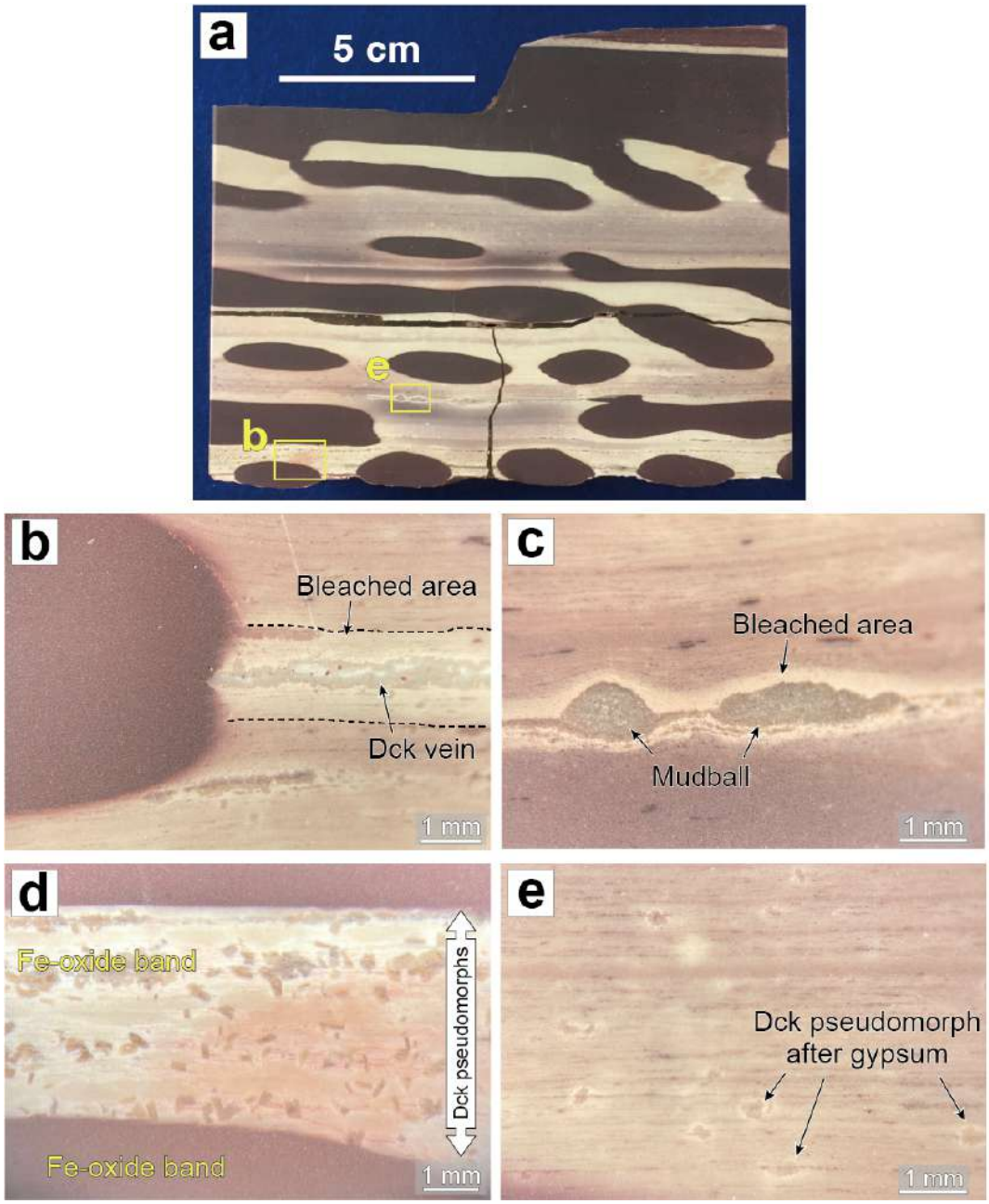

Fig. 14 Bleached textures in the Alu-type zebra rock. **(a)** Cross-cut view of the representative Alu-type zebra rock sample (ZRY-05). Lightly colored areas in the background show slight Fe concentration. **(b)** The dickite pseudomorph-rich layer in (a). The color of this layer is whiter than the other background part (i.e., bleached layer). **(c)** Sparce dickite pseudomorphs after gypsum (ZRY-05). The margin of the pseudomorphs shows tiny bleached area. **(d)** Dickite vein showing bleached halo (ZRY-05). **(e)** Mudballs composed of quartz and dickite in (a). The surrounding areas are bleached.

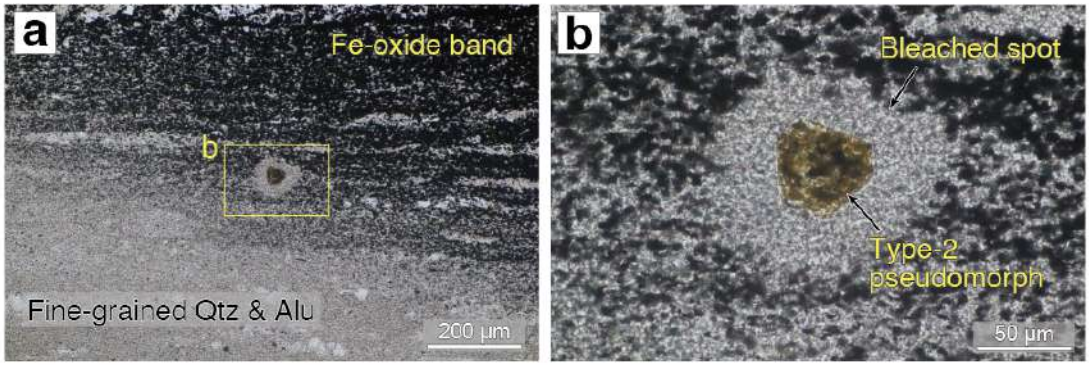

Fig. 15 Microscopic observations of the bleached spot in the Alu-type zebra rock. **(a)** Photomicrograph of a bleached spot at the margin of the Fe oxide band. The spot is observed only in the lower Fe concentration area. Plane polarized light. ZRY-07a. **(b)** Close-up of the bleached spot in (a). Six-sided pseudomorph located at the center of the spot primarily comprises dickite and Fe^{3+} minerals (type 2) and also contains opaque minerals such as Ti-oxide mineral. Plane polarized light. (continued)

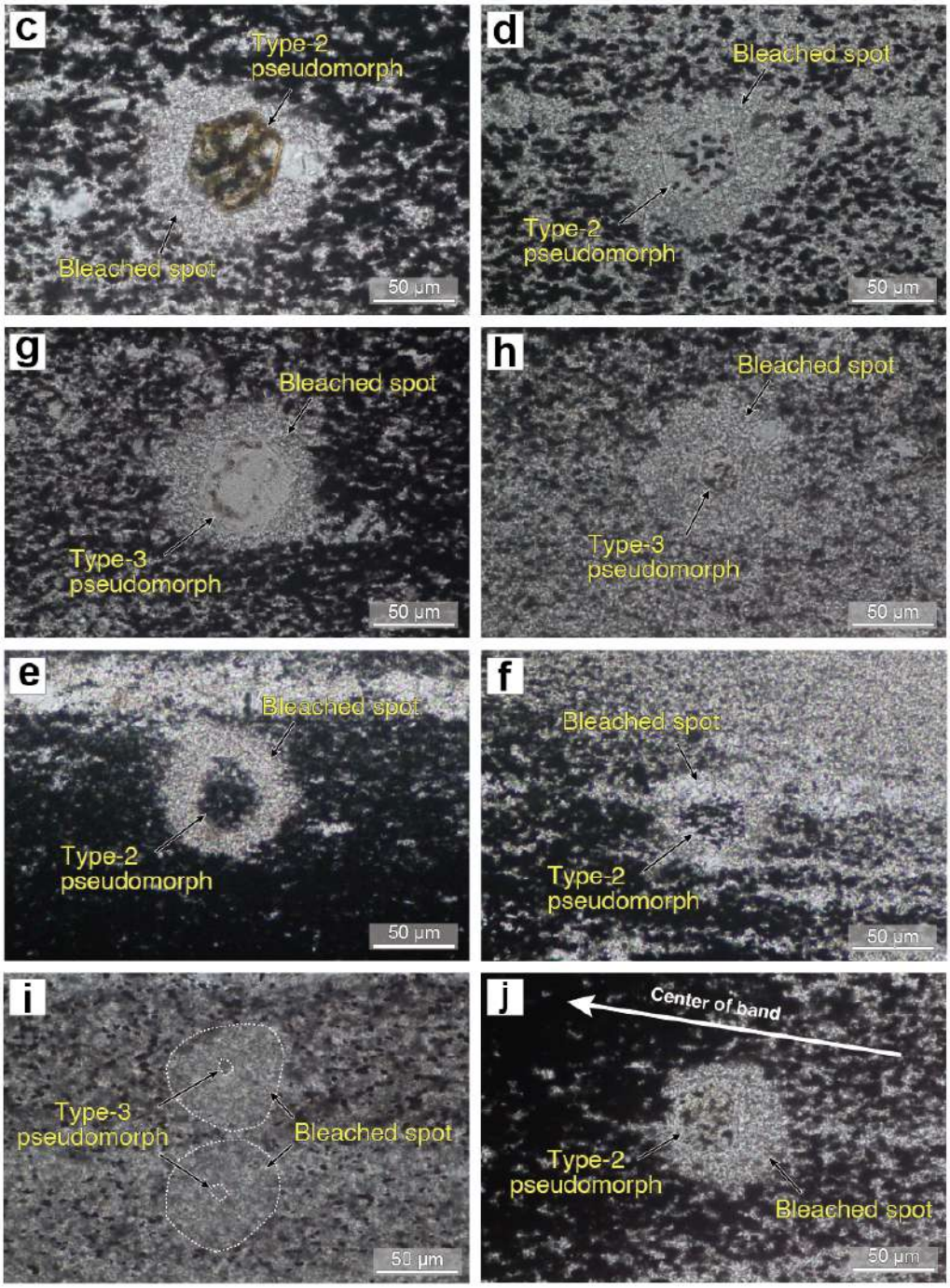

(c)–(j) Photomicrographs of bleached spots with polygonal dickite pseudomorph. ZRY-05a, 05f, 07a, and 07b. Plane polarized light. White dash lines in (i) represent the shapes of bleached spots and pseudomorph. In bleached spot in (j), the bleached area closer to the inner part of the band, where Fe concentrations are greater, is smaller than the one closer to the outer side of the band. (continued)

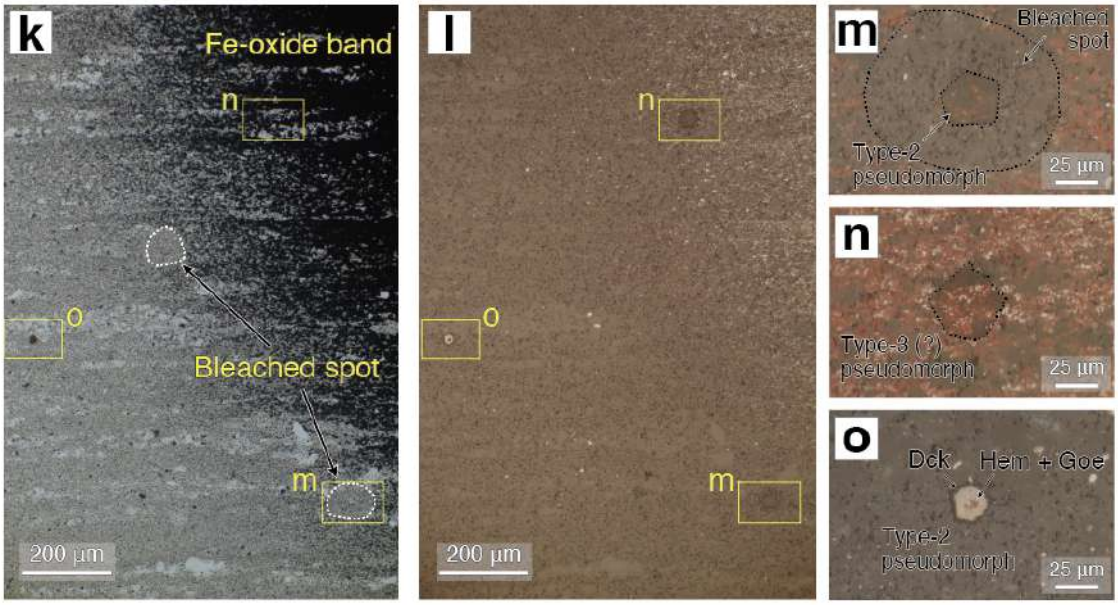

(k) and **(l)** Photomicrographs of the pseudomorphs under plane polarized light and reflected light, respectively. ZRY-07a. Three pseudomorphs can be observed inside and outside the Fe oxide band. Two bleached spots (white dashed lines) are discovered at the margin of the band. **(m)** and **(n)** Close-up of the pseudomorphs inside the band in (l). The pseudomorph in (m) at the margin (type 2) is contained in a bleached spot. Alternatively, the spot does not form around the pseudomorph located inside the band in (n); thus, it cannot be observed under plane polarized light in (k). The pseudomorph is unclear due to overprinting of Fe oxide minerals, but it is assumed to be type 3. Black dashed lines emphasize the outline of pseudomorphs and bleached spots. Reflected light. **(o)** Close-up of the pseudomorph outside the band in (l). It comprises Fe^{3+} minerals and dickite (type 2). Reflected light. Alu, alunite; Dck, dickite; Goe, goethite; Hem, hematite; Qtz, quartz.

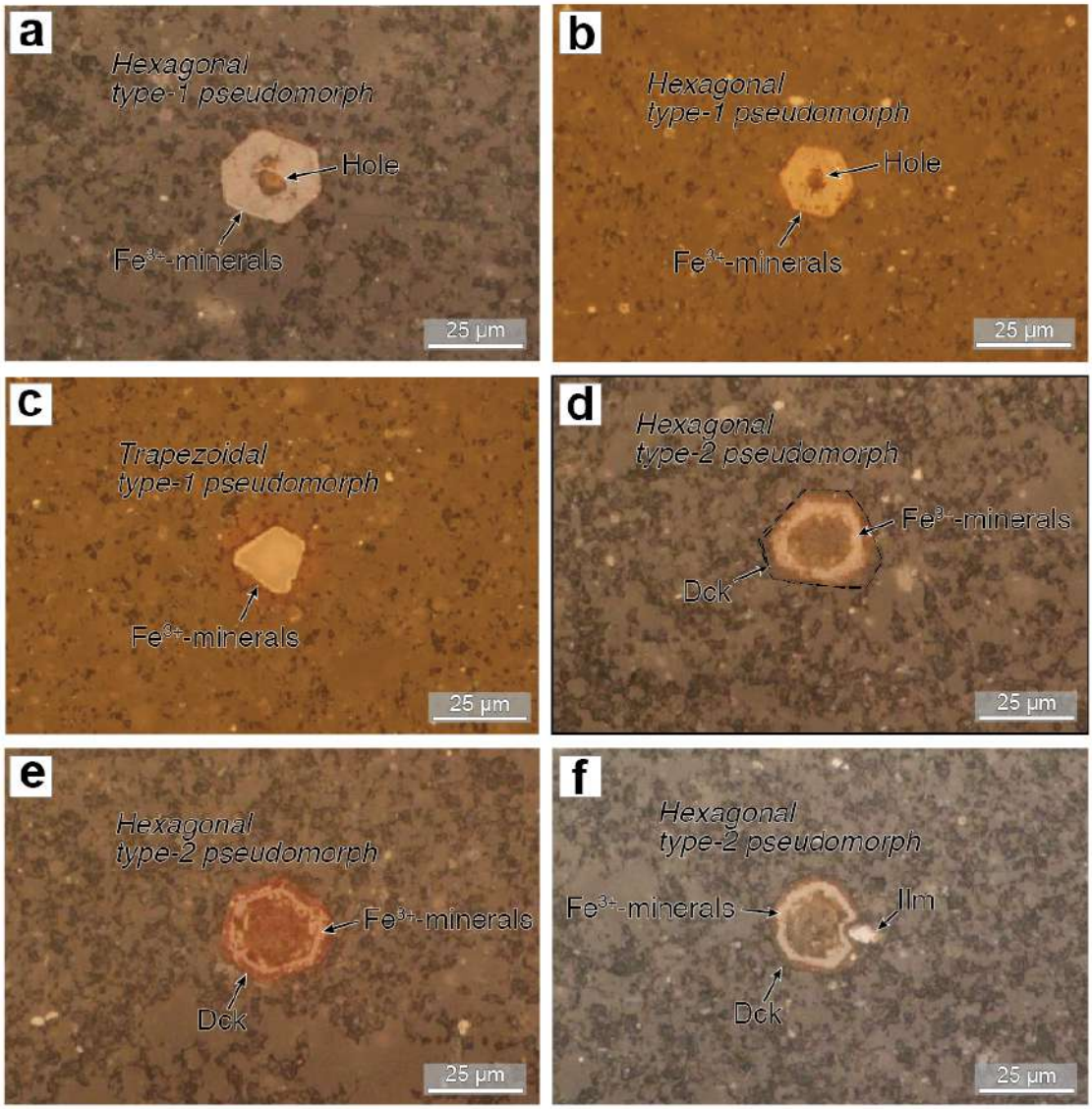

Fig. 16 Microscopic observations of polygonal pseudomorphs outside of the Fe oxide bands. Reflected light. The surrounding matrix is composed of quartz and alunite, with minor ilmenite. Black dash lines in (d) and (i) represent the margin of the pseudomorphs. **(a)–(c)** Photomicrographs of the type-1 pseudomorph. The pseudomorphs mostly comprise Fe^{3+}-minerals. The center part in (a) and (b) is slightly dissolved, and small amount of dickite appears. **(d)–(h)** Photomicrographs of the type-2 pseudomorph. Characteristic ring-shaped areas consisted of Fe^{3+}-minerals are observed inside the pseudomorphs. The center and rim part of the pseudomorph in (h) was starting to be dissolved, showing the transition texture from the type-1 to the type-2 pseudomorph. (continue)

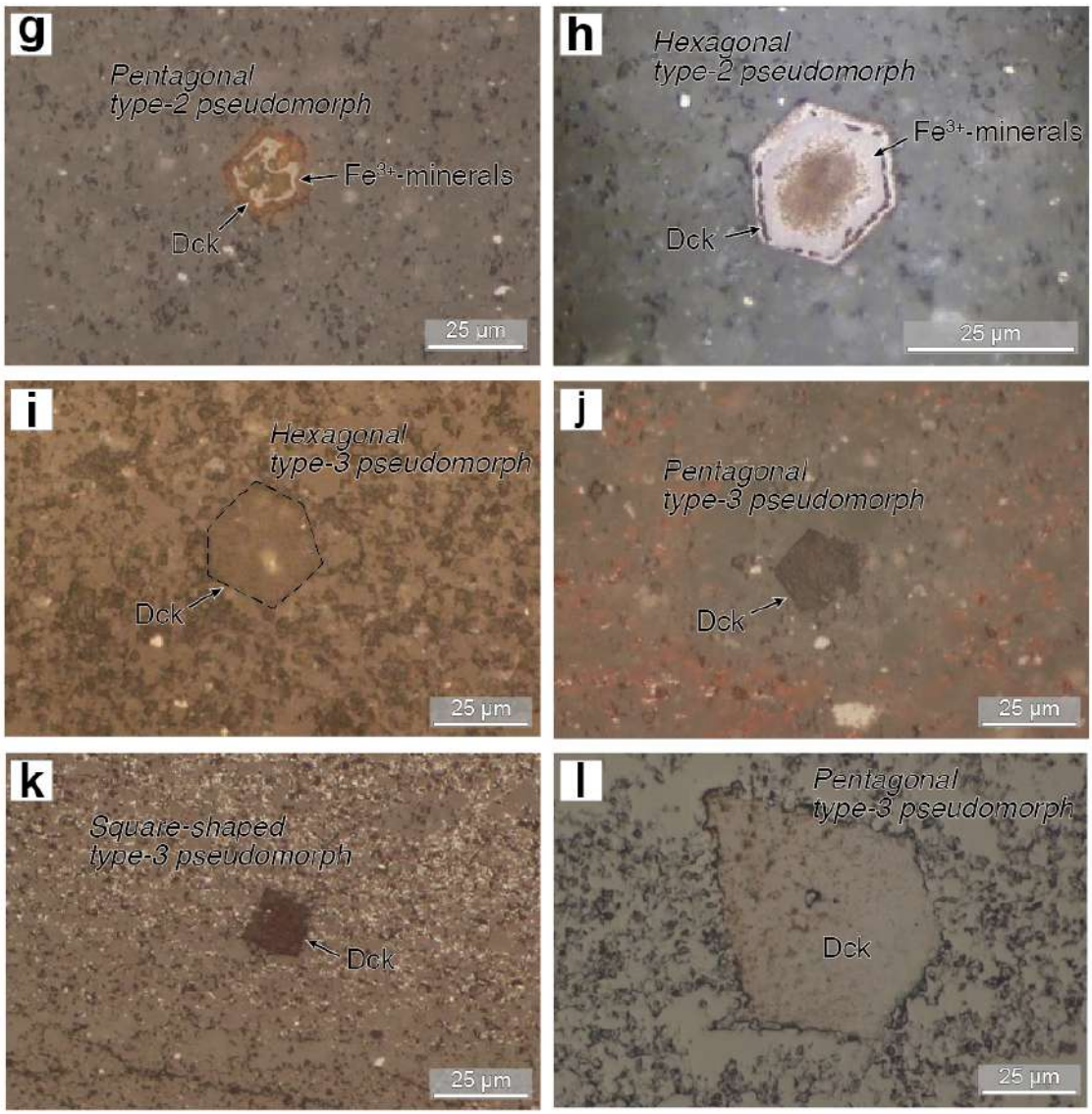

(i)–(l) Photomicrographs of the type-3 pseudomorph. They are almost replaced to dickite, and are vary in size.

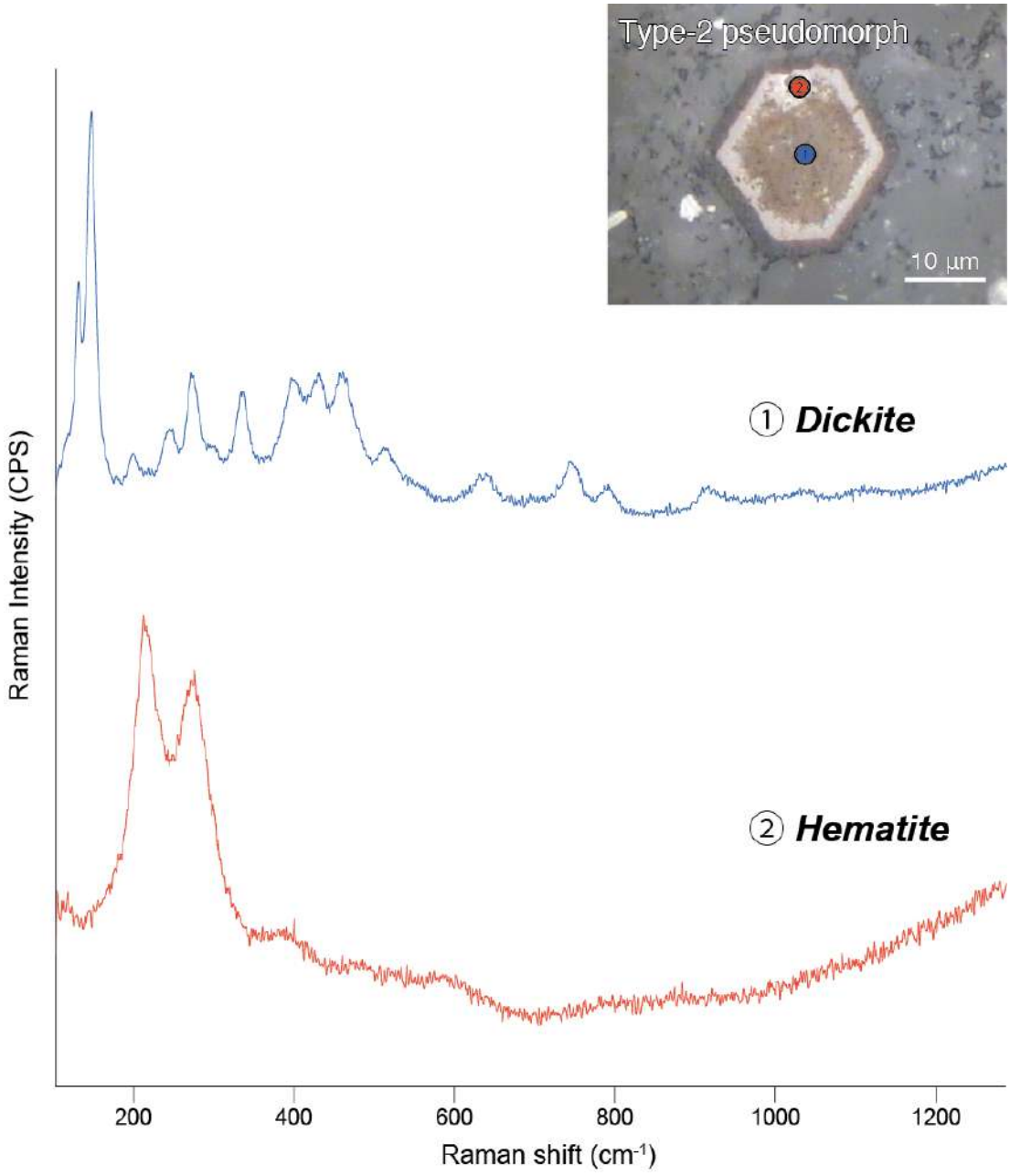

Fig. 17 Results of Raman spectroscopy for the type 2 pseudomorph in zebra rock (ZRY-07a). The spectrum at the center of the pseudomorph (①: blue line) represents dickite. The one of ring-shaped part (②: red line) represents hematite. The area of the rim part is too small to obtain the spectrum.

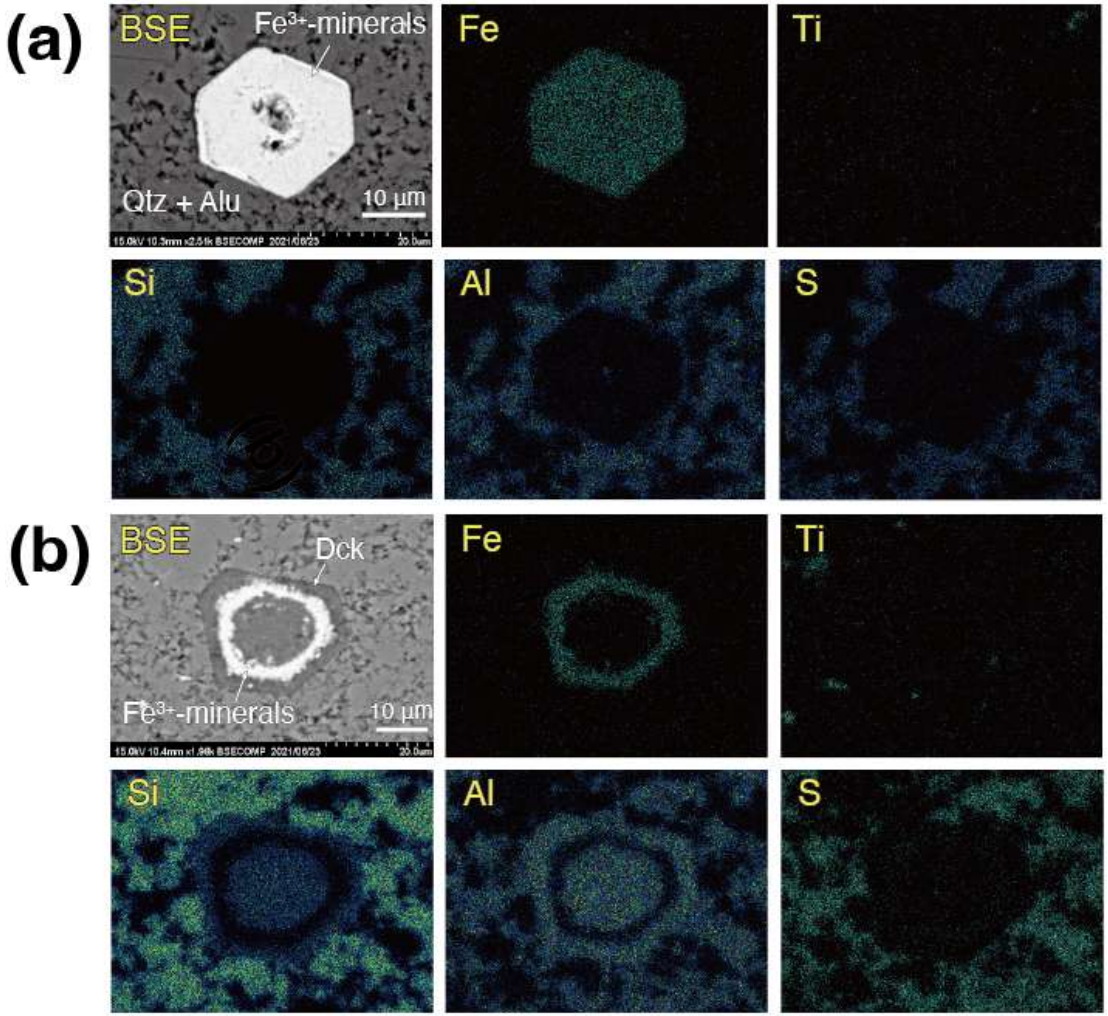
(a)
BSE
Fe3+-minerals
Qtz + Alu
10 µm
Fe
Ti
Si
Al
S
(b)
BSE
Dck
Fe3+-minerals
10 µm
Fe
Ti
Si
Al
S

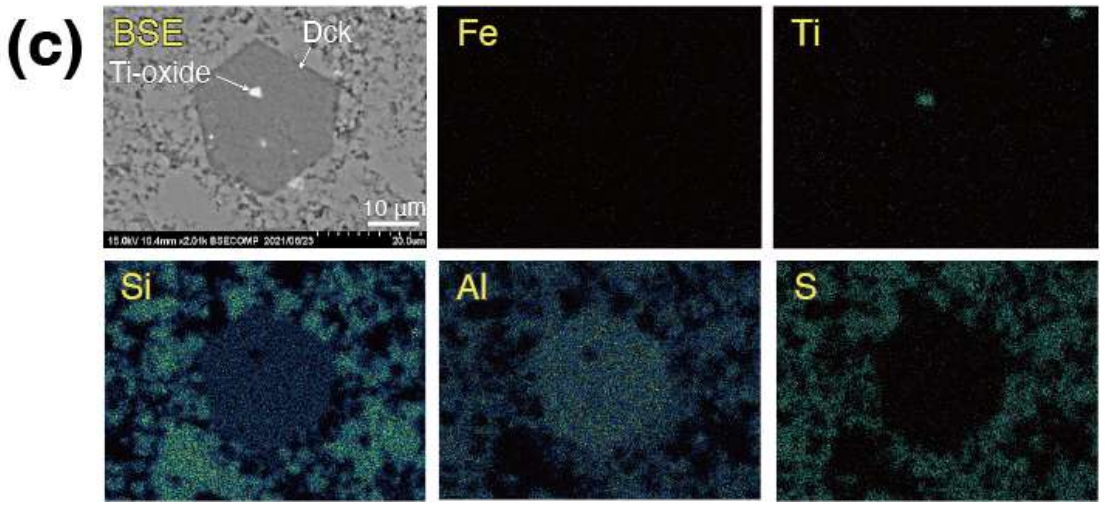

Fig. 18 SEM-EDX images of pseudomorphs in ZRY-07a; backscattered electron (BSE) images and elemental mappings of Fe, Ti, Si, Al, and S. Images of Si, Si-Al, and Al-S represent quartz, dickite, and alunite, respectively. (a) Type 1 pseudomorph comprises Fe^{3+} minerals. (b) Type 2 pseudomorph with ring-shaped Fe^{3+} minerals. (c) Type 3 pseudomorph comprises dickite. Alu, alunite; Dck, dickite; Goe, goethite; Hem, hematite; Qtz, quartz.

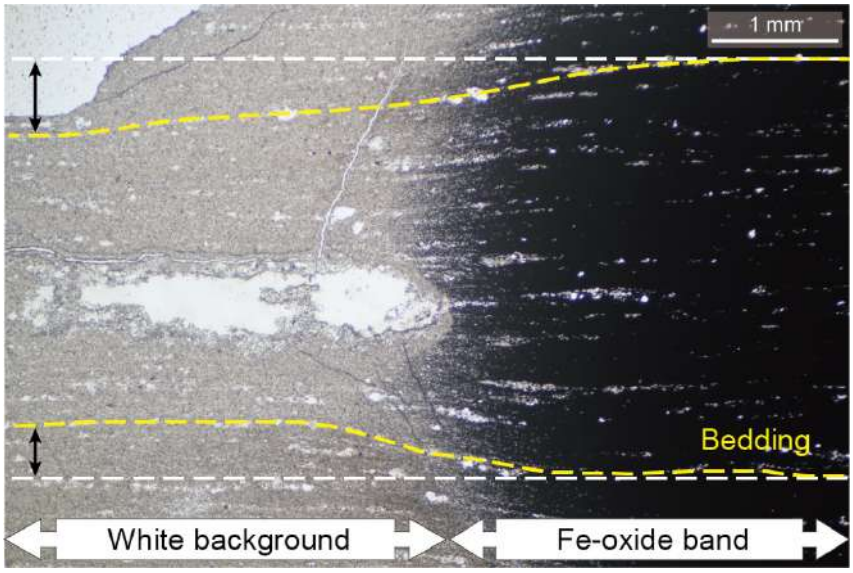

Fig. 19 Microscopic observation of compaction texture around Fe oxide band. Yellow dashed lines represent laminae. The laminae outside the band are bent, and their spacing is closer than the one inside the band. White dashed lines represent horizontal extension of the laminae inside the band.

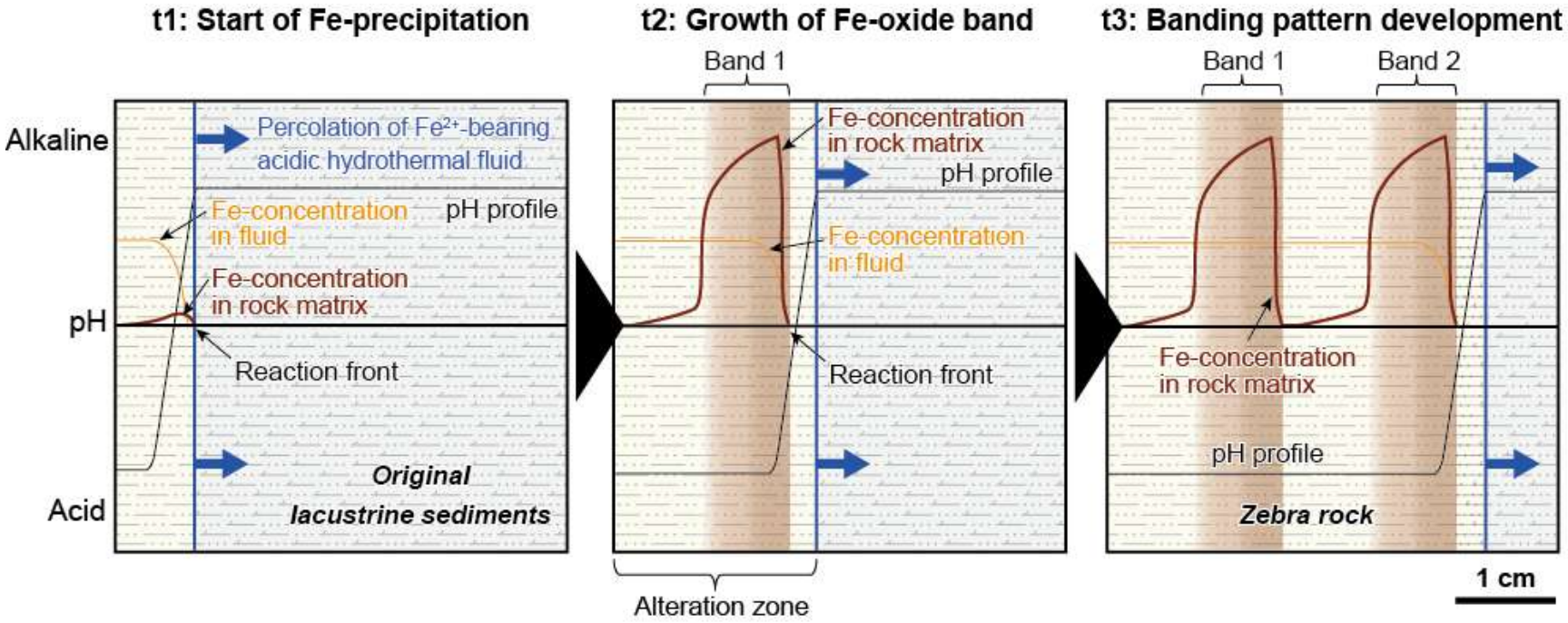

Fig. 20 A schematic model for Fe oxide banding formation.

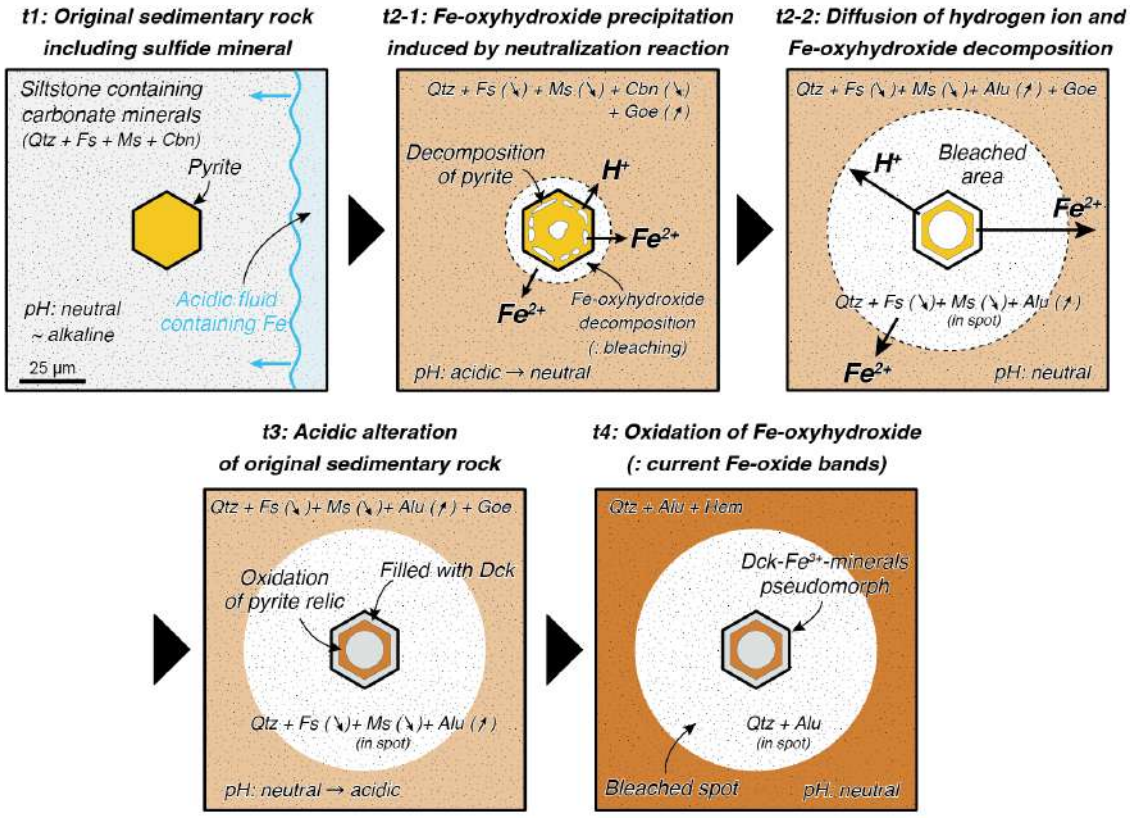

Fig. 21 Schematic of the bleached spot formation. Alu, alunite; Cbn, carbonate mineral; Dck, dickite; Fs, feldspar; Goe, goethite; Hem, hematite; Ms, muscovite; Qtz, quartz.

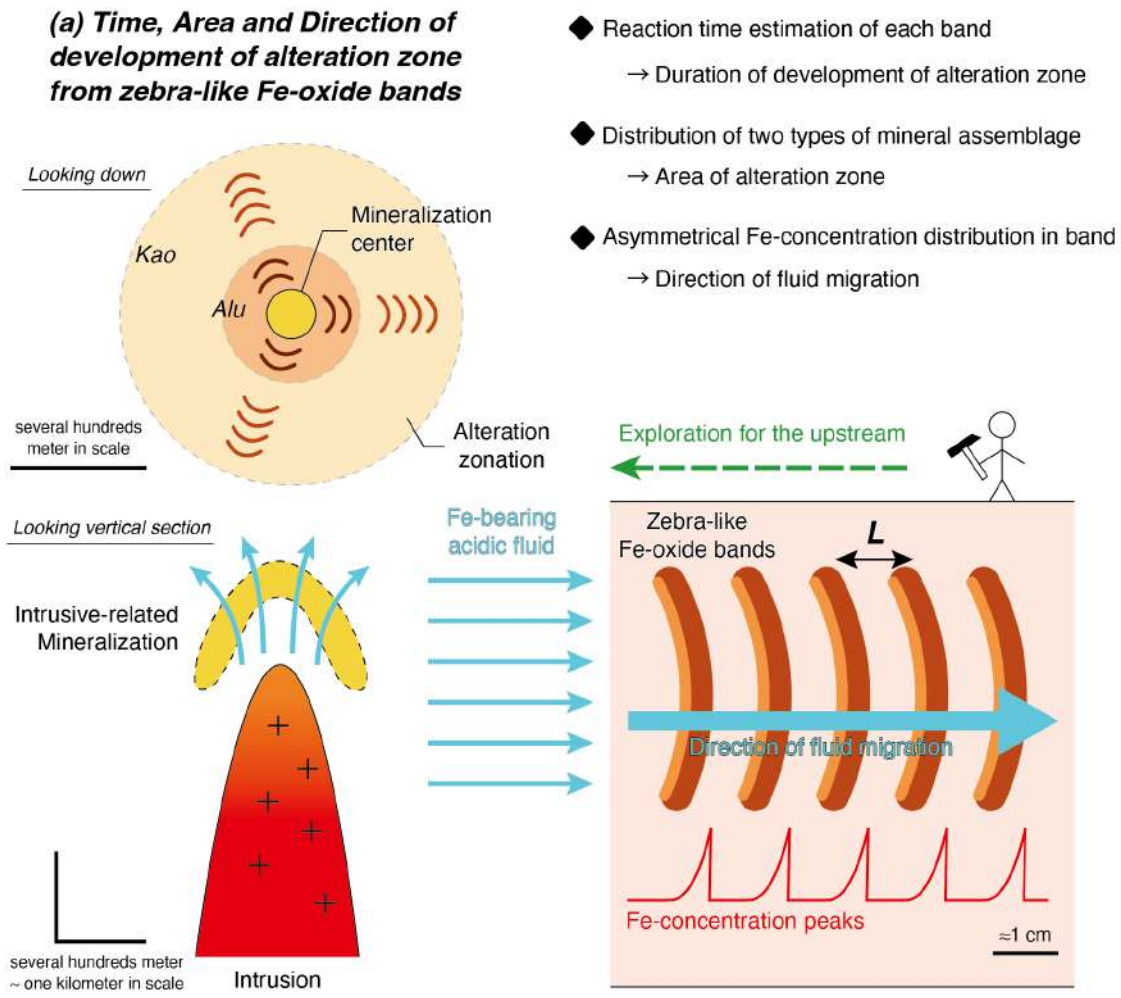

Fig. 22 Application of Fe oxide bands and bleached spots to explorations of metal mineral deposits and extraterrestrial life (a,b,c). (a) Time, area, and direction of development of alteration zone from zebra-like Fe oxide bands. Alu, alunite; Kao, kaolinite. "L" represents the space between bands. (b) Explorations of mineral deposits and extraterrestrial life on Mars. (c) Bleached spots as potential marker of mineral deposit related to red sandstone. Py, pyrite.

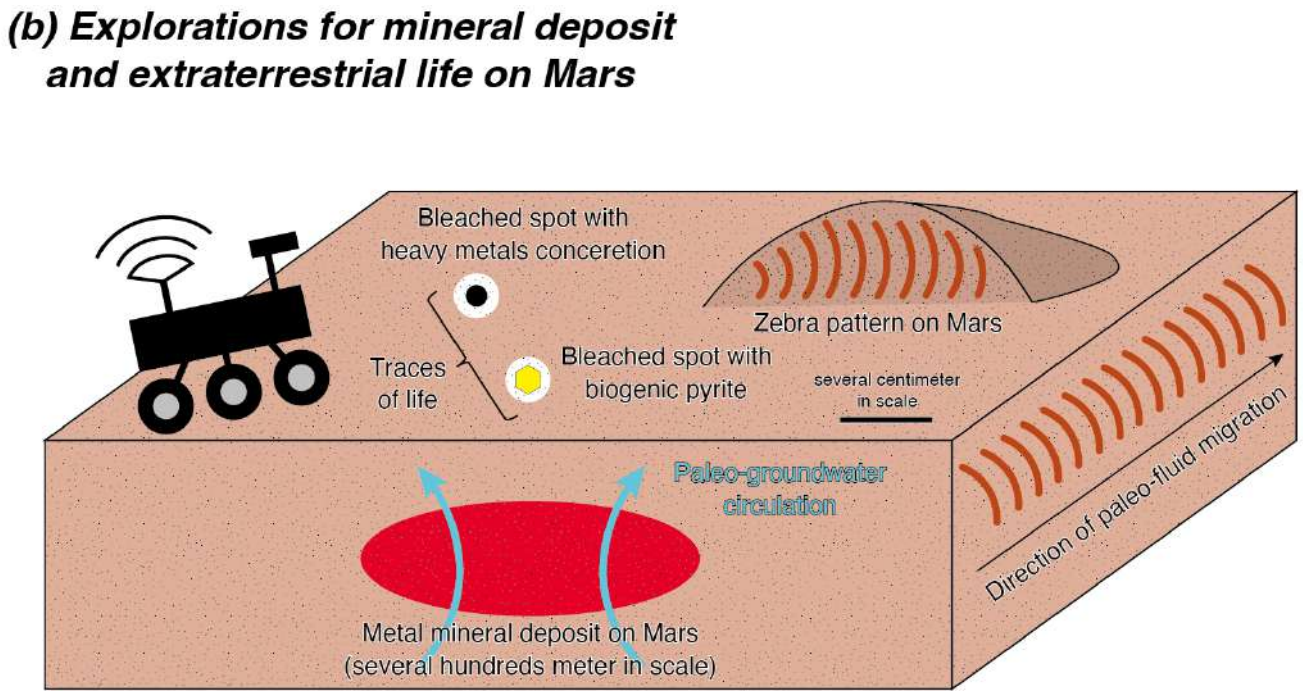

(b) Explorations of mineral deposits and extraterrestrial life on Mars.

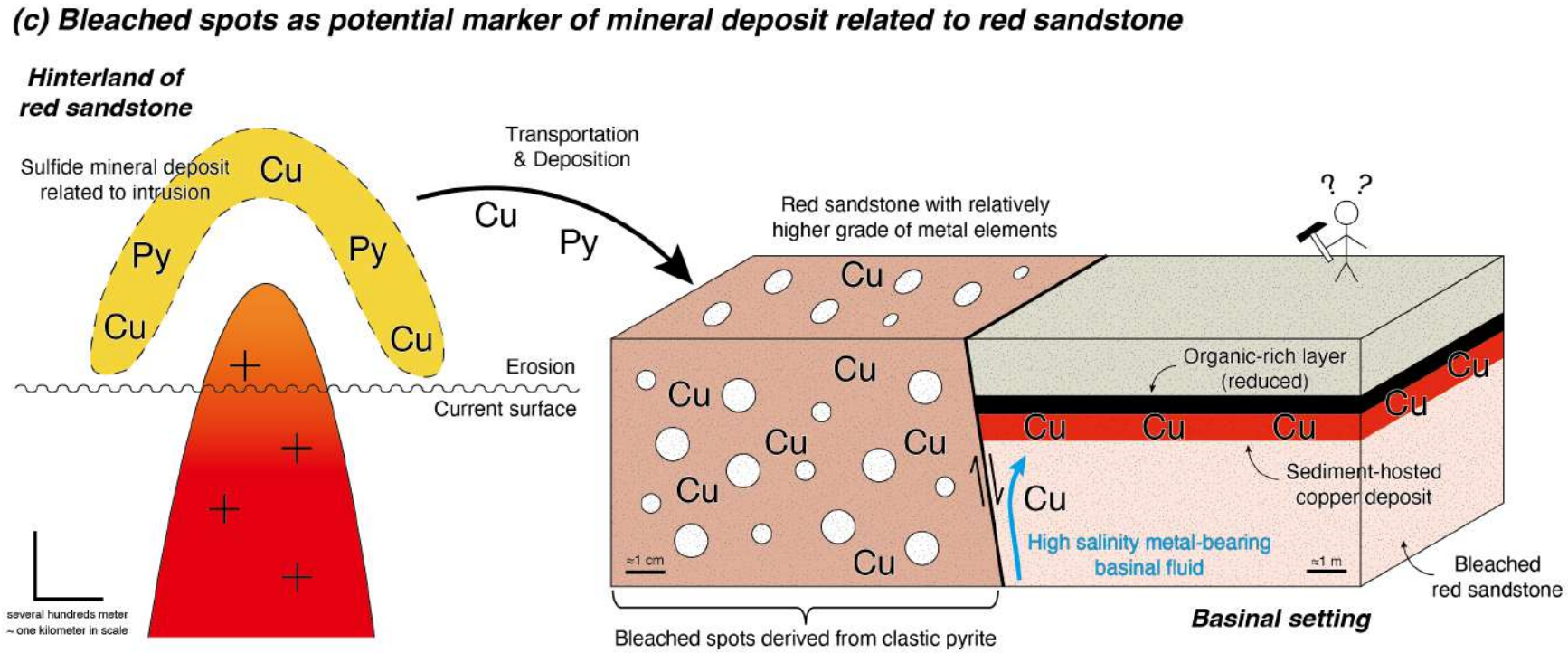

(c) Bleached spots as potential marker of mineral deposit related to red sandstone. Py, pyrite.

Table 1

Table 1 List of locations of bleached spot occurrence.

Country	Area	Stratigraphy	Age	Setting	Rock type	Reference
Antarctica	Southern Victoria Land	Aztec siltstone	Late Devonian	Fluvial	Siltstone	McPerson 1979
Argentina	Los Chihuidos High	the Huincul Formation, Neuque'n Group	Middle Cretaceous (late Cenomanian–early Turonian)	Fluvial deposits developed in a foreland basin	Sandstone with hydrocarbon-induced alteration in continental red-bed	Rainoldi et al., 2014
Australia	South Australia	the Pandurra Formation	Mesoproterozoic	the Intracratonic Cariewerloo Basin	Mudstones and siltstones	Cowley, 1993
Bulgaria	the Golo-bardo unit	the Komstica Formation, the Moesian Group	Late Triassic	Marine shallow-water deposits formed in most unstable paleogeographic setting of regressing sea and separation of local basins and environments.	Red shales, siltstones and sandstones	Budurov et al., 1993
China	Danxia Mountain, Guangdong	-	-	Continental	Red sandstone and conglomerate	He et al., 2022
Denmark	North Sea Basin	The Bunter Sandstone Formation,	Early Triassic	Fluvial, or a mixture of ephemeral streams and aeolian sand sheets in sabkha environment	Sandstone	Weibel, 1998; Weibel and Friis, 2004; Olivarius et al., 2015
Egypt	Southern Egypt	the Nubia Formation	Late Cretaceous (Coniacian-Santonian)	-	Sandstone	Hamimi et al., 2018
France	Brittany	the Pont-Réan formation	Ordovician	Small basins of half graben type	-	Cogne, 1988
	the Maritime Alps (southeastern France)	-	Permian	-	Red shales and slates	Kligfield et al., 1981, 1983
Greenland	Western South Greenland	the Eriksfjord Formation	Middle Proterozoic	Extensive drowning of the floodplain, resulting in the formation of widespread lacustrine deposition	Sandstone and mudstone	Tirsgaard and Ø xnevad, 1998
Ireland	County Antrim, Northern Ireland	the Mercia Mudstone Group	Triassic	Acid salt lake	Red mudstone	Andeskie et al., 2018
Mexico	South of Galeana	the Huizachal Formation	Triassic-Jurassic	Grabens in the Gulf of Mexico rift system	Siltstone	Michalzik, 1991
Pakistan	the Hazara–Kashmir Syntaxis of Northern Pakistan	the Murree formation	Late Paleocene(55 m.y.) to early-middle Eocene age (45 m.y.)	Tidal channels in a continuously subsiding foreland basin	Sandstones and shales	Bossart and Ottiger, 1988, 1990
		the Sabathu formation (the Balakot Formation)	55–50Myr (latest Palaeocene to Mid Eocene	The oldest continental sedimentary succession in the foreland basin	Shale	Wells and Gingerich, 1987; Najman et al., 2001
Switherland	the Lower Glarus Nappe complex of the Helvetic zone	the Verrucano and Quartenschiefer formations	Permian-Triassic	-	Deformed shale	Hirt et al., 1986
U.K.	Wales	-	Cambrian	Welsh Lower Paleozoic Basin	Slate	Wood et al., 1976
	County Antrim, Northern Ireland	the Mercia Mudstone Group	Triassic	Shallow perennial saline lakes and associated environments	Mudstone	Andeskie, 2016
U.S.A	South eastern New Mexico	the Pierce Canyon formation	Permian	the Delaware basin	Sandstone	Miller, 1966
	the Wyoming Salient	the Ankareh Formation	Triassic	Sedimentary basin	Red, quartzose to subarkosic, variably micaceous to calcareous sandstone and mudstone	Weil et al., 2010
	the Colorado Plateau, Arizona	the Chinle Formation	Late Triassic	Continental	Mudstone and siltstone	Olsen et al., 2018
	Northern New Mexico	the Rock Point Formation of the Chinle Group	Late Triassic (Rhaetian)	Continental interior	Mudstone	Cleveland et al., 2008
	Ionia, Michigan	the Pewamo Formation	Holocene and Pleistocene	Eolian desert	Eolian quartz sandstone	Benison et al., 2011

Table 2

Table 2 List of locations of heavy metals concretion occurrence. All of the concretions are found in bleached spot.

Country	Area	Stratigraphy	Age	Setting	Rock type	Enriched elements	Reference
Australia	near Kalbarri, Western Australia	the Tumblagooda Sandstone	Ordovician–lower Silurian	Basin	Sandstone	Fe, Ti, U	Fox et al., 2020
Canada	McArthur Basin, Northern Australia	the Tawallah Group	Late Palaeoproterozoic	-	-	-	Parnell, 2018
	Dorchester Cape, New Brunswick	the Hopewell Group	Late Carboniferous	Gleyed horizons and calcretes, and partially a playa lake	Conglomerates, sandstones, mudstones	Cu, Ag, Fe, Ti, U, V and REE	Lines et al., 1996
	Ontario	the Sibley Group	Mesoproterozoic	-	-	-	Parnell, 2018
China	Jiaolai Basin	-	Cretaceous	-	Sandstone	V, Fe, Pb	Yang et al., 2019
Czech	Bohemian Massif	the Líně formation, the Vrchlabí formation etc.	Upper Paleozoic	Continental basin	Mudstone	V, U	Pesek and Skocek, 1999
Germany	Weitenau, southern Germany	Rotliegendes	Permian	-	-	U	Hofmann, 1991a
	Helgoland	the Bunter Sandstone formation	Triassic	-	Sandstone	-	Hofmann, 1991a
Oman	Al Hammnah Range	the Warah formation	Jurassic-Cretaceous	-	-	-	Hofmann, 1991a
Switzerland	Northern Switzerland	Oberrotliegendes	Permian	Tectonic graben, fluvial	Mudstone, Sandstone	V, U, Ni, Co, As, Cu, Se, Pb, S	Hofmann, 1989, 1990, 1991b, 1993
U.K.	Midland Valley in Scotland	the Kelly Burn Sandstone Formation	Devonian	Fluviatile facies in continent	Sandstone	U, Se, Mo, Cu, V	Spinks et al., 2014
	Dingwell, Scotland	Old Red Sandstone	Devonian	-	Sandstone	U, REE	Parnell, 1985; Parnell and Eakin, 1987; Hofmann, 1993
	Sidmouth, Devon	the Littleham Mudstone Formation	Late Permian or Early Triassic	River channel, flood basin, or ephemeral lake environments	Mudstone	U, V, Ni, Co, Cr, Cu, As, Ag	Perutz, 1939; Durrance et al., 1978, 1980; Kemp et al 1994, 1996; Milodowski et al., 2000, 2002; Harrison, 2010; Yoshida et al., 2015; Parnell, 2016
	Warwick	the Enville Group	Late Carboniferous-Early Permian	-	Coarser grained marl and sandstone	Cu, V, U	Mykura and Hampton, 1984
	NW Scotland	the Bay of Stoer Formation, the Stoer Group	Pernian-Triassic	Fluvial and lacustrine	Sandstone, siltstone and shale	V	Spinks et al., 2010; Pernell et al., 2016, 2018
	Northern Ireland	the Mercia Mudstone Group	Triassic	-	Mudstone	V	Parnell, 1988; Spinks et al., 2010
	East Midland, near Nottingham	the Mercia Mudstone Group	Triassic	-	Mudstone	V, Te, Se	Parnell et al., 2016
	Knowle, West Midlands	the Mercia Mudstone Group	Triassic	-	Mudstone	U, V, Ni, Co, Cu	Hofmann, 1993
	Gipsy Lane Brickpit, Leicester	the Mercia Mudstone Group	Triassic	-	Mudstone	U, Cu, Ni, Co	Hofmann, 1993

Table 2 (continued)

	Grand Canyon, Arizona	the Hakatai formation	Precambrian	-	-	-	Hofmann, 1991a
	Shartlesville, Pennsylvania	the Hamburge formation	Ordovician	-	-	-	Hofmann, 1991a
	Climax, Colorado	the Minturn formation	Carboniferous	-	-	-	Hofmann, 1991a
	Lyons, Colorado	the Fountain formation	Permo-Carboniferous	-	-	-	Hofmann, 1991a
U.S.A.	Kiowa Country, Oklahoma	the Hennessey Group	Permian	Nearshore deposit	Siltstone	U, Ni, Co, As, Pb, Se	Curiale et al., 1983; Hofmann, 1991a, 1993
	Oklahoma Co., Oklahoma	the Garber Sst. Formation	Permian	-	Siltstone	-	Hofmann, 1991a
	Southern Kansas	the Nippewalla Group	Mid-Permian (Leonardian)	Continental basin (lake and saline pan)	Siltstone	-	Benison and Goldstein, 2001
	Bedrock, Paradox Valley, Colorado	the Chinle formation	Triassic	-	-	-	Hofmann, 1991a
	Montana	the Spokane Formation in the Belt Supergroup	Mesoproterozoic	-	-	-	Parnell, 2018

Table 3 Representative bulk compositions of zebra rock. Total Fe as Fe_2O_3, LOI*: (initial LOI (: loss on ignition)) − (S (%)), r: reddish band, w: white background, o: outer part of zebra pattern. Sampling points refer to Fig. 8a, b.

	Sample No.	SiO_2	TiO_2	Al_2O_3	Fe_2O_3	MnO	MgO	CaO	Na_2O	K_2O	P_2O_3	S	LOI*	Total
Kao-type zebra rock	ZRY-06w1	63.7	0.99	24.1	0.36	0	0.21	0.06	0.10	1.78	0.10	0.07	8.97	100.4
	ZRY-06r1	59.1	0.96	21.1	9.31	0	0.20	0.06	0.12	1.76	0.10	0.07	7.91	100.7
	ZRY-06w2	64.2	1.02	24.4	0.37	0	0.21	0.07	0.11	1.81	0.10	0.06	8.84	101.2
	ZRY-06r2	59.5	0.97	21.3	9.46	0	0.21	0.06	0.10	1.77	0.10	0.08	7.66	101.2
	ZRY-06o	64.3	0.91	24.6	0.34	0	0.20	0.06	0.11	1.76	0.11	0.07	8.19	100.6
Alu-type zebra rock	ZRY-07w1	55.3	0.62	16.7	0.25	0	0.01	0.05	0.93	3.55	0.08	6.49	17.1	101.1
	ZRY-07r1	41.8	0.61	10.9	30.1	0	0.02	0.06	0.57	2.09	0.06	3.94	11.0	101.2
	ZRY-07w2	54.8	0.63	16.9	0.30	0	0.01	0.06	0.94	3.58	0.08	6.68	16.8	100.8
	ZRY-07r1	42.3	0.61	10.8	30.5	0	0.02	0.06	0.56	2.06	0.06	4.14	10.8	101.8
	ZRY-07o	42.8	0.64	22.3	1.66	0	0.01	0.06	1.14	4.14	0.10	7.48	20.6	101.0

Table 4 Concentration factor of Fe concentration parts of zebra rock, Fe oxide concretions, and Fe oxide band in dacite cobble.

	Sample No.	Fe_2O_3 (wt%) of background	Fe_2O_3 (wt%) of Fe concentration part	Concentration factor
Zebra rock	ZRY-06-band1	0.36	9.31	25.9
	ZRY-06-band2	0.37	9.46	25.6
	ZRY-07-band1	0.25	30.1	120.4
	ZRY-07-band2	0.30	30.5	101.7
Fe oxide concretion	Mo-Go030	0.79	28.3	35.8
	Mo-Go-032	0.63	31.9	50.6
	Jo-005	0.25	7.03	28.1
Fe oxide bands in dacite cobble	NGY-01	1.08	3.65	3.38

Table 5 Results of mass balance calculation (τ) for major elements in zebra rock. Tau (τ) of ZRY-06-1 is calculated by comparing ZRY-06w1 and ZRY-06r1 in Table 3, and so forth.

	T (Si)	τ (Al)	τ (Fe)	τ (Mg)	τ (Ca)	τ (Na)	τ (K)	τ (P)	τ (S)
ZRY-06-1	0.0	−0.1	26.0	0.0	0.0	0.1	0.0	0.0	0.0
ZRY-06-2	0.0	−0.1	25.8	0.1	−0.1	0.0	0.0	0.0	0.4
ZRY-07-1	−0.2	−0.3	121.4	1.2	0.1	−0.4	−0.4	−0.2	−0.4
ZRY-07-2	−0.2	−0.4	103.4	1.2	0.3	−0.4	−0.4	−0.2	−0.4

Table 6. Characteristics of three types of pseudomorph.

	Mineral assemblage	Occurrence			Bleached spot
		Outside band	Margin of band	Inside band	
Type-1	Hem + Goe	+			
Type-2	Hem + Goe + Dck	+	+		+
Type-3	Dck	+	+	(+)	+

Dck, dickite; Goe, goethite; Hem, hematite. "+" represents present.

Table 7 Representative microprobe analysis of type 1 and 3 pseudomorphs in ZRY-07a.

	Type1-1	Type3-1	Type3-5	Type3-7	Type3-8
Mineral	Hematite + Goethite	Dickite			
SiO_2 wt%	2.22	44.0	45.9	46.3	46.0
Al_2O_3	0.48	37.8	38.7	39.8	39.7
TiO_2	0.05	1.22	0.02	0.04	0.00
FeO	71.8	0.22	0.33	0.06	0.09
MnO	0.00	0.00	0.00	0.00	0.00
K_2O	0.05	0.05	0.06	0.14	0.13
SO_3	0.17	0.05	0.04	0.10	0.04
Fe_2O_3 (c)	79.8	0.24	0.37	0.06	0.10
Total	82.7	83.4	85.0	86.4	85.9
O a.p.f.u	3	7	7	7	7
Si	0.07	1.96	2.00	1.98	1.98
Al	0.02	1.99	1.98	2.01	2.02
Ti	0.00	0.04	0.00	0.00	0.00
Fe^{3+}	1.88	0.00	0.01	0.00	0.00
Mn	0.00	0.00	0.00	0.00	0.00
K	0.00	0.00	0.00	0.01	0.01
S	0.00	0.00	0.00	0.00	0.00
Sum cation	1.97	3.99	3.99	4.00	4.01

(c): calculated value

Table 8 Representative bulk compositions of Fe oxide concretions in Mongolia and Jordan, and Fe oxide bands in a dacite cobble in Nagara river, Gifu Prefecture.

	Sample No.	Drilling point	SiO_2	TiO_2	Al_2O_3	Fe_2O_3	MnO	MgO	CaO	Na_2O	K_2O	P_2O_3	LOI	Total
Fe oxide concretions	Mo-Go030	Crust	53.5	0.15	6.53	28.3	0.36	0.57	0.73	1.48	2.10	0.09	6.34	100.1
	Mo-Go030	Core	80.0	0.21	10.4	0.79	0.01	0.44	0.83	2.32	3.25	0.03	2.17	100.4
	Mo-Go032	Crust	51.8	0.13	5.86	31.9	0.28	0.49	0.58	1.28	2.09	0.08	6.36	100.8
	Mo-Go032	Core	82.1	0.22	9.77	0.63	0.01	0.42	0.61	2.17	3.29	0.03	1.89	101.1
	Jo-005	Crust	80.5	0.38	7.29	7.03	0.03	0.22	0.42	0.05	0.08	0.29	4.22	100.5
	Jo-005	Matrix	87.8	0.38	8.39	0.25	0.00	0.05	0.39	0.04	0.07	0.17	3.35	100.9
Fe oxide bands in dacite cobble	NGY-01	Band	71.5	0.11	13.6	3.65	0.08	0.15	0.13	2.94	3.79	0.04	2.42	99.1
	NGY-01	White background	72.9	0.09	15.3	1.08	0.03	0.16	0.14	3.45	3.93	0.03	2.24	99.3
	NGY-01	Core	71.5	0.18	14.4	1.77	0.06	0.17	1.30	3.05	3.90	0.05	3.36	99.7

Total Fe as Fe_2O_3, LOI, loss on ignition.